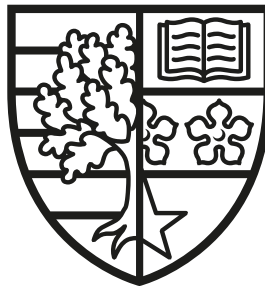


# Millimetre-wave Radar Development for High Resolution Detection

Cristian A. Alistarh

SUBMITTED FOR THE DEGREE OF  
DOCTOR OF PHILOSOPHY

HERIOT-WATT UNIVERSITY



SCHOOL OF ENGINEERING & PHYSICAL SCIENCES,  
INSTITUTE FOR SIGNALS, SENSORS AND SYSTEMS.

November, 2022

The copyright in this thesis is owned by the author. Any quotation from the thesis or use of any of the information contained in it must acknowledge this thesis as the source of the quotation or information.

## Abstract

Automotive technology today is focusing on autonomous vehicle development. The sensors for these systems include radars due to their robustness against adverse weather conditions such as rain, fog, ash or snow. In this constant search for advancement, high resolution systems play a central role in target detection and avoidance. In this PhD project, these methods have been researched and engineered to leverage the best radar resolution for collision avoidance systems.

The first part of this thesis will focus on the existing systems consisting of the state-of-the-art at the time of writing and explain what makes a high resolution radar and how it can cover the whole field of view. The second part will focus on how a non-uniform sparse radar system was simulated, developed and benchmarked for improved radar performance up to 40% better than conventional designs. The third part will focus on signal processing techniques and how these methods have achieved high resolution and detection: large virtual aperture array using Multiple Input Multiple Output (MIMO) systems, beam pattern multiplication to improve side-lobe levels and compressive sensing. Also, the substrate-integrated waveguide (SIW) antennas which have been fabricated provide a bandwidth of 1.5GHz for the transmitter and 2GHz at the receiver. This has resulted in a range resolution of 10 cm. The fourth part of this thesis presents the measurements which have been carried out at the facilities within Heriot-Watt University and also at Netherlands Organisation for Applied Scientific Research (TNO). The results were better than expected since a two transmitter four receiver system was able to detect targets which have been separated at  $2.2^\circ$  in angle in the horizontal plane. Also, compressive sensing was used as a high resolution method for obtaining fine target detection and in combination with the multiplication method showed improved detection performance with a 20 dB side-lobe level suppression. The measurement results from the 6-months placements are presented and compared with the state-of the art, revealing that the developed radar is comparable in performance to high-grade automotive radars developed in the industry.

# Dedication

*To my beloved family and friends who have supported me so much.*

*You all deserve to see what I have been up to all these years.*

## Acknowledgements

I would like to offer my heartfelt thanks to my supervisors: Prof. Symon K. Podilchak, Prof. John Thompson, Prof. Mathini Selluthurai since they have been a pillar of support throughout these years as a PhD student. I would also like to thank the members of staff at Heriot Watt: Prof. George Goussetis and Prof. Dimitris Anagnostou.

Especially, I would like to thank Prof. Podilchak since he has never failed to give me exceptional advice and support. It would be an understatement to say that my success throughout these years has resulted because of the great supervision of Symon. It is his professionalism and perseverance as well as dedication which made me love my topic associated with antennas and radar. I would like also to sincerely thank Prof. Thompson since it is with his good will that my degree has been co-supervised with the University of Edinburgh. His experience with signal processing and also review of my work has made me eager to pursue different methods and also learn about the best techniques in signal processing. I am really privileged to be one of his students in both undergraduate and postgraduate degrees. A word of sincere thanks goes to my supervisor, Prof. Mathini Selluthurai, who has always given me good ideas to explore in my work. My transition to her as a student has been very fortunate and I will always be thankful for her support.

Special thanks go to the staff at Netherlands Organisation for Applied Scientific Research (TNO), Defence and Security who have hosted me for 6 months during my internship: Laura Anitori, Wim van Rossum and Dave Bakers, Frank van De-Bogaart, Caspar Lageweg and Pepjin Cox.

I would also like to thank the staff at Leonardo for their support and encouragements for the work developed during the PhD.

I would also like to thank my dear colleagues who have been so great over the years: Pascual, Rahil, Victoria, Salvador, Maria Jesus, Callum, Kostas, Panagiota, Adrian, Carlos, Alexis, Sam, Spyros, Sadeque, Khalid, Jose, Dave and many more.

I hope that this PhD thesis will be a statement of thanks to everyone who has supported me throughout these years.



# Internal Examiners Declaration Form

(This form must be typed and all sections completed)

Candidate's Name:	Cristian Alistarh	Heriot-Watt Person ID:	H00282715
School:	EPS	Degree Sought:	PhD
Campus: (If off-campus please state location)	Edinburgh		

## Declaration

- I confirm that the corrections to the thesis of the above named have been carried out to the satisfaction of the examiners Yes ☒ No ☐ N/A ☐
- I confirm that the Joint Examiners Report Form states recommendation (b) - 'Award degree following satisfactory completion of minor corrections' Yes ☒ No ☐

### If yes,

- Please provide details below to demonstrate that the particular corrections are satisfactory.
- Confirm that the corrections have been completed within the period of time given, if not please give an explanation.

The two examiners agreed with the candidate to perform the corrections for a time period of five months and insist that the award of the PhD is given with minor corrections. The reason for this is that the candidate was on a full time job as a researcher in the uni. The work is of high quality and the corrections could have been easily made in the usual three months time limit,. But the fact that the candidate was employed on a full-time basis and to give justice to the candidate efforts, the examiners have allowed five months for the minor corrections to be completed.

- I confirm that the Joint Examiners Recommendation was originally: Re-submit (decision (c or d) on the previous Joint Examiners Form) Yes ☐ No ☒
- I confirm that thesis title has changed since the temporary thesis was submitted. If yes, please provide details of amended title here: Yes ☐ No ☒

- I confirm that I have seen the presentation (final bound) thesis and it has been bound in accordance with University regulations. Yes ☐

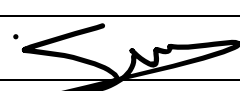
## Electronic Thesis

As the Internal Examiner, I confirm that the student has prepared an electronic copy of the thesis in accordance with University guidelines **and it is an exact copy of the final bound thesis.**

Yes ☒ No ☐

In accordance with [Heriot-Watt University Regulations](https://www.hw.ac.uk/students/studies/examinations/thesis.htm), all students submitting research theses to the University for the awards of Doctor of Philosophy, Doctor of Philosophy by Published Research, Doctor of Engineering, Doctor of Business Administration, Master of Philosophy and/or Higher Degrees of Master (Research), must provide an electronic version of their final thesis. Further information on electronic thesis submission is available in the Submission and Format of Thesis Guidelines, available at <https://www.hw.ac.uk/students/studies/examinations/thesis.htm>

## Internal Examiner

Print Name:	Souheil Ben Smida	Date:	14/11/2022
Signature:		School:	EPS

## Notes

1. Please note that under current University Regulations one presentation (final bound) and one electronic copy of the thesis are required for final submission.
2. The Internal Examiner's Declaration Form should be submitted along with the presentation (final bound) and electronic copy of the thesis to the Student Service Centre.

## Research Thesis Submission

Please note this form should be bound into the submitted thesis.

Name:	Cristian-Alexandru Alistarh		
School:	Engineering and Physical Science (EPS)		
Version: <i>(i.e. First, Resubmission, Final)</i>	Final	Degree Sought:	PhD. (Electrical Engineering)

### Declaration

In accordance with the appropriate regulations I hereby submit my thesis and I declare that:


1. The thesis embodies the results of my own work and has been composed by myself
2. Where appropriate, I have made acknowledgement of the work of others
3. The thesis is the correct version for submission and is the same version as any electronic versions submitted\*.
4. My thesis for the award referred to, deposited in the Heriot-Watt University Library, should be made available for loan or photocopying and be available via the Institutional Repository, subject to such conditions as the Librarian may require
5. I understand that as a student of the University I am required to abide by the Regulations of the University and to conform to its discipline.
6. I confirm that the thesis has been verified against plagiarism via an approved plagiarism detection application e.g. Turnitin.

### ONLY for submissions including published works

Please note you are only required to complete the Inclusion of Published Works Form (page 2) if your thesis contains published works)

7. Where the thesis contains published outputs under Regulation 6 (9.1.2) or Regulation 43 (9) these are accompanied by a critical review which accurately describes my contribution to the research and, for multi-author outputs, a signed declaration indicating the contribution of each author (complete)
8. Inclusion of published outputs under Regulation 6 (9.1.2) or Regulation 43 (9) shall not constitute plagiarism.

\* Please note that it is the responsibility of the candidate to ensure that the correct version of the thesis is submitted.

Signature of Candidate:		Date:	14/11/2022
-------------------------	---	-------	------------

### Submission

Submitted By <i>(name in capitals)</i> :	
Signature of Individual Submitting:	
Date Submitted:	

### For Completion in the Student Service Centre (SSC)

Limited Access	Requested	Yes		No		Approved	Yes		No	
E-thesis Submitted <i>(mandatory for final theses)</i>										
Received in the SSC by <i>(name in capitals)</i> :						Date:				

## Inclusion of Published Works

Please note you are only required to complete the Inclusion of Published Works Form if your thesis contains published works under Regulation 6 (9.1.2)

### Declaration

This thesis contains one or more multi-author published works. In accordance with Regulation 6 (9.1.2) I hereby declare that the contributions of each author to these publications is as follows:

Citation details	C. A. Alistarh, S K. Podilchak, P. D. Hilario Re, T. M. Strober, Y. Pailhas, C. Mateo-Segura, M. Sellathurai, G. Goussetis, Y. Petillot, J. S. Thompson, J. Lee, " <b>Sectorized FMCW MIMO Radar by Modular Design with Non-uniform Sparse Arrays</b> ", IEEE Journal of Microwaves, 2022 (accepted with major revisions)
C. A. Alistarh	Theoretical analysis, radar and antenna simulations and measurements, antenna fabrication, post-processing and writing of the paper, corrections.
S K. Podilchak	Supervision, guidance, corrections.
P. D. Hilario Re	Measurements, antenna modelling and simulation
T. M. Strober	Antenna modelling and simulation
Y. Pailhas	Guidance, corrections
C. Mateo-Segura	Guidance
M. Sellathurai	Guidance, supervision, corrections
G. Goussetis	Guidance
Y. Petillot	Guidance
J.S. Thompson	Guidance, supervision, corrections
J. Lee	Supervision
Signature:	
Date:	14/11/2022

Citation details	C. A. Alistarh, D. Bekers, S. K. Podilchak, L. Anitori, W. van Rossum, R. Boekema, M. Sellathurai, J. S. Thompson, " <b>Compressed Radar Sensing Using Non-Uniformly Spaced SIW Antenna Receiver</b> ", IEEE Transaction in Antennas and Propagation, 2022, (submitted, under review)
C. A. Alistarh	Theoretical analysis, radar and antenna simulations and measurements, antenna fabrication, post-processing and writing of the paper (80%), corrections.
D. Bekers	Simulations, supervision, guidance, writing of paper (20%)
S. K. Podilchak	Supervision, guidance, corrections
L. Anitori	Supervision, guidance, corrections
W. van Rossum	Simulations, supervision, corrections
R. Boekema	Measurement set-up and preparation
M. Sellathurai	Guidance, corrections
J.S. Thompson	Guidance, corrections
Signature:	
Date:	14/11/2022

Citation details	F. Alsaleem, J.S. Thompson, D. I. Laurenson, S. K. Podilchak, C. A. Alistarh <b>“Small-Size Blockage Propagation Modeling at 28 GHz for mmWave Communications Systems”</b> , IEEE Transactions on Antennas and Propagation (accepted with revisions), 2022
F. Alsaleem	Theoretical analysis, simulations and measurements, antenna fabrication, post-processing and writing of the paper, corrections.
J. S. Thompson	Supervision, guidance, corrections
D. I. Laurenson	Supervision, corrections
S. K. Podilchak	Supervision, guidance, corrections
C. A. Alistarh	Measurements
Signature:	
Date:	14/11/2022

Citation details	M. K. Kuznetcov, S.K. Podilchak, M. I. Poveda-Garcia, P. D. Hilario Re, C. A. Alistarh, G. Goussetis, J. L. Gomez-Tornero, <b>“Compact Leaky-Wave SIW Antenna With Broadside Radiation and Dual-Band Operation for CubeSats”</b> , IEEE Transactions on Antennas and Propagation, Vol. 20 (Issue. 11), pp. 2125 - 2129, 2021, ISSN: 1548-5757.
M. K. Kuznetcov	Theoretical analysis, simulations and measurements, antenna fabrication, post-processing and writing of the paper, corrections.
S. K. Podilchak	Supervision, guidance, corrections
P. D. Hilario Re	Measurements, Corrections
M. I. Poveda-Garcia	Measurements, Simulations, Antenna Modelling
C. A. Alistarh	Measurements
J. L. Gomez-Tornero	Supervision, Guidance, Corrections
Signature:	
Date:	14/11/2022

Citation details	P.D. Hilario Re, D. Comite, S. K. Podilchak, C. A. Alistarh, G. Goussetis, M. Sellathurai, J. S. Thompson, J. Lee, <b>“FMCW Radar With Enhanced Resolution and Processing Time by Beam Switching”</b> IEEE Open Journal on Antennas and Propagation, Vol. 2 (No. 21076384 ), pp. 882 - 896, 2021, ISSN: 2637-6431 .
P. D. Hilario Re	Theoretical analysis, simulations and measurements, antenna fabrication, post-processing and writing of the paper, corrections.
D. Comite	Paper writing, corrections
S. K. Podilchak	Supervision, Guidance, Corrections
C. A. Alistarh	Measurements, Simulations of Radar System
M. Sellathurai	Corrections
J.S. Thompson	Corrections
J. Lee	Supervision
Signature:	
Date:	14/11/2022

# List of Publications

## Journal Publications

1. **Alistarh, Cristian A**; Podilchak, Symon K; Anitori, Laura; van Rossum, Wim; Bekers, Dave; Boekema, Rob; Sellathurai, Mathini; Thompson, John S, “**Compressed Radar Sensing Using Non-Uniformly Spaced SIW Antenna Receiver**”, IEEE Transactions in Antennas and Propagation, **in preparation**, 2022.
2. **Alistarh, Cristian A**; Podilchak, Symon K; Re, Pascual Hilario D; Thomas M; Sellathurai, Mathini; Pailhas, Yan; Petillot, Yvan; Mateo-Segura, Carolina; Goussetis, George; Thompson, John S; Lee, Jaesup, “**Sub-modular FMCW MIMO Radar Design by Non-uniform Sparse Arrays**”, IEEE Journal of Microwaves, **submitted (under review)**, 2022.
3. Re, Pascual Hilario D; Comite, David; Podilchak, Symon K; **Alistarh, Cristian A**; Goussetis, George; Sellathurai, Mathini; Thompson, John S; Lee, Jaesup, “**FMCW Radar With Enhanced Resolution and Processing Time by Beam Switching**”, IEEE Open Journal on Antennas and Propagation, Vol. 2 (No.21076384 ), pp. 882 - 896, 2021, ISSN: 2637-6431
4. Kuznetcov, Maksim V; Podilchak, Symon K; Poveda-Garcia, Miguel; Re, Pascual Hilario D; **Alistarh, Cristian A**; Goussetis, George; Gomez-Tornero, Jose Luis, “**Compact Leaky-Wave SIW Antenna With Broadside Radiation and Dual-Band Operation for CubeSats**”, IEEE Transactions on Antennas and Propagation, Vol. 20 (Issue. 11), pp. 2125- 2129, 2021, ISSN: 1548-5757.
5. Alsaleem, Fahd; Thompson, John S; Laurenson, David I; Podilchak, Symon K; **Alistarh, Cristian A**, “**Small-Size Blockage Propagation Modeling**

at 28 GHz for mmWave Communications Systems” IEEE Transactions on Antennas and Propagation, **accepted with revisions**, 2022

## Conference Papers

1. **Alistarh, Cristian A**; Anitori, Laura; van Rossum, Wim; Podilchak, Symon K; Thompson, John S; Sellathurai, Mathini, “**Compressed Sensing for MIMO Radar using SIW Antennas for High Resolution Detection**”, 18th European Radar Conference (EuRAD) 2021 (London), **accepted**, April 2022.
2. Alsaleem, Fahd; Thompson, John S; Laurenson, David I; Podilchak, Symon K; **Alistarh, Cristian A**, “**Small-Size Blockage Measurements and Modeling for mmWave Communications Systems**”, 2020 International Symposium on Personal, Indoor and Mobile Radio Communications, 2020.
3. **Alistarh, Cristian**; Anitori, Laura; Podilchak, Symon K; Thompson, John; Re, Pascual Hilario D; Sellathurai, Mathini; Goussetis, George; Lee, Jaesup, “**Millimeter-wave Automotive Radar using Extrapolation for Improved Angular Resolution**”, 17th European Radar Conference (EuRAD), IEEE 2020.
4. Shafiq, Zain; **Alistarh, Cristian A**; Anagnostou, Dimitris E; Podilchak, Symon K, “**Towards MIMO-Monopulse FMCW Radar for Automotive Applications using SIW Antennas**”, IEEE Asia-Pacific Conference on Antennas and Propagation (APCAP’2020 on-line), 2020.
5. Re, Pascual Hilario; **Alistarh, Cristian**; Podilchak, Symon; Goussetis, George; Thompson, John; Lee, Jaesup, “**Millimeter-wave FMCW Radar Development using SIW Butler Matrix for Time Domain Beam Steering**”, 2019 16th European Radar Conference (EuRAD), IEEE 2019.
6. **Alistarh, Cristian A**; Podilchak, Symon K; Goussetis, George; Thompson, John S; Lee, Jaesup, “**Spectral Smoothing by Multiple Radar Pattern Multiplication for Improved Accuracy**”, University of Waterloo, International Symposium on Antenna Technology and Applied Electromagnetics (ANTHEM) , Waterloo, Canada, 2018.

7. **Alistarh, Cristian**; Hilario Re, Pascual ; Thomas M, ; Rotenberg, Samuel; Podilchak, Symon; Mateo-Segura, Carolina; Pailhas, Yan; Goussetis, George; Petillot, Yvan; Thompson, John S; Lee, Jaesup, “**Millimetre-Wave FMCW MIMO Radar System Development Using Broadband SIW Antennas**”, 2018 12th European Conference on Antennas and Propagation (EU-CAP), 2018.

## Publications in Preparation

1. **Alistarh, Cristian A**; Podilchak, Symon K; Thompson, John S; Selluthurai, Mathini, “***Highly Separated Automotive Radar Antennas for Improved Detection Accuracy***”, IEEE Microwave Theory and Techniques, 2022.
2. **Alistarh, Cristian A**; Podilchak, Symon K; Thompson, John S; Selluthurai, Mathini, “***Monopulse Radar Antennas for Collision Avoidance Applications***”, IEEE Transactions on Antennas and Propagation, 2022.



# Contents

<b>Glossary</b>	<b>xvi</b>
<b>List of Symbols</b>	<b>xviii</b>
<b>1 Introduction</b>	<b>1</b>
1.1 Motivation and goal . . . . .	1
1.2 Background . . . . .	1
1.3 Motivation and Main Contributions . . . . .	4
1.4 Thesis Outline . . . . .	5
<b>2 Background</b>	<b>7</b>
2.1 Motivation and goal . . . . .	7
2.1.1 Chapter outline . . . . .	7
2.2 Radar in History . . . . .	8
2.3 Radar Basics . . . . .	8
2.4 Radar Types . . . . .	10
2.4.1 Measuring distance . . . . .	11
2.4.2 Doppler shift . . . . .	13
2.4.3 Defining the FMCW radar signals . . . . .	15
2.5 Automotive Radar Concept . . . . .	16
2.6 Key Parameters in Automotive Radar Performance . . . . .	16
2.7 SIMO and MIMO radar . . . . .	23
2.7.1 Definition . . . . .	23
2.7.2 MIMO Radar Configurations . . . . .	25
2.7.3 MIMO Radar Angular Resolution Improvement . . . . .	26
2.8 State-of-the-art Automotive Radars . . . . .	27

2.9	Propagation model: Two-way propagation channel model . . . . .	32
2.10	Radar Link Budget . . . . .	34
2.11	Substrate Integrated Waveguide Technology . . . . .	36
2.12	Microstrip patch antennas versus SIW antennas . . . . .	38
2.13	State-of-the art limitations and Outlook . . . . .	38
2.14	Contributions by the candidate . . . . .	40
<b>3</b>	<b>FMCW SIW Radar Systems</b>	<b>41</b>
3.1	Introduction . . . . .	41
3.1.1	Motivation and goal . . . . .	41
3.2	Overview of Radar Concepts . . . . .	42
3.3	Sectorized Radar System Design . . . . .	43
3.4	Radar Antenna Design . . . . .	50
3.4.1	Transmit Substrate Integrated Waveguide (SIW) Antennas . .	52
3.4.2	Receive Substrate Integrated Waveguide (SIW) Antenna Ar- rays and Dual-Mode Detection . . . . .	53
3.4.3	Two-tier process for non-uniform antenna design . . . . .	54
3.4.4	Selecting the best antenna configuration . . . . .	54
3.4.5	Radar system specifications . . . . .	57
3.5	Sectorized Radar System Measurements . . . . .	63
3.5.1	Radar Measurement Setup . . . . .	63
3.5.2	Radar Linearity and Range Resolution Measurements . . . . .	63
3.6	Angular Resolution Measurements . . . . .	67
3.6.1	Power budget for complicated radar scenarios . . . . .	71
3.7	Discussion . . . . .	72
3.8	Summary and Conclusions . . . . .	73
3.9	Contributions by the candidate . . . . .	73
<b>4</b>	<b>Signal processing techniques with improved target detection for MIMO Automotive Radar</b>	<b>75</b>
4.1	Motivation and goal . . . . .	76
4.2	Spectral smoothing using beampattern multiplication . . . . .	76
4.2.1	Background . . . . .	76

4.2.2	Smoothing Using a sinc Function . . . . .	79
4.2.3	Multiplication Smoothing Function Practical Implementation .	80
4.2.4	Measurement Results . . . . .	82
4.2.5	Additional simulations for the Multiplication method . . . . .	83
4.3	Interpolation and Extrapolation of Antenna Array Data for Enhanced Radar Detection . . . . .	84
4.3.1	Background . . . . .	84
4.3.2	Practical Implementation of Interpolation and Extrapolation for Radar System . . . . .	88
4.3.3	Measurements with extrapolation . . . . .	88
4.3.4	Measurements with the Interpolation Method . . . . .	91
4.4	Highly Separated Radar Systems for Improved Target Illumination . .	92
4.4.1	Background . . . . .	92
4.4.2	Highly Separated Radar . . . . .	95
4.5	Conclusions and future work . . . . .	98
4.6	Contributions by the candidate . . . . .	98
<b>5</b>	<b>Compressed Sensing for High Resolution Radar Detection</b>	<b>100</b>
5.1	Introduction . . . . .	100
5.1.1	Motivation and goal . . . . .	101
5.2	Compressive Sensing (CS) . . . . .	101
5.2.1	CS in Automotive Radar . . . . .	102
5.2.2	Problem formulation . . . . .	105
5.2.3	Application of CS to Radar . . . . .	107
5.3	Your Algorithm for L1 (YALL1) . . . . .	107
5.4	Non-uniform sparse array . . . . .	110
5.5	Design of the non-uniform sparse array . . . . .	110
5.5.1	Non-uniform antenna array scanning with angle . . . . .	112
5.5.2	Non-uniform Antenna Array Fabrication . . . . .	113
5.6	Measurement Setup and Results . . . . .	114
5.6.1	Antenna Beampatterns . . . . .	114
5.6.2	Radar Measurements over frequency . . . . .	116
5.6.3	Radar Measurements with CS . . . . .	116

5.6.4	CS and Multiplication . . . . .	119
5.6.5	Measurements with radar rotation . . . . .	119
5.6.6	Discussion and limitations . . . . .	121
5.7	Conclusions and future work . . . . .	122
5.8	Contributions by the candidate . . . . .	122
<b>6</b>	<b>Conclusions</b>	<b>124</b>
6.1	Motivation and goal . . . . .	124
6.2	Novelty in this work . . . . .	125
6.3	Limitations of this work . . . . .	126
6.4	Future work endeavours . . . . .	127
<b>A</b>	<b>Compressive sensing beamforming implementation with YALL1</b>	<b>128</b>
<b>B</b>	<b>Additional Simulations with the Multiplication Method</b>	<b>132</b>
<b>C</b>	<b>Measurement Setup for Anechoic Chamber Measurements</b>	<b>137</b>

# List of Tables

3.1	Comparison of Other Radar Systems as Reported in the Literature . . . . .	44
3.2	Circuit Components for the Radar . . . . .	60
3.3	Three Different Measured RM Transmitter Outputs <sup>1</sup> . . . . .	64
4.1	Radar Specifications for Multiplication Measurement Trial . . . . .	83
4.2	Additional simulations for Multiplication (Appendix B for full results)	84
4.3	Baseline ULA and Extended Receiver Comparison . . . . .	88
4.4	Summary of interpolated and extrapolated measurements for various antenna element sizes . . . . .	92
5.1	State-of-the-Art Radar System Comparison as Reported in the Lit- erature . . . . .	107
5.2	YALL1 Input Value Parameters . . . . .	109
5.3	Comparison of Optimal Sparse Antenna Receiver Array Configura- tions . . . . .	112

# List of Figures

1.1	High abstract layers are implemented more frequently in today's automotive radar [1.1]. . . . .	2
1.2	Automotive radar roadmap for next generation of autonomous vehicle systems. This figure is adopted from [1.2]. . . . .	3
2.1	British defence radar systems used in World War II [2.1]. . . . .	9
2.2	Illustration of linear frequency variation with time, for a linear FM modulation as found in [2.2]. . . . .	11
2.3	Illustration for a FMCW detection and determination of range as found in [2.2]. . . . .	12
2.4	Illustration of Doppler effect as found in [2.2]. . . . .	13
2.5	Solving for the Doppler effect using the up and down chirps of a triangular FMCW signal as found in [2.2]. . . . .	14
2.6	Types of automotive radar systems . . . . .	17
2.7	Radar Field-of-view (FOV) . . . . .	19
2.8	Angular resolution . . . . .	20
2.9	Wavefront arriving at the antenna receiver . . . . .	21
2.10	Digital beamformer . . . . .	23
2.11	Single-Input Multiple-Output and Multiple-Input Multiple-Output Architectures . . . . .	25
2.12	MIMO configurations . . . . .	26
2.13	Physical MIMO spacing vs MIMO virtual array spacing . . . . .	26
2.14	77-81 GHz radar with 2x16 MIMO antennas [2.23] . . . . .	28
2.15	77 GHz Quasi-optical radar [2.34] . . . . .	29
2.16	77 GHz radar with SIMO digital beamforming [2.45] . . . . .	29

2.17 MIMO 77 Ghz transceiver radar using non-uniform antenna element spacing with 4- [2.56]	30
2.18 Radar architecture	31
2.19 Comparison of off-the-shelf FMCW radar systems	32
2.20 Two-ray ground propagating model taking into account multipath as found in [2.64]. $E_{TOT}$ is the total field, $E_g$ is the ground reflected field, $E_i$ is the incident field, $\Theta_i$ is the incident angle, $\Theta_0$ is the reflected angle, $E_{LOS}$ is the line of sight field, $h_t$ is the transmitter height, $h_r$ is the receiver height, $d$ is the distance between transmitter and receiver, $E_0$ is the free-space electric field (in units of V/m).	33
2.21 Illustration of radar link budget diagram showing all system components and values for the power budget calculation.	35
2.22 Calculation of received power levels for a Single Input Single Output (SISO) radar system and a MIMO radar system assuming a signal to noise ratio (SNR) of 10 dB, noise figure of 10 dB, radar cross section of $1.5m^2$	35
2.23 SIW antenna cross section showing metalized vias (a) and the equivalent dielectric waveguide (b) (courtesy of [2.67])	37
2.24 Microstrip patch antenna beampattern measurements in the azimuth and elevation plane. (courtesy of [2.67])	39
2.25 SIW antenna beampattern measurements in the azimuth plane. (courtesy of [2.67])	39
3.1 Modular sectorized radar concept using three modular MIMO radars across the front bumper of an automobile.	45
3.2 Proposed automotive radar and antenna configuration: (a) SISO, (b) a MIMO radar module (RM) defined by 2 physical transmitters (TX) and four receivers (RX), (c) modular MIMO radar defined by 32 antenna elements in total ( $= 4 RM \times 2 TX \times 4 RX$ ), (d) sectorized MIMO radar system where 6 targets are illustrated.	45
3.3 Workflow diagram for the signal processing of the sectorized radar for one acquisition cycle, showing in-quadrature (IQ) data, delay and sum (DAS) beamforming and Fast Fourier Transforms (FFT).	46

3.4	Comparison of radar synchronisation designs based on FMCW radar architectures ranging from non-coherent networks (left) to synchronized systems (right) [1.1]	47
3.5	Single element SIW TX (left) and 8-element RX (right). The TX and RX SIW antenna ports, are labeled as $TP_i$ and $RP_i$ , respectively. The design has been carried out by Thomas Stoeber, another PhD student working in the automotive radar group.	51
3.6	Realised gain beam pattern of the SIW transmitter antenna in the horizontal plane.	52
3.7	Comparison of theoretical array factor, simulations and measurements for the $\lambda/2$ array with 4 RX elements using $RP_3$ , $RP_4$ , $RP_5$ , and $RP_6$ (see Figure 3.5).	53
3.8	Best antenna configuration for four element receiver array with $0.5\lambda$ -spacing between potential element positions.	55
3.9	Best antenna configuration for eight element receiver array with $0.5\lambda$ -spacing between potential element positions.	55
3.10	Two-tier process for determining the sparse, non-uniform antenna receiver from MIMO data for $\lambda/2$ and $\lambda$ -spacing.	56
3.11	Radar receiver configurations for 8-element $\lambda/2$ , $\lambda$ -spaced and non-uniform MIMO array receiver using SIW receiver antennas.	57
3.12	Array factor for beampattern array of RM with 8 elements at $\lambda/2$ uniform spacing, $\lambda$ uniform spacing, and sparse non-uniform spacing.	58
3.13	Array factor for beampattern array of RM with 32 elements at $\lambda/2$ uniform spacing, $\lambda$ uniform spacing, and sparse non-uniform spacing.	59
3.14	Comparison of measured 8 element modular MIMO radar at $\lambda/2$ uniform spacing, $\lambda$ uniform spacing, and non-uniform sparse array using element beampattern and array factor.	60
3.15	Comparison of measured 32 element modular MIMO radar at $\lambda/2$ uniform spacing, $\lambda$ uniform spacing, and non-uniform sparse array using element beampattern and array factor.	61
3.16	Radar connection and signal processing diagram for a single RM.	61



3.17	Photograph of the 2TX by 4RX radar electronics defining an individual RM. . . . .	62
3.18	TX and RX block diagram for an individual RM. . . . .	62
3.19	Measurement setup for the radar detection trials within an anechoic chamber with 3 RMs and three targets of dimensions: 10 cm x 10 cm, 20 cm x 20 cm and 30 cm x 30 cm. A diagram with the radar setup can be seen in appendix C . . . . .	64
3.20	Measured transmitter spectrum response for three different 2TX by 4RX MIMO RMs (see Figure 7) by sampling TX port 1 only. . . . .	65
3.21	Range accuracy comparison using one target for a distance up to 4 meters using 250MHz and 1.5GHz bandwidth. . . . .	66
3.22	Range resolution simulations and measurements with two targets separated above and below the angular resolution limit of 10 cm using a 1.5 GHz bandwidth. . . . .	66
3.23	One target comparison: $\lambda/2$ , $\lambda$ and non-uniform spacing with setup as described in C.1, just for one target. . . . .	67
3.24	Radar measurement comparison for an 8 degree angular target separation: $\lambda/2$ , $\lambda$ and non-uniform spacing. It should be mentioned that grating lobes are observed for the $\lambda$ spaced array at about $\pm 60^\circ$ while the radar measurement with the non-uniform receiver array clearly distinguishes the targets and where grating lobes and SLLs are about -10 dB or lower. The setup is presented in Fig. C.1 . . . . .	68
3.25	Radar measurement comparison for a 6 degree angular target separation: $\lambda/2$ , $\lambda$ and non-uniform spacing, which, is the only effective radar antenna which can clearly distinguish the two targets; i.e. the non-uniform spaced array. The setup is presented in Fig. C.1 . . . . .	69
3.26	Radar measurement comparison for a 4 degree (or $\pm 2$ degrees) angular target separation: $\lambda/2$ , $\lambda$ and non-uniform spacing. Again, similar to Figure 3.25, the non-uniform spaced array is the only virtual receiver than can decipher the two targets and with low SLLs for the angular spectrum estimate. The setup is presented in Fig. C.1 . . . . .	70

3.27	Simulations (a) and measurement (b) results for a radar trial detecting two targets at $0^\circ$ and $65^\circ$ as identified in Figure 3.19(d). The targets have been placed at an angular separation of $65^\circ$ to highlight the improvement of the sparse array approach compared to the $\lambda/2$ -spaced and $\lambda$ -spaced uniform array. The setup is similar to the previous measurements which are described in Fig. C.1 . . . . .	71
4.1	Comparison of linear (upper) and logarithmic (lower) representations of $\text{sinc}(x)$ , $\text{sinc}^2(x)$ , $\text{sinc}^{10}(x)$ . . . . .	77
4.2	Radar configurations: a. sub-module b. complete radar. . . . .	81
4.3	Radar signal processing approach where multiplication is employed in the spectral domain. . . . .	81
4.4	FMCW MIMO radar sub-module calibrated in an anechoic chamber with antenna transmitters at the top, 8-port receiver underneath the transmitter and radar system connected with 2.92mm cables connected from the back of the radar stand. . . . .	82
4.5	Measurements for a target at broadside for MIMO radar (4TX by 8RX elements) and spectral beam pattern multiplication (4 sub-radars with 2TX by 4RX for each). . . . .	83
4.6	Template for obtaining an interpolated (a) or extrapolated (b) antenna array design for an uniform linear array (ULA), with elements spaced at $\lambda/2$ inter-element spacing. . . . .	85
4.7	Illustration of the interpolation method for predicting missing inter-array data for the improvement of detection accuracy. . . . .	87
4.8	Illustration of the extrapolation method for estimating extra-array data for the enhancement of antenna aperture . . . . .	87

4.9	Real, simulated and measured angular target estimates considering a SIMO (1TX4RX) radar configuration which identifies two targets at: $0^\circ$ and $25^\circ$ (with a theoretical resolution of $30^\circ$ ) at 24 GHz, with two extrapolants using a piecewise cubic extrapolation function: (a) SIW Transmitter and receiver array with highlighted extrapolation elements, (b) front-end configuration and illustration of the radar scenario, (c) simulations and measurements comparing the baseline and extrapolated cases. . . . .	89
4.10	Trial runs on 1x4 SIMO measurement data comparing discontinuous extrapolation functions (nearest, next and previous) and continuous extrapolation functions (linear, pchip, makima and spline) with pchip rendering an optimal response for target detection and resolution. . .	90
4.11	Simulated and measured interpolated angular target estimates considering a MIMO (2TX4RX) radar configuration which identifies two targets at: $0^\circ$ and $15^\circ$ at 24 GHz, showing a baseline and results for three interpolants using a linear extrapolation function. . . . .	90
4.12	Simulated and measured interpolated angular target estimates considering a MIMO (6TX12RX) radar configuration which identifies two targets at: $3^\circ$ and $30^\circ$ at 24 GHz, with eight interpolants using a linear extrapolation function. . . . .	91
4.13	Illustration of highly separated radar detection showing 4 point scatters.	93
4.14	Highly separated antenna configurations showing the spacing of the transmitters and receiver antennas with 10cm and 45cm apart. . . .	95
4.15	Results of highly separated radar measurements showing 10 cm and 45 cm separation (without normalisation). . . . .	96
4.16	Highly separated radar signal processing chain showing the data acquisition of each radar and post-processing for complete target detection. . . . .	96
4.17	Highly separated radar target detection of one target with multiplication. . . . .	97

4.18	Highly separated antenna configurations measurements showing two scenarios with antennas separated at either $0.5\lambda$ or 45cm apart, showing the benefit of using highly separated radar antennas. . . . .	97
5.1	Diagram showing the steps taken to apply CS reconstruction. . . . .	106
5.2	Your Algorithm for L1 (YALL1) procedure diagram. . . . .	108
5.3	Template for obtaining a sparse array design for a 2TX 4RX receiver MIMO array, with elements spaced at $\lambda/2$ inter-element spacing. . . .	111
5.4	Comparison of measured beampatterns using the element beampattern multiplied with the array factor of the configurations found in Table 5.3. . . . .	111
5.5	Simulated response for 8-element antenna receiver in u-v coordinates for complete antenna scan. . . . .	113
5.6	Measured UV response for antenna array beam steering for complete antenna scan, showing highest SLL. . . . .	114
5.7	Side lobe level response comparison for 8-element array configuration with a large separation between arrays as described in Table 5.3. . . .	115
5.8	Newly fabricated SIW transmitter and receiver antennas, and radar hardware setup for far-field measurement. . . . .	115
5.9	Simulated and measured return losses for the manufactured SIW sparse 8-element antenna array. . . . .	116
5.10	Azimuth beampattern response of 8-element SIW antenna receiver . .	117
5.11	Elevation beampattern response of 8-element SIW antenna receiver .	117
5.12	Normalised target return for frequency calibration at 200 MHz and 1.5 GHz for corner reflector with 10 cm size at 2.6 meter distance. .	118
5.13	Radar hardware setup for target detection measurement comprising of two targets positioned at 2.6m, spaced at different angle separations.	118
5.14	Final measurement for two targets spaced at 2 degrees at a distance of 2.6m as shown in Fig. 5.13, comparing delay-and-sum (DAS), compressive sensing (CS) with range resolution of 7.5cm (1.5 GHz bandwidth). . . . .	120

5.15	Final measurement for two targets spaced at 2 degrees apart at a distance of 2.6m as shown in Fig. 5.13, comparing delay-and-sum (DAS), compressive sensing with multiplication (CS+M) with range resolution of 7.5cm (1.5 GHz).	120
5.16	Measurement sweep for two targets spaced at 20 degrees apart at 2.6m as shown in Fig. 5.13, rotating the radar platform in $10^\circ$ increments, while comparing delay and sum (DAS) and compressive sensing (CS) with 7.5cm range resolution (1.5 GHz).	121
B.1	Diagram showing the multiplication scenario where the radar cross section difference between the pedestrian and the car is 10 db and the multiplication factor is set to $M = 1$ .	133
B.2	Diagram showing the multiplication scenario where the radar cross section difference between the pedestrian and the car is 10 db and the multiplication factor is set to $M = 2$ .	133
B.3	Diagram showing the multiplication scenario where the radar cross section difference between the pedestrian and the car is 10 db and the multiplication factor is set to $M = 3$ .	134
B.4	Diagram showing the multiplication scenario where the radar cross section difference between the pedestrian and the car is 20 db and the multiplication factor is set to $M = 1$ .	134
B.5	Diagram showing the multiplication scenario where the radar cross section difference between the pedestrian and the car is 20 db and the multiplication factor is set to $M = 2$ .	135
B.6	Diagram showing the multiplication scenario where the radar cross section difference between two cars is 2 dB and the multiplication factor is set to $M = 1$ .	135
B.7	Diagram showing the multiplication scenario where the radar cross section difference between two cars is 2 dB and the multiplication factor is set to $M = 2$ .	136
B.8	Diagram showing the multiplication scenario where the radar cross section difference between two cars is 2 dB and the multiplication factor is set to $M = 3$ .	136

C.1	Diagram showing the chamber setup for two targets for each of the measurements presented in previous chapter . . . . .	137
-----	---	-----

# Glossary

**ACC** Adaptive Cruise Control

**ADC** Analogue to Digital Converter

**ADAS** Advance Driver Assistance Systems

**AR** Angular Resolution

**BW** Bandwidth

**BEAMSCAN** Delay and Sum Beamforming

**CW** Continuous Wave

**CS** Compressive Sensing

**DAS** Sum and Delay Beamforming

**DoA** Degree of Arrival

**FM** Frequency Modulated

**FWHM** Full width half maximum

**FFT** Fast Fourier Transform

**FOCUSS** FOcal Underdetermined System Solver

**FMCW** Frequency Modulated Continuous Wave

**ERA** Equivalent Receiver Array

**FOV** Field-of-view

**HPBW** Half-Power Beamwidth

**LNA** Low Noise Amplifier

**LiDAR** Light Detection and Ranging

**MIMO** Multiple Input Multiple Output

**NESTA** Nestor's Algorithm

**OMP** Orthogonal Matching Pursuit

**PRF** Pulse Repetition Frequency

**PLL** Phased Lock Loop

**RCS** Radar cross section

**RIP** Restricted Isometry Property

**RM** Radar module

**RMS** Root Means Squared

**RP** Receiver port

**RR** Range resolution

**RX** Receiver antenna

**SAR** Synthetic Aperture Radar

**SIMO** Single Input Multiple Output

**SIW** Substrate-Integrated Waveguide

**SLL** Side-lobe level

**SNR** Signal-to-Noise Ratio

**SRR** Short Range Radar

**TX** Transmitter Antenna

**TDMA** Timed division multiple access

**ULA** Uniform Linear Array

**VCO** Voltage controlled Oscillator

**YALL1** Your Algorithm for  $l_1$



# List of Symbols

$\ \cdot\ $	Norm function
$\mathbf{A}$	Matrix dictionary for compressible signal
$\mathbf{A}(t)$	Boxcar apotization function
$A(t)$	Inverse Fourier transform of the smoothing function
$c$	Speed of light (m/s)
$\Delta_R$	Range resolution (m)
$\Delta(0)$	Maximum distortion
$\delta_{1/2}$	Relative distortion at FWHM
$\delta$	Detection threshold
$D$	Duty cycle
$D_{(x,y)}$	Target dimensions in x and y coordinates
$E$	Electromagnetic field
$E(f)$	Frequency domain signal
$f_c$	Carrier frequency (Hz)
$f_b$	Beat frequency (Hz)
$FOM$	Figure of merit
$H(x)$	Hermitian blending functions
$I(t)$	Inverse Fourier transform of the signal
$k$	Wavenumber (rad/m)
$\lambda_0$	Free space wavelength
$\phi$	Phase ( $^\circ$ )
$p(t)$	Estimated interpolated/extrapolated signal
$R$	Range to the target (m)
$Q$	SNR enhancement

## *List of Symbols*

$s(t)$	Received signal in time domain
$\Theta_{3dB}$	Half power beamwidth ( $^{\circ}$ )
$\Theta_{FOV}$	Field of view ( $^{\circ}$ )
$\tau$	Delay to the target (s)
$\mathbf{x}$	Original compressible signal
$(x, y)$	Antenna element coordinates
$\mathbf{y}$	Measurement vector for compressed signal
$y(\phi)$	Steering vector
$W(f)$	Frequency domain smoothing function
$\omega$	Angular frequency (rad/s)

# Chapter 1

## Introduction

### 1.1 Motivation and goal

In this chapter, a short account will be given on the importance of radar systems in the automotive industry, its emergence and key role in avoiding collisions, while creating the path to the development of autonomous systems. This chapter presents the motivation for this thesis and highlights the key findings of the work, while focusing on the breakdown of the thesis structure and main content.

### 1.2 Background

Automotive radar systems are primarily used as sensors for Autonomous Driving Assistance Systems (ADAS). Sensors such as cameras or laser imaging, detection, and ranging ("LiDAR") gather complementary data to enable a holistic data acquisition process called "sensor fusion" [1.1]. This process leverages machine learning algorithms to react in case there is any danger present. Radars are considered essential in the detection of other cars, pedestrians or other objects for the collision avoidance process [1.1, 1.2]. Radar sensors are used in conditions where other sensors such as cameras and LiDAR underperform. Radar networks (such as the one shown in Fig. 1.1) are combining several streams of data which is usually later processed in a process called "sensor fusion". This solution is attractive since multiple sensors offer diversity, which can lead to improved angular performance in particular if the whole network of sensors has a wider span than the sensor's span [1.1]. In

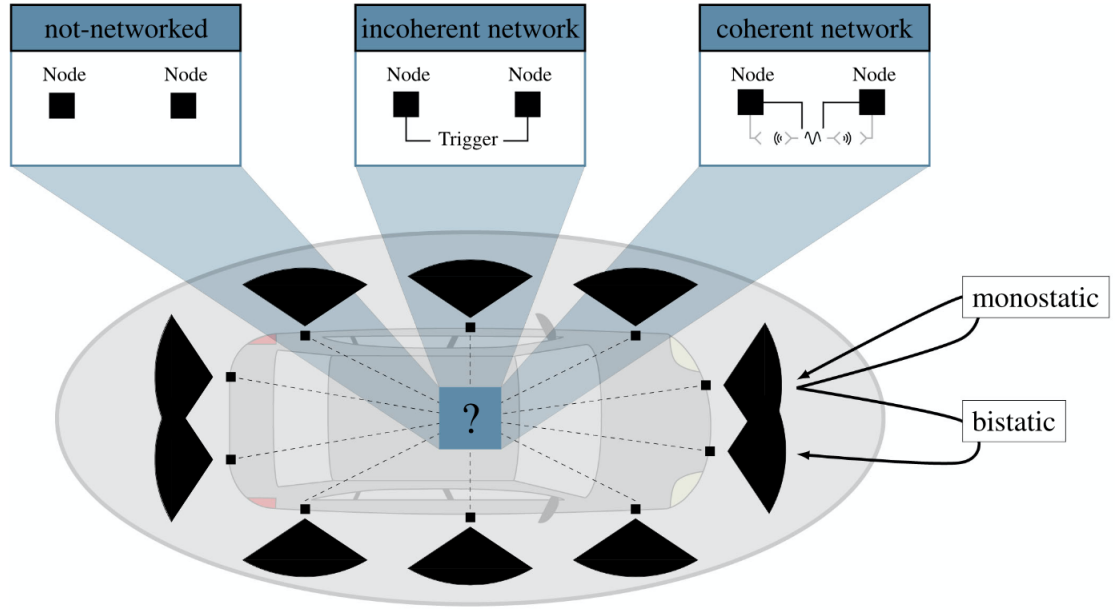


Figure 1.1: High abstract layers are implemented more frequently in today's automotive radar [1.1].

literature, radar systems with several separated sensors is called a radar network. These sensors create a fusion which is can be coherent or incoherent as depicted in Fig. 1.1.

Several factors have resulted in the progress of automotive radar systems: the development of monolithic microwave integrated circuits (MMICs) which operate from 300 MHz to 300 GHz and are based on silicon technology which can be mass-produced, the requirements set by the European New Car Assessment Programme (EuroNCAP) on automotive safety, the advancements of the antenna systems such as planar antennas with a reduced fill factor, and improved back-end digital signal processing techniques for advanced machine learning algorithms, as well as the appearance of 5G connected vehicles. Research for radar has boosted in the automotive sector. Market research companies such as Yol  Development closely monitor the electronics industry especially in the automotive market. Their report is that the automotive radar market is still expanding with a rate of 19% per year despite the shortages with COVID-19 [1.2]. The total cost of these sensors on an individual car is forecast to reach \$10,000 by 2025, with an estimated 110 million radar units to be shipped that year. In [1.2], Yol  propose several directions of research and develop an automotive radar roadmap based on their experience of the radar market

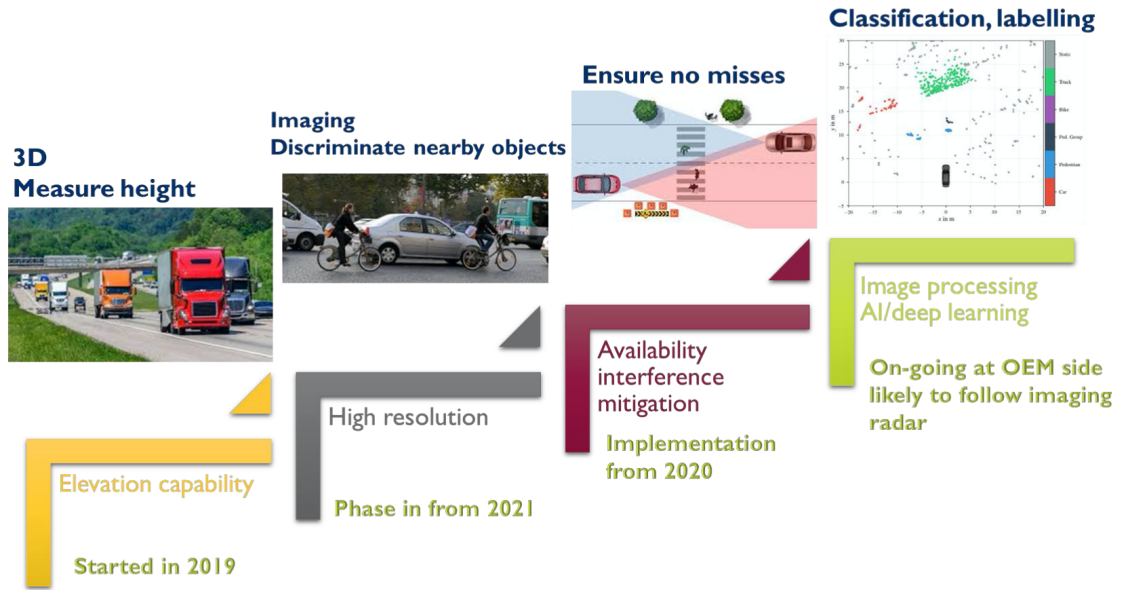


Figure 1.2: Automotive radar roadmap for next generation of autonomous vehicle systems. This figure is adopted from [1.2].

(as depicted in Figure 1.2) : 3D height measurement (elevation capability) started in 2019, discriminate nearby objects (high resolution radar imaging) phased in from 2021, ensure no misses (reduce inter-radar interference) implemented from 2020 , classification and labelling (image processing with artificial intelligence (AI)) as an ongoing development for radar manufacturers.

The gradual improvement of ADAS has made possible the pioneering of fully automated vehicles deployed on street environments, reaching Levels 4 (constant human interaction is not required) and in some cases Level 5 (driver controls are optional) [1.2]. ADAS platforms at the time of writing of this thesis are prominently based on Levels 2 and 3 of autonomy, meaning that Automated Emergency Braking (AEB) is the current standard, Automated Emergency Steering (AES) represents the next norm, while, Automated Driving (AD) is the convention of the future. Autonomous driving at Levels 4 and 5 can be assisted by sensor data fusion, with the surrounding of the car being recorded by video, LiDAR, and more conventional microwave or millimeter-wave radar [1.2]. The inclusion of all three platforms is necessary to provide adequate resolution and detection for all weather conditions including fog, rain or snow. Radar is and will stand to be an essential part of the automotive safety, with imaging becoming more predominant and essential for the

detection process.

### 1.3 Motivation and Main Contributions

When it comes to voxel perceptions per scan, microwave and millimeter-wave radar systems perform sixteen times worse than LiDAR, and approximately two hundred times worse than camera [1.3]. Achieving improved resolution for automotive radar and accurate target detection plays a key role in the progress towards autonomous driving [1.2]. Basically, the constraint with radar performance is limited by the actual physics of the problem [1.3], therefore radar performance can be improved by system design in terms of resolution, in order to precisely detect the coordinates of the targets present in the environment. The motivation is to design an automotive radar system which is able to give a fast reading of the environment, while accurately detecting multiple targets.

The following main contributions have been made towards designing a high resolution millimetre-wave radar system:

1. Design, fabrication and measurement of a substrate-integrated waveguide (SIW) sparse antenna receiver array with enlarged antenna aperture for greater radar angular resolution to prove detection of two targets which are separated at  $2^\circ$  in the angular domain with the use of only 8 antenna elements and the use of compressive sensing reconstruction.
2. Design of a radar post-processing smoothing function using beam pattern multiplication which improves side-lobe level (SLL) response for radar measurements, which lead to the use of another algorithm using a 4x4 Butler matrix radar detector, for increased angular resolution.
3. Radar system measurements with a multiple-input multiple output (MIMO) substrate integrated waveguide (SIW) frequency modulated continuous wave (FMCW) system in an anechoic chamber environment and characterisation of a 24 GHz radar system, using SIW antennas using 6.3% impedance percentage bandwidth (1.5 GHz), for increased range resolution.

In this thesis, Doppler velocity is not investigated since it is not possible to measure it using the existing facilities at Heriot-Watt and additional efforts are

needed to validate simulation results of the metric. Hence, only angular and range measurements will be presented in this thesis. However, a detailed description on how to theoretically calculate them are found in Chapter 2 (2.4.1).

## **1.4 Thesis Outline**

The remainder of this thesis contains the following:

## **Chapter 2**

This chapter introduces the concepts of millimetre-wave radar, and briefly describes the theory behind the use of FMCW MIMO radar transmission and reception, which is a key aspect in understanding the work presented in this thesis. Digital beamforming is also presented as the means of processing the raw data acquired by the radar and determining the points in the environment of maximum signal return. Other relevant technologies are presented for antenna design: SIW technology, MIMO systems, an overview of sparse-array design and compressive sensing as an alternative to conventional digital signal processing techniques.

## **Chapter 3**

This chapter presents the novel antenna MIMO design which was first developed for FMCW MIMO radar operating at 24 GHz, and which had improved range resolution and angular resolution, due to the enlarged aperture formed with the MIMO array in the time domain. This work has been presented in [1.4]. The chapter later presents a new concept, called a sectorized radar system which enhances the field-of-view (FOV) of the radar system by using multiple radar modules which are assigned to different areas of the visible range of the radar, making it possible to have a wide detection area, and also increased angular resolution with the use of a two-tier detection system which is able to replicate the behaviour of a non-uniform sparse array radar system. This work has been presented in [1.5].

## Chapter 4

This chapter introduces the signal processing techniques used for digital beamforming in order to detect the positions of the targets in the angular domain. Classical beamforming approaches are presented, but also new techniques are introduced: interpolation/extrapolation of antenna element arrays for a MIMO radar system (presented in [1.6]), spectral smoothing with the use of beampattern multiplication (presented in [1.7]) and highly separated antenna systems which are able to detect targets with an improved response due to the reduction of the coupling between the elements.

## Chapter 5

This chapter presents the sparse sensing approach to automotive radar using the FMCW MIMO radar system and also applying a compressive sensing algorithm called ***Your L1 Algorithm***(YALL1). The advantages and disadvantages of this approach are highlighted in this chapter. The results of this solution are considerably improved in comparison to standard solutions since the sparse reconstruction is able to detect targets even with reduced data sampling points. The work has been presented in [1.8].

## Chapter 6

The final chapter of the thesis presents a summary of the results, main contributions, and the possibility of future work for the discussed topics.



# Chapter 2

## Background

### 2.1 Motivation and goal

This chapter introduces radar systems for automotive collision avoidance applications. The goal of this chapter is to give the reader basic understanding of radar mechanics, what are the performance indicators of these types of radars in order to correctly identify the opportunities of improvement. Basic concepts of radar system design are mentioned and explained, as well as the basic principles behind radar signal processing, the way information is perceived from the environment, and how the radar makes use of the signals in order to produce meaningful content. The motivation is to make the reader confident about radar metrics and with the basic principles understood, he/she is able to appreciate the efforts of the works presented in subsequent chapters.

#### 2.1.1 Chapter outline

This chapter will present the radar concept, outlining the types of radars available, focusing on Multiple-Input Multiple-Output (MIMO) radar and frequency modulated continuous wave (FMCW) radar. Then a discussion is made on the importance of antenna placement for these types of devices. In the introduction, a classification of MIMO antenna placement is made for colocated MIMO radar and widely separated MIMO radar. Then, this chapter discusses the dominant techniques found in literature for achieving high performance automotive radar sensors. Both hardware and software processing techniques are highlighted. This chapter will also introduce

the most recent and influential works in MIMO automotive radar to date, having illustrated the benefits of several radar sensors and how these are compared with the work presented in this thesis. This chapter also describes the classical MIMO approach for automotive applications and presents inter-element antenna array spacing as the foundation for the sectorized radar system described in Chapter 3 as well as the non-uniform spaced array presented in Chapter 5.

## 2.2 Radar in History

Electromagnetic signals have seen multiple uses over time. For example, they can be used to carry information for radio or mobile communications. Another use of electromagnetic waves is to quantify back-scattered signals from objects to detect their presence. This is the motivation for building a radio detection and ranging (radar) device which is able to sense information about a target location. Historically, RADAR had a major influence on the outcome in the Second World War (WWII) in the Battle of Britain (1940). Scottish radio engineer Sir Robert Watson-Watt, built an entire network of early-warning radar stations, to remove the necessity of airborne flight patrols. These were called Chain Home (CH) and Chain Home Low (CHL) and covered the area surrounding the English Channel, as well as adjacent zones of Great Britain. The Royal Air Force was able to save half of its fleet of pilots, compared to the German fire fighters. This led to Britain's success since it was technologically more advanced with long distance object detection.

Nowadays, radars are indispensable working units of air-traffic control systems, collision avoidance systems in automotive driving applications, motion sensing, speed-camera tracking, space applications and many others.

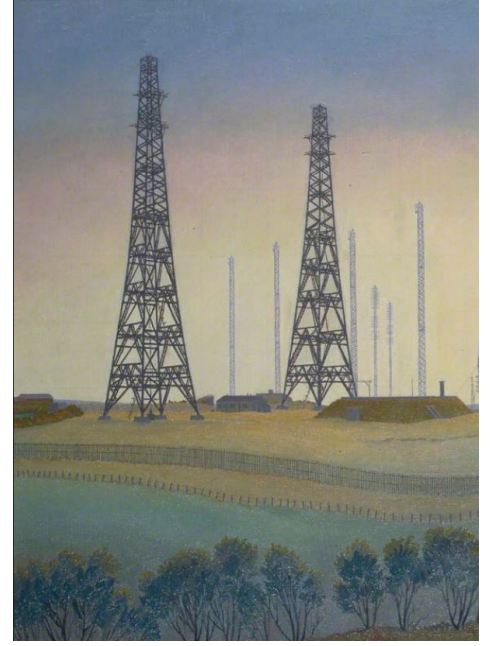
## 2.3 Radar Basics

A radar can send signals which can be synchronously or asynchronously processed. Synchronous types of radars are named **coherent** due to the nature of the architecture which allows only signals defined to a reference to be processed.

A radar is a complex system formed of a **transmitter** and a **receiver** and



(a) Map of Chain Home radar system



(b) Chain Home radar towers

Figure 2.1: British defence radar systems used in World War II [2.1].

signal processing blocks. Each of the blocks has significant impact on RADAR performance. When the transmitter emits electromagnetic waves, the target reflects a fraction of the electromagnetic waves to the receiver.

Because electromagnetic (EM) waves travel at the speed of light, the round-trip distance is twice the distance to the target for monostatic radar. Once the signal is received, it is then amplified, and digitized with the help of an analogue-to-digital converter (ADC). This signal (the raw digital data) is then transferred to the signal processing block, where it is processed for range, velocity and angle of arrival.

Types of radars are also able to determine the angular position of the target (not only range and speed). This is possible by analysing the phases between receiver antenna returns. This assumption is valid only for radars which have two or more elements at the receiver array, such as a phased array antenna. The process of identifying the direction of a phased array antenna is called beamforming.

## 2.4 Radar Types

### Pulsed Radar

A Pulsed radar is a type of radar where the signal is transmitted at a constant rate and the target backscatters returns in-between pulses. These systems are simpler to understand than CW systems, but more expensive to design and manufacture.

A Pulsed radar usually sends a signal to the target and expects to get a reflection until the next pulse is send. Pulses can be sent synchronously or asynchronously, but the target will always be detected in the window between two pulses. The frequency at which a pulse is send is usually referred to the Pulse Repetition Frequency (PRF), defined as:

$$\text{PRF} = \frac{D}{\text{Pulse width}} \quad (2.4.1)$$

where D represents the duty cycle and the Pulse width is the pulse width of the signal. The range of targets for pulsed systems can be calculated using the time it takes to reach the target and back. The method of detection in pulsed radar is called time gating. The range to the target can be calculated with:

$$R = \frac{t_{echo} \cdot c}{2} \quad (2.4.2)$$

where c is the speed of light (approx.  $3 \times 10^8$  m/s), R is the range to the target, and  $t_{echo}$  is the time delay to the target.

### Continuous Wave (CW) Radar

This type of radar emits energy continuously and listens for any target returns. CW radars are widely used in applications such as door openers for large retail stores, police speed cameras and collision avoidance in cars.

### Frequency Modulated Continous Wave (FMCW) Radar

FMCW radars are an inexpensive solution which are also easy to fabricate and they are the most used form of CW radar in use today [2.2]. FMCW radars have the

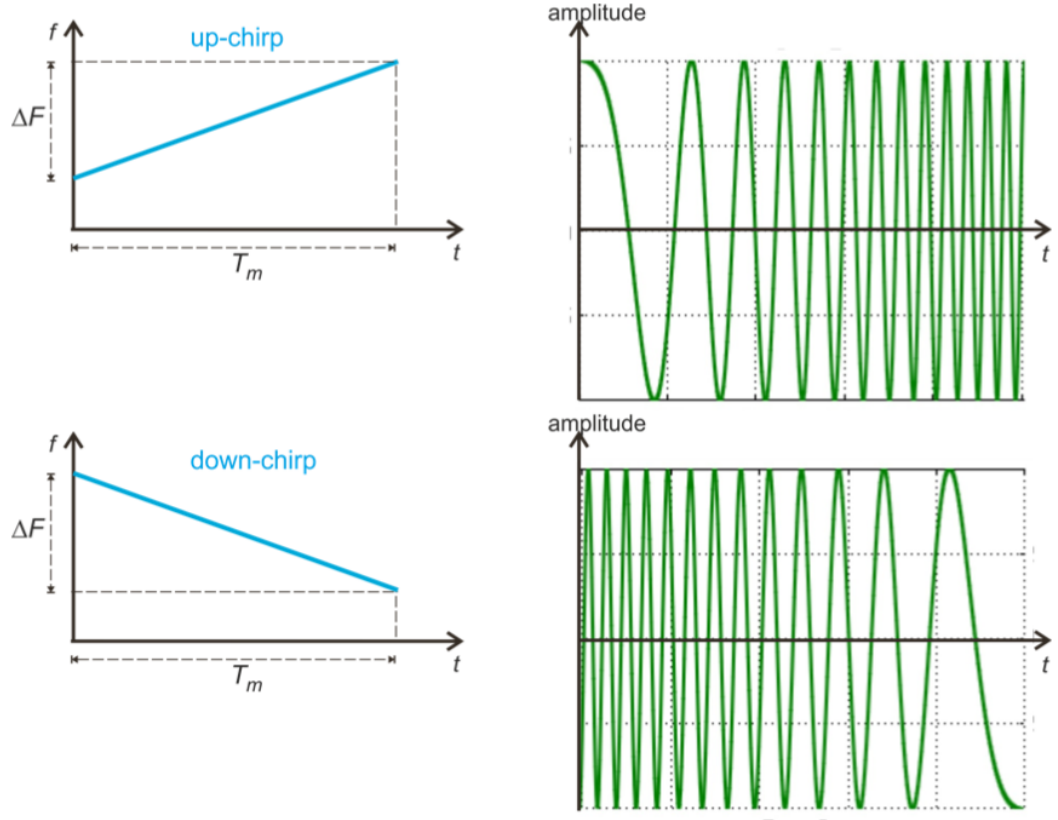


Figure 2.2: Illustration of linear frequency variation with time, for a linear FM modulation as found in [2.2].

same basis as pulse compression, but it varies frequency as a function of time. This way, a particular value of frequency is associated with a delay which translates in range. Fig. 2.2 shows the linear FM signal.

where  $\Delta_F$  is bandwidth and  $T_m$  is the chirp period. When sending a signal to an object and back, we can assume there will be a delay which also translates a frequency change. This instantaneous difference in frequency between transmitted and received signal at a point in time is called the beat frequency ( $f_{beat}$ ). The delay between the transmitted and receive signal is called the echo delay ( $t_{echo}$ ), and represents the time for the signal to echo to the target and back to the receiver. The problem is that  $t_{echo}$  cannot be measured directly.

### 2.4.1 Measuring distance

**Assuming that the targets are static**, by measuring the beat frequency, we are able to determine the range  $R$  by relating to the time for the signal to be echoed

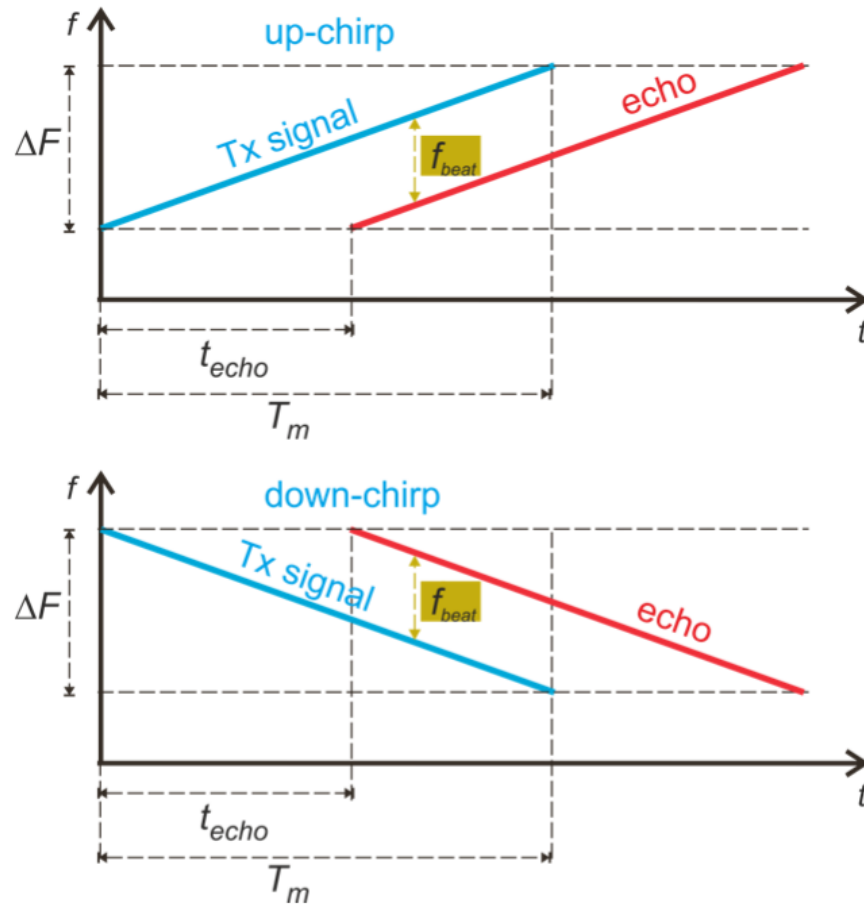


Figure 2.3: Illustration for a FMCW detection and determination of range as found in [2.2].

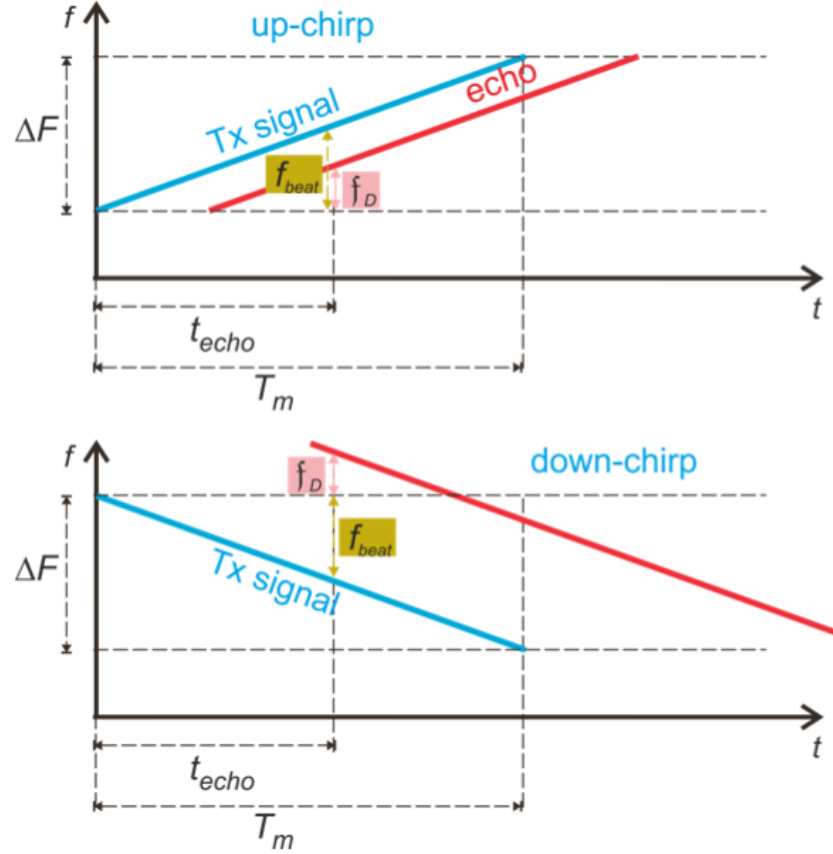


Figure 2.4: Illustration of Doppler effect as found in [2.2].

back. We already know  $T_m$  and we are looking to determine  $t_{echo}$  by looking at the direct relationship between period, frequency, delay and change in frequency:

$$\frac{t_{echo}}{T_m} = \frac{f_{beat}}{\Delta F} \quad (2.4.3)$$

The two terms  $T_m$  and  $\Delta F$  formed an enlarged triangle formed by  $t_{echo}$  and  $f_{beat}$ . The range of the static target thus becomes:

$$R = \frac{T_m}{\Delta F} \cdot \frac{c \cdot f_{beat}}{2} \quad (2.4.4)$$

## 2.4.2 Doppler shift

In case we have moving targets we will notice an effect in frequency called the Doppler effect or shift. In this case, the received signal is offset-ed with a frequency deviation called the Doppler frequency ( $f_D$ ) and this can be seen in Fig. 2.4. The total frequency deviation thus becomes:

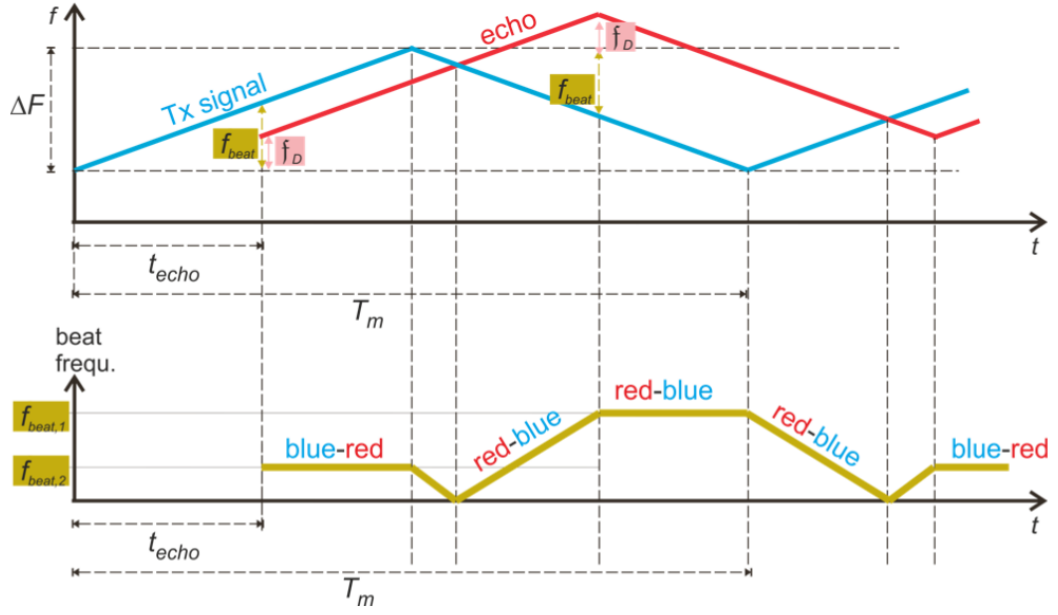


Figure 2.5: Solving for the Doppler effect using the up and down chirps of a triangular FMCW signal as found in [2.2].

$$f_{beat} = \frac{\Delta F}{T_m} \frac{2R}{c} + \frac{2v_r}{\lambda} \quad (2.4.5)$$

where  $v_r$  is the target velocity,  $\lambda$  is the wavelength. In this case we have one equation with two unknowns, since we do not know the range and the target velocity. One method to determine both variables is to consider up and down chirps in the case of a triangular FMCW waveform as seen in Fig. 2.5. The up and down beat frequencies are thus defined as:

$$\begin{aligned} f_{beat,up} &= \frac{\Delta F}{T_m} \frac{2R}{c} - \frac{2v_r}{\lambda} \\ f_{beat,down} &= \frac{\Delta F}{T_m} \frac{2R}{c} + \frac{2v_r}{\lambda} \end{aligned} \quad (2.4.6)$$

Thus for a single moving target we have two equations with two unknowns (range and velocity) and thus we can find their expressions:

$$R = \frac{T_m c}{8\Delta F} (f_{beat,up} + f_{beat,down}) \quad (2.4.7)$$

$$v_r = \frac{\lambda}{4} (f_{beat,down} - f_{beat,up}) \quad (2.4.8)$$



### 2.4.3 Defining the FMCW radar signals

The linear modulated waveform or a linear chirp is a signal which has a linear variation in frequency. To better understand the concept, a sinusoidal signal is taken [2.3]:

$$x(t) = A \sin(\phi(t)) \quad (2.4.9)$$

where A is the amplitude and  $\phi(t)$  is the phase. The derivative of the phase is the instantaneous angular frequency[2.4]:

$$w(t) = \frac{d\phi(t)}{dt}, \quad w(t) = 2\pi f(t) \quad (2.4.10)$$

$$f(t) = \frac{1}{2\pi} \times \frac{d\phi(t)}{dt}; \quad (2.4.11)$$

The frequency rate or chirp rate is defined by the rate of change of the frequency[2.4]:

$$c = \frac{1}{2\pi} \times \frac{d^2\phi(t)}{dt^2} = \frac{df(t)}{dt}; \quad (2.4.12)$$

Since it is known that a LFM signal has a linear frequency response over time, we can write that signal as:

$$f(t) = f_0 + kt \quad (2.4.13)$$

where  $f_0$  is the starting frequency, k is the slope of the chirp and t is the time variable. k is defined as:

$$k = \frac{f_1 - f_0}{T} \quad (2.4.14)$$

where  $f_1$  is the stop frequency and T is the period to sweep between  $f_0$  and  $f_1$ . Since the frequency behaves linearly within the sweep, one is able to compute the phase of the chip by taking the time integral of the frequency.

$$\begin{aligned}
\phi(t) &= \phi_0 + 2\pi \int_0^t f(\tau) d\tau \\
&= \phi_0 + 2\pi \int_0^t (f_0 + k\tau) d\tau \\
&= \phi_0 + 2\pi \left( f_0 t + \frac{k}{2} t^2 \right)
\end{aligned} \tag{2.4.15}$$

where the linear modulated waveform signal (or linear chirp) can be written as [2.3, 2.4]:

$$x(t) = \sin \left[ \phi_0 + 2\pi \left( f_0 t + \frac{k}{2} t^2 \right) \right]; \tag{2.4.16}$$

Usually, the initial phase at  $t = 0$  is zero. The chirp is therefore an FM signal which has a linear change of rate in the frequency domain.

## 2.5 Automotive Radar Concept

The concept of automotive radar dates back from the 1970's when car manufacturers have investigated the possibility of detecting objects at a distance for collision avoidance. The first actual hardware was produced in 1998 with Daimler and this radar worked at 77 GHz [2.5]. Until 2003, car manufacturers have adopted radar hardware for executive cars in order to adapt distance without too much user interaction in adaptive cruise control (ACC) applications [2.5]. Nowadays, middle class cars include radar sensors due to the reduction in price of electronics made with mass manufacturing and their widespread adoption with car makers [2.5].

## 2.6 Key Parameters in Automotive Radar Performance

Automotive radars will vary in their performance based on specifications chosen by engineers and designers. These key parameters determine how the ADAS will react in different scenarios and it is important that adequate values are chosen especially

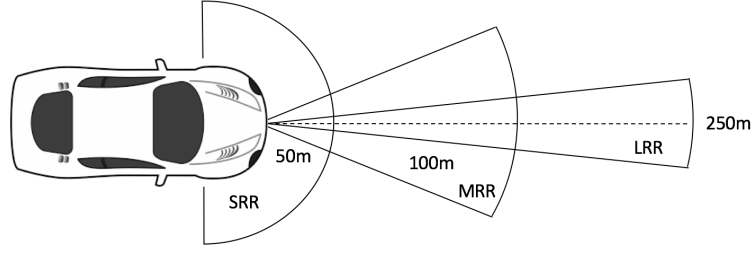


Figure 2.6: Types of automotive radar systems

in safety critical systems.

In this section, the parameters which contribute to radar performance for automotive applications are described.

## Range resolution

The first parameter a radar will be capable of displaying is the range to the target. For automotive radars, there is a clear distinction between the several types of radar:

- **Short Range Radar (SRR)**- Typically operate between 0.15m and 50m and have a wide field of view (FOV) covering up to  $\pm 80^\circ$  degrees the horizontal view. These types of radar can render high resolution since they have a narrow beam in the elevation plane but a fan beam in the horizontal plane.
- **Medium Range Radar (MRR)** - Operate between 50m and 100m and typically have less FOV in comparison with the SRR but are capable of detecting targets at longer distances. A field of view of a MRR can span between  $\pm 40^\circ$  and  $\pm 10^\circ$  in elevation.
- **Long Range Radar (LRR)** can typically detect targets up to 250m in distance and have a narrow beam both in azimuth ( $\pm 15^\circ$ ) and elevation ( $\pm 5^\circ$ ).

Although objects can be detected at a certain range, it is important to quantify how many targets the radar is able to detect a certain distance. This is called the range resolution ( $\Delta R$ ). As an example, if two targets are located at 0.5m apart, but the radar has only 1m range resolution, then the two targets will be detected as a single target. It is desired to have a range resolution which is as small as possible. The formula for radar range resolution is [2.6]:

$$\Delta R = \frac{c}{2B} \quad (2.6.1)$$

where  $c$  is the speed of light, and  $B$  is the bandwidth of the transmitters and receivers. Typically, SRRs have higher range resolution than LRRs, with values ranging from 10cm to 0.5cm depending on the bandwidth.

## Design frequency

Two millimetre frequency bands are predominant in automotive radar systems: 24 GHz (Ka-band) and 77 GHz (W-band). The 24 GHz frequency band has been chosen by the European Telecommunications Standards Institute (ETSI) as a temporary measure to prepare radars to work between 77-81 GHz [2.7]. Future radar systems will not be allowed to use 24 GHz technology because frequencies up to 40GHz will be dedicated for millimetre wave communications. If radars are used at this frequency, the beams will interfere, therefore ETSI has scheduled that all radars working at 24 GHz will have to have special permission to continue production [2.8].

The 24 GHz frequency band was initially adopted in order to allow car manufacturers to develop technology without the high costs of W-band production, since the technology at higher frequencies adds extra cost. The transition between the two frequencies would be less difficult and would allow decreasing the cost of higher frequency components. Since the wavelength at 77 GHz is smaller than the 24 GHz wavelength, radars at higher frequencies are three times smaller than an equivalent 24 GHz radar, hence the footprint is small [2.8].

## Bandwidth

Bandwidth plays an important role in the range resolution of the radar and its performance. According to the official standards, the radar bandwidth is limited at 250MHz for 24 GHz radars which use the industrial, scientific, and medical radio band (ISM band)[2.7]. This is only a temporary measure set by the European Standards Telecommunications Institute (ETSI) and this ended in January 2018. The maximum effective isotropic power which could be used was limited to 20dBm[2.8].

A ultra wide band (UWB) frequency spectrum is also available from 22.65-25.65 GHz, but should be shared with other applications. For 77 GHz radars, a frequency band of 1GHz has been allocated between 76 and 77 GHz, with an ultra

wide band option available from 77 GHz-81 GHz[2.8]. The EIRP is limited to 40 dBm. [2.7]

## Radar field-of-view (FOV)

The radar FOV is defined as the angular section over which the the main beam can be steered in order to illuminate the target [2.6]. When an array of antennas is steered electronically, a phase shift is applied to sensor elements which will affect the array factor of the antenna array to 'look' in a certain direction. This is illustrated in Figure 2.7.

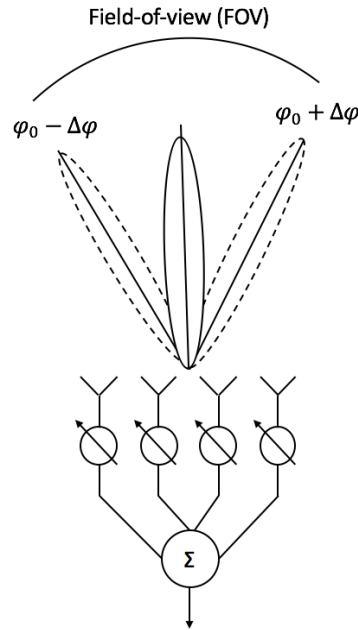


Figure 2.7: Radar Field-of-view (FOV)

## Angular resolution

The antenna array of the radar will transmit a number of waves which will travel different paths, some combining constructively and others destructively. At certain points, the amplitude of the antenna response decreases and becomes a perfect null (where the waves completely cancel). The distance between two nulls on either side of the normal of the antenna define the main lobe of the antenna [2.6].

After the angular position of the first null, waves partially construct into lobes which are less in amplitude than the main lobe and they are usually preceded and

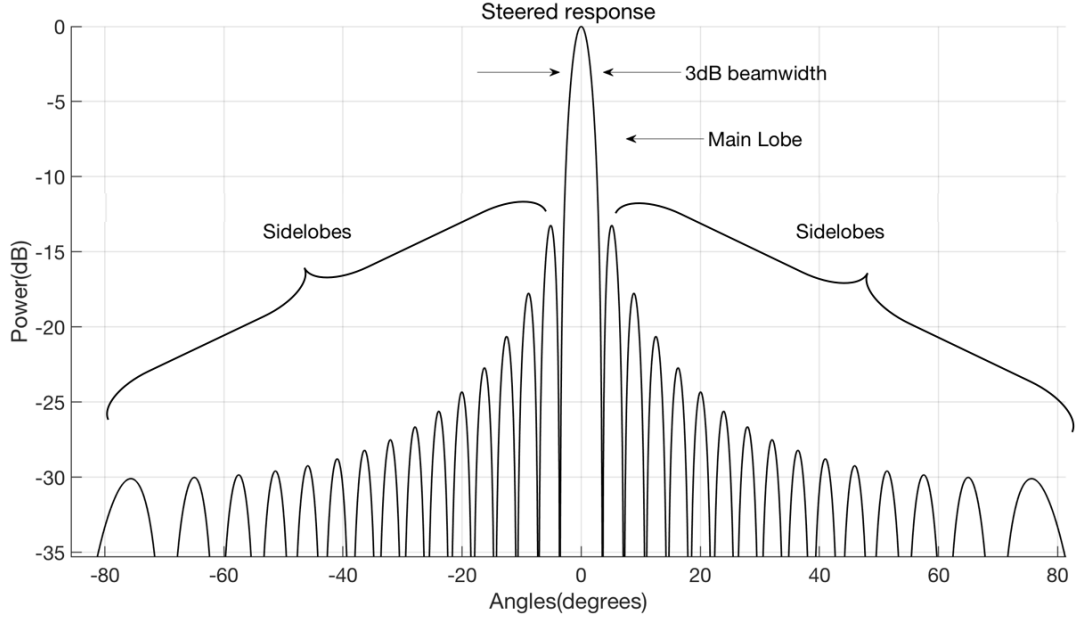


Figure 2.8: Angular resolution

followed by nulls. These lobes are called sidelobes and it is better for a directive array to have as low side lobes as possible [2.6].

Antenna arrays are sets of antennas combined to output an improved response compared to a single element. Phased arrays are steered by changing the phases between elements as seen in Figure 2.7. The output of the phased array is obtained by directly summing the signals from  $N$  elements [2.9, 2.10].

$$E_a = \sum_{k=1}^N \sin(\omega t + \phi_k); \quad (2.6.2)$$

From the wavefront arriving at element  $K=1$ , an additional phase of  $\psi$  will be added to each element of the array while the last element will have phase equal to  $\frac{(N-1)\psi}{2}$ . Therefore, the output will have the form:

$$E_a = \sum_{k=1}^N \sin(\omega t + k\psi - \frac{N+1}{2}\psi); \quad (2.6.3)$$

For two elements, this will translate in adding two phase shifts:

$$E_a = \sin(\omega t + \frac{\psi}{2}) + \sin(\omega t - \frac{\psi}{2}); \quad (2.6.4)$$

By applying trigonometric identities, the output field pattern can be rewritten

as:

$$E_a = \sin(\omega t) \frac{\sin(2\psi/2)}{\sin(\psi/2)} \quad (2.6.5)$$

In the general case, for an N-element array, the numerator will be changed as to reflect the N-elements of the sensor array[2.10, 2.9]:

$$E_a = \sum_{k=1}^N \sin(\omega t + k\psi - \frac{N+1}{2}\psi) = \sin(\omega t) \frac{\sin(N\psi/2)}{\sin(\psi/2)} \quad (2.6.6)$$

The output field response of the array becomes:

$$E_a = \sin(\omega t) \frac{\sin(N \frac{\pi d}{\lambda} \sin\theta)}{\sin(\frac{\pi d}{\lambda} \sin\theta)} \quad (2.6.7)$$

and  $|E_a(\theta)|$  is the magnitude of the field intensity pattern[2.10, 2.9]:

$$|E_a(\theta)| = \frac{\sin(N \frac{\pi d}{\lambda} \sin\theta)}{\sin(\frac{\pi d}{\lambda} \sin\theta)} \quad (2.6.8)$$

To obtain the radiation pattern of the antenna, the field pattern must be normalised and squared:

$$G_a(\theta) = \frac{|E_a(\theta)|^2}{N^2} = \frac{\sin^2(N \frac{\pi d}{\lambda} \sin\theta)}{N^2 \sin^2(\frac{\pi d}{\lambda} \sin\theta)} \quad (2.6.9)$$

The aperture of the antenna is  $L = N d$ , and the small angle approximation can be applied ([2.10]) where  $\sin(\theta) = \theta$ . Hence:

$$G_a(\theta) \approx \frac{\sin^2(\frac{\pi L}{\lambda} \sin\theta)}{(\frac{\pi L}{\lambda} \sin\theta)^2} \quad (2.6.10)$$

Generally, the beamwidth of the antenna is calculated at the half-power point

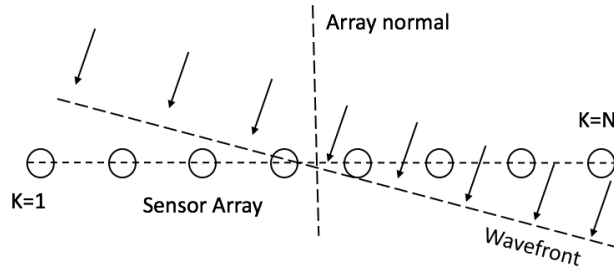


Figure 2.9: Wavefront arriving at the antenna receiver

at broadside (at the point at which the beam is steered at  $0^\circ$ ). The beamwidth increases as the beam is steered away from broadside. It is a variable which is dependent on wavelength and aperture diameter [2.10].

$$\theta_{3dB} = \arcsin\left(\frac{k\lambda}{d}\right) \quad (2.6.11)$$

where  $k$  is a constant (70 for degrees and 1.22 for radians),  $\lambda$  is the wavelength and  $d$  is the aperture of the antenna.

By rearranging (2.6.11) :

$$\theta_{3dB} = \sin^{-1}\left(\frac{\omega \lambda}{2\pi d}\right) \quad (2.6.12)$$

where  $\omega$  is angular velocity. If the elements are equally spaced and the spacing between them is  $0.5\lambda$  [2.11] then the angular resolution becomes:

$$\theta_{3dB} = \sin^{-1}\left(\frac{2}{N}\right) \quad (2.6.13)$$

The field of view (FOV) of the radar will always be positioned radially between angles  $(-\pi; \pi)$  [2.11]. Hence the FOV is defined as :

$$\theta_{FOV} = \pm \sin^{-1}\left(\frac{\lambda}{2d}\right) \quad (2.6.14)$$

If the spacing is  $0.5\lambda$  then the FOV is  $\pm 90^\circ$ .

## Digital beamforming

The digital beamforming method is similar to analogue beamforming, only that the beamforming itself is done after each of the receiver channels have been sampled with an analogue-to-digital converter (ADC). This offers a significant advantage over analogue beamforming since high resolution angle of arrival (AoA) algorithms are capable of obtaining a precise location of the target. However, the main disadvantage of this method is that the signal processing time of these algorithms makes it difficult for them to be adapted to safety critical systems. Also, for some of the algorithms, the number of targets has to be specified, information which is not always known apriori. A typical digital beamformer is depicted in Figure 2.10.



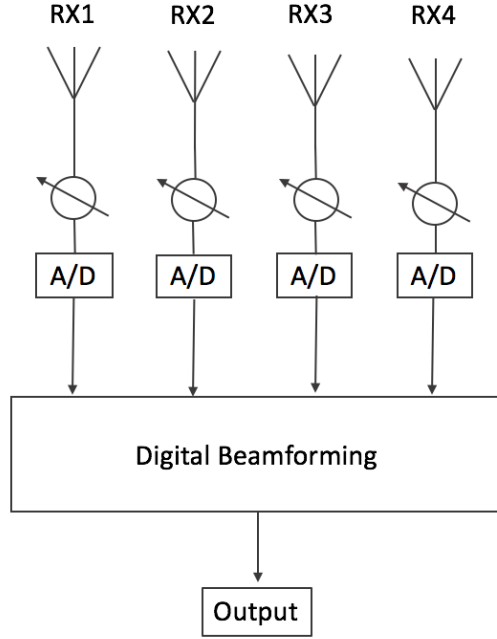


Figure 2.10: Digital beamformer

## 2.7 SIMO and MIMO radar

The concepts of SIMO and MIMO radar have seen its adoption from 1989 when a synthetic aperture impulse radar would use largely spaced arrays to continuously illuminate airborne space for detection [2.12]. Since then, MIMO radar has seen popularity in the 1990's [2.13] while today it is present in many area of radar and communication systems. The concept of MIMO radar has been adopted also in automotive radar due to the evolution of manufacturing processes (e.g. SiGe, CMOS, BiCMOS etx.) for on-chip technologies and the need to work at millimetre frequencies not only for automotive applications but also for communication systems in general.

### 2.7.1 Definition

The term **SIMO (single input multiple output)** is used to describe a radar system with only one transmitter and multiple receivers. **Multiple input multiple output(MIMO) radar** on the other hand can have multiple transmitters which can increase the views of the target. The principle between the two is orthogonal transmission and reception in either time, space or phase. In effect, a reduced number of elements is used for a wide virtual antenna aperture. Figure 2.11 illustrates

the two SIMO and MIMO configurations.

MIMO radar is a technology which uses multiple receivers and transmitters in order to take advantage of spatial diversity and illuminate several areas of the target.

SIMO radars are conventional radar configurations which have one transmitter and usually equally spaced receivers defined as a uniform linear array (ULA). MIMO radars, on the other hand, can provide increased angular resolution for automotive detection systems because these radars can emulate an increased aperture size for the receiver antenna array [2.14]. MIMO systems also combine the advantage of using multiple reflections from transmit/receive paths. The targets are illuminated successively from different views, taking into account the positioning of the antenna sensors [1.1].

MIMO antennas also bring more spatial diversity. Emerging antenna designs provide beamsteering which can improve radar resolution in addition to the transmitted power distribution [2.15]. MIMO systems have also seen a proliferation among radars designed for automotive applications [2.16, 2.17, 2.18]. This is especially true due to the well-known principles behind MIMO processing which have been adapted from digital communication systems [2.19, 2.15, 2.20]. The advantage of using MIMO radar front-ends is also related to the increased illumination of the target for a defined FOV. At the same time, MIMO systems use the spatial antenna distribution to increase the virtual aperture length by convolving the antenna signals. Furthermore, signal orthogonality is key to multi-antenna transmission systems, especially when concurrent transmission is taking place. The received signal strengths vary for different radar cross sections (RCS) of the targets, however increased aperture length improves angular resolution.

According to the MIMO theory described in [2.21], the positions of the  $N_{TX}$  transmitters, together with the positions of the  $M_{RX}$  receivers constitute an equivalent array, also termed a virtual array with the following steering vector:

$$\mathbf{y}(\phi) = e^{i \frac{2\pi}{\lambda} (d^{Tx} \oplus d^{Rx})_u}, \quad (2.7.1)$$

where  $d^{Tx}$ ,  $d^{Rx}$  are the transmitter and receiver antenna element separations, and  $(d^{Tx} \oplus d^{Rx}) = (d_1^{Tx} + d_1^{Rx}, d_1^{Tx} + d_2^{Rx}, \dots, d_N^{Tx} + d_M^{Rx})$  represents the antenna virtual array configuration based on the convolution of the transmitter and receiver antenna

array elements. The aperture of this equivalent virtual array has a total number of  $N_{TX} \times M_{RX}$  element positions. The advantage of using this MIMO configuration is the reduced sensor footprint and RF hardware requirement when compared to an equivalent uniform linear array of the same size. In general, it is expected that for an array of size  $N_{TX} \times M_{RX}$  antenna sensors, the total physical area is reduced to only  $N_{TX} + M_{RX}$  antenna sensors for the radar front-end.

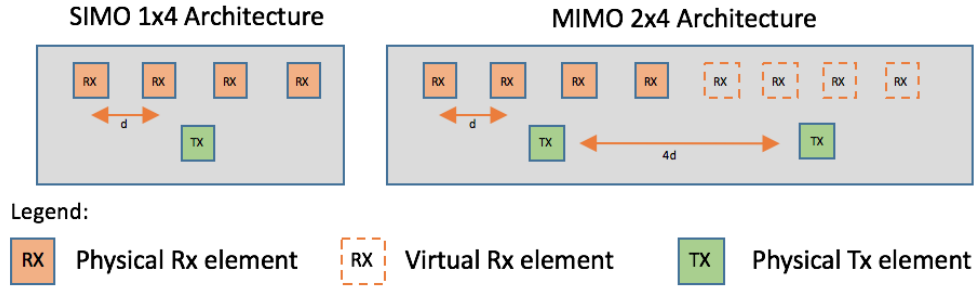


Figure 2.11: Single-Input Multiple-Output and Multiple-Input Multiple-Output Architectures

## 2.7.2 MIMO Radar Configurations

MIMO radar can transmit multiple orthogonal signals. The next two sections will describe the advantages and disadvantages of positioning the antennas closely together (in colocated configuration) and when they are separated at a considerable distance (widely separated configuration).

### Colocated MIMO Radar

For transmitter antennas that are closely positioned (colocated), the usually are transmitting orthogonally. In addition, waveform optimisation offers an unique advantage for MIMO radars since beampatterns can be modelled with effective sensor positioning. The illustration of colocated MIMO radar can be seen in Figure 2.12a.

### Widely Separated MIMO Radar

MIMO radars with widely separated transmit/receive antennas benefit from gain diversity since each of the modules can better illuminate the target and provide a better view of the radar cross section (RCS) [2.22]. An important assumption in

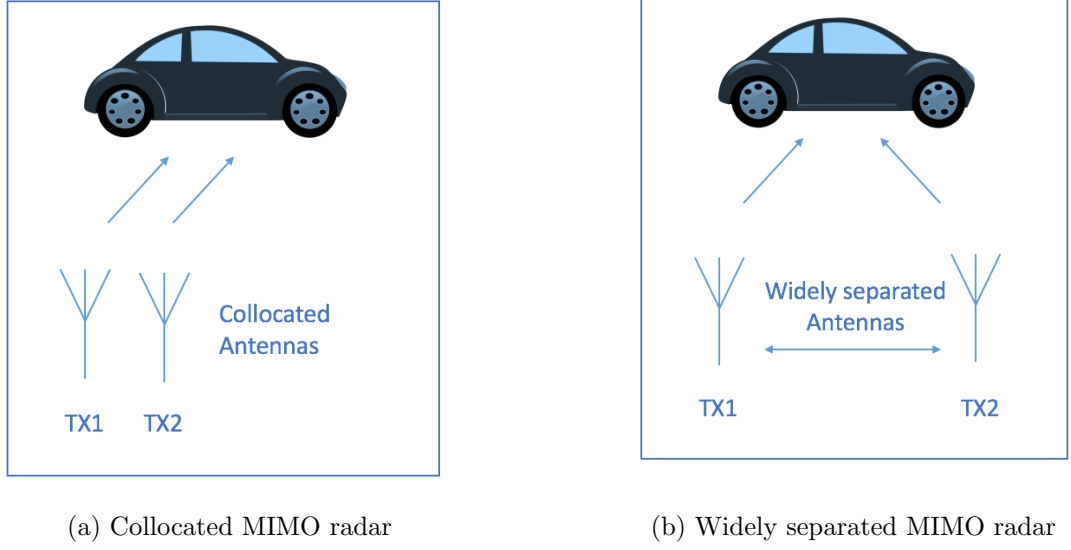


Figure 2.12: MIMO configurations

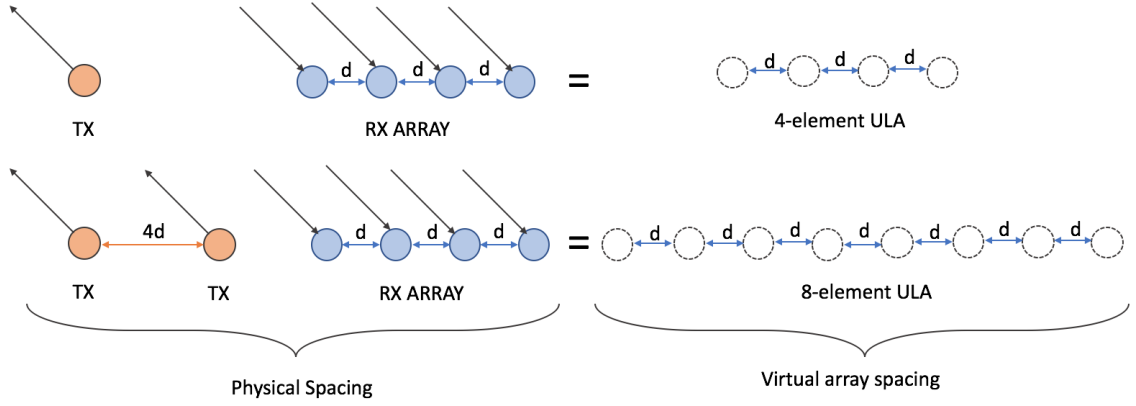


Figure 2.13: Physical MIMO spacing vs MIMO virtual array spacing

widely separated antennas is the decorrelation between antennas, which assumes that the individual views of the target are independent and facilitates non-coherent processing [2.22]. An illustration of widely separated antennas is present in Figure 2.12b.

### 2.7.3 MIMO Radar Angular Resolution Improvement

MIMO radars can improve resolution with transmission diversity. As can be seen in Figure 2.13, one transmitter which sends a signal to the target will reflect a beam at the four-element receiver. The number of transmit elements,  $N_{TX}$  is 1 and the number of receiver elements  $N_{RX}$  is 4 in this case. If the transmitter has two

elements which are spaced at a distance equal to the aperture size of the receiver (in this case four), then the equivalent virtual array will receive two beams and it will have twice the size of the receiver. Generally, if a MIMO transmission system has  $N_{TX}$  transmitters and  $N_{RX}$  receivers, then the aperture of the receiver array will have the size of  $N_{TX} \times N_{RX}$  elements [2.11, 2.13].

This property of MIMO systems allows for smaller antenna physical size with a larger virtual aperture. For radars, this property translates in better angular resolution. In Figure 2.13, the angular resolution of the SIMO system has  $30^\circ$  resolution, while the MIMO array will be able to distinguish targets at  $15^\circ$  resolution, at the expense of only a single physical element. Therefore MIMO systems achieve  $N_{TX} \times N_{RX}$  element aperture at the expense of  $N_{TX} + N_{RX}$  physical antenna elements [2.11, 2.13].

## 2.8 State-of-the-art Automotive Radars

In this section, the most recent works involving automotive radars are presented and classified. This literature review was composed of a set of 40 conference papers and journal articles [2.23, 2.34, 2.45, 2.56, 2.58, 2.59, 2.60, 2.61, 2.62, 2.24, 2.25, 2.26, 2.27, 2.28, 2.29, 2.30, 2.31, 2.32, 2.33, 2.35, 2.36, 2.37, 2.38, 2.39, 2.40, 2.41, 2.42, 2.43, 2.44, 2.46, 2.47, 2.48, 2.49, 2.50, 2.51, 2.52, 2.53, 2.54, 2.55, 2.57, 1.1] . A shortlist of 5 papers was prepared for a more detailed comparison. The papers are the most recent works of automotive radars found at the time of writing. In the classification of automotive radars, the most important factors taken into consideration were the angular resolution of the radar, range resolution, ease of manufacturing, detection time and the footprint of the antenna front end.

As a result of this review, different techniques of increasing angular resolution have been identified in both hardware and software domain. It is the focus of this chapter to identify the techniques which significantly improve radar detection.

Improving radar resolution can be achieved with several hardware techniques. The works discussed in this review achieve this enhancement by the design of the transmitter and receiver front end. It is possible to obtain accurate identification of targets even with few number of elements (e.g.  $5^\circ$  3-dB beamwidth with only 4

elements both at transmit and receive). Hence, the angular resolution of the radar can be determined by designing the aperture of the receiver antenna. The wider the aperture of the antenna, the sharper the beam and a more precise detection can take place [2.10]. The theory underlying the beamwidth of the receiver as well as how MIMO achieves better resolution have been discussed in Chapter 2. In this chapter, several techniques are presented as a way of enhancing angular resolution and range resolution.

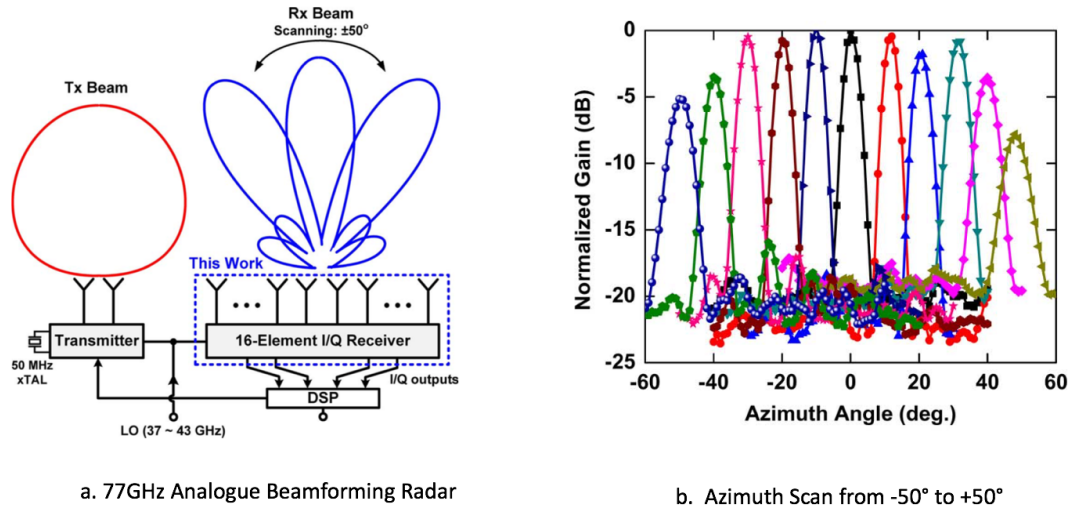


Figure 2.14: 77-81 GHz radar with 2x16 MIMO antennas [2.23]

## Analogue beamforming

The analogue beamformer adjusts the sensor arrays to position the beam in the radar's direction of maximum return. By positioning the beam in a particular direction, the target reflects energy back and this will show a peak. The target is thus identified with a minimal signal processing overhead, which makes analogue beamforming very fast.

The work presented in [2.23] shows a 2-by-16 MIMO analogue beamformer for an automotive radar working at 77-81 GHz. The FOV achieved in [2.23] is  $\pm 50^\circ$ . A microstrip patch array was employed for the antenna front end which has been manufactured in a SiGe process with wire bonding assembly. Overall, the radar is able to distinguish targets at  $5.5^\circ$  apart. The radar is able to scan in  $\sim 1^\circ$  increments. An illustration of the work in [2.23] can be seen in Figure 2.14.

## Quasi-optical beamforming

This type of beamforming requires antenna elements which are quasi-optical (they act as a lens to shape the antenna beampattern). In [2.34], a 77 GHz automotive radar is designed using on-chip glass resonators. A field of view of  $\pm 30^\circ$  has been achieved, while the angular resolution is  $4^\circ$ , which is near the theoretical limit of  $3.6^\circ$  for a virtual antenna array of 32-elements. An illustration of the work in [2.34] can be seen in Figure 2.15.

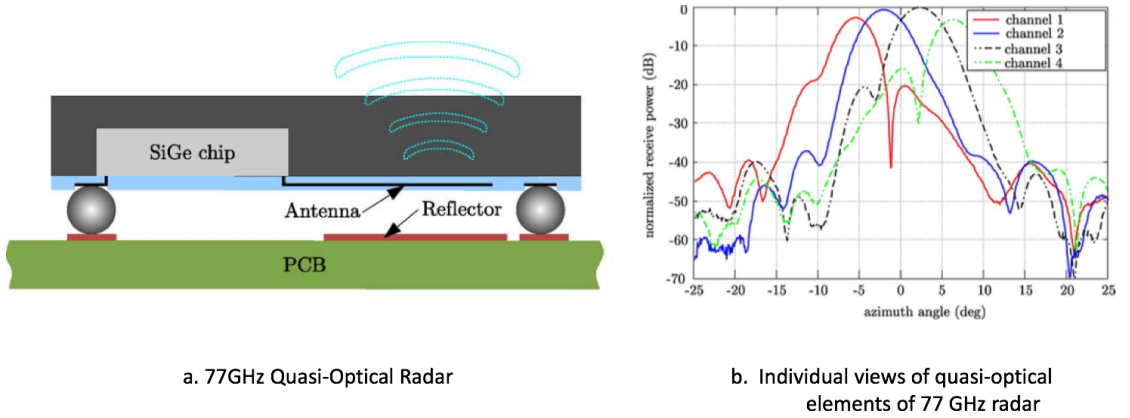


Figure 2.15: 77 GHz Quasi-optical radar [2.34]

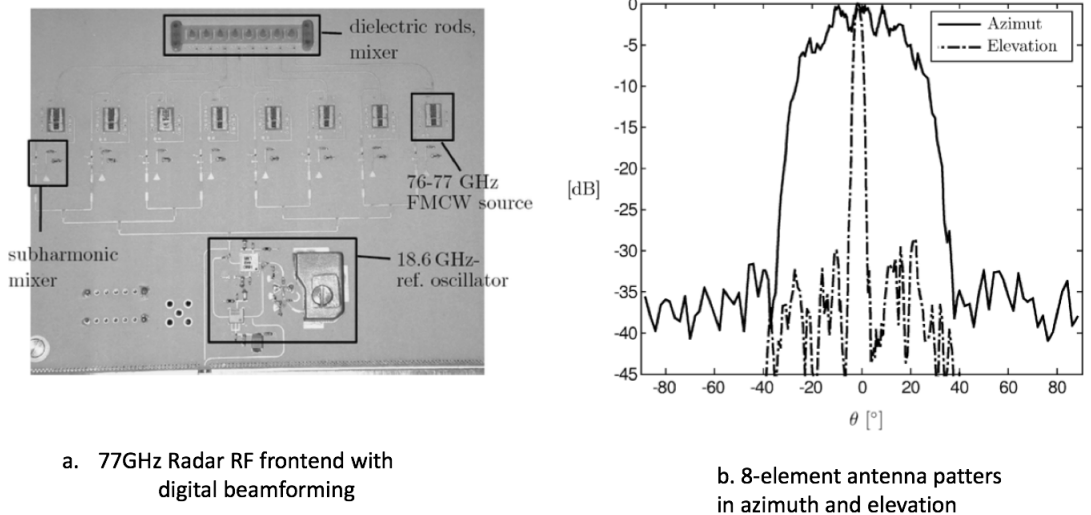
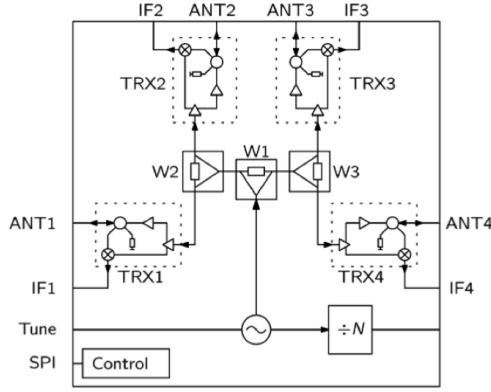


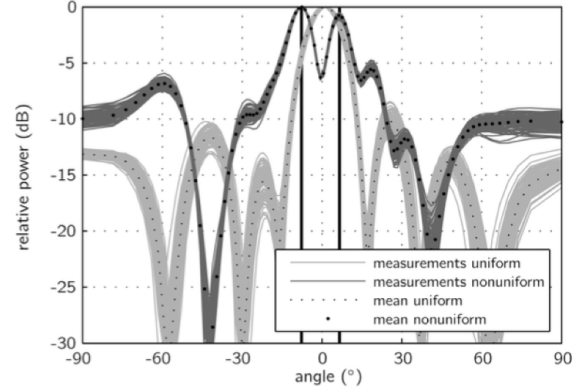
Figure 2.16: 77 GHz radar with SIMO digital beamforming [2.45]

The work in [2.45] describes a SIMO digital beamforming system which has transceiver capability (each transmitter module can also work as a receiver). The antennas were chosen to be microstrip patches with dielectric rods at half-wavelength

spacing. The total dimension of the aperture of the antenna is  $7\lambda_0$ . By applying a beamforming algorithm with Chebyshev weighting, the side-lobe level is 25 dB lower than the main lobe. In addition, the application of MUSIC high-resolution offers a sharp receiver beampattern with angular resolution of  $3.9^\circ$ . The system together with the beampatterns of the rod antennas can be seen in Figure 2.16.



a. Block diagram of 77GHz SiGe transceiver



b. Two target identification at  $-7^\circ$  and  $+7^\circ$  with uniform and non-uniform configuration

Figure 2.17: MIMO 77 GHz transceiver radar using non-uniform antenna element spacing with 4- [2.56]

## MIMO Digital Beamforming

The work in [2.56] has been positively received by the radar research community since it has been awarded the IEEE Microwave prize in 2011 due to its implementation of transmit receive modules which are able to offer a wide antenna aperture by using transmission and reception orthogonally. This automotive radar manufactured in a SiGe wire bonding technology has used only 4 elements in order to account for the performance of a 16-element uniform linear array (ULA). The unique method adopted in [2.56] uses a rat-race coupler to allow for each sensor element to be used as transmitter and receiver. This front end receiver will have  $4 \times 4$  antenna elements in the MIMO virtual space. Hence, the resolution expected for this type of radar according to equation (2.6.13) should be  $7.1^\circ$  in the  $0.5\lambda$  case. Hence, the 4 element front-end is capable of achieving the same resolution as a 32-element uniform linear array. Moreover, the field-of-view of the radar is capable of scanning  $\pm 81^\circ$  in the azimuth plane. A block diagram with the transceiver front end and two target



identification are shown in Figure 2.17.

## MIMO Digital Beamforming with Substrate Integrated Waveguide (SIW) antennas and sectorized radar

The work presented Chapter 3 of this thesis discusses a MIMO radar which has increased receiver antenna bandwidth with low radiation losses at 24 GHz. A multi-static radar (or radar network) approach has been adopted to increase the effective RCS of the target by using the concept of transmitter diversity as discussed in [2.22]. Further details of this work are presented in Chapter 3.

A MIMO FMCW radar off-the-shelf commercial system has been used in this work. Before choosing the device, a literature survey has been carried to establish the best radar available, and several works have been found suitable.

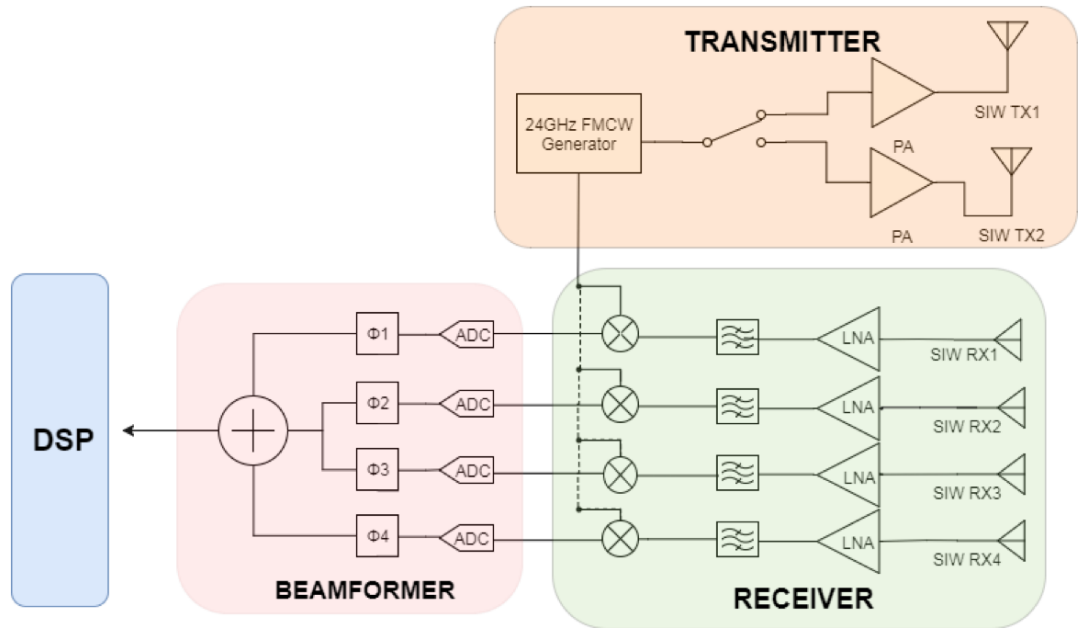
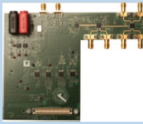
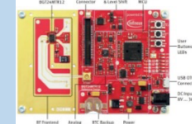



Figure 2.18: Radar architecture

An investigation was carried to find a radar capable of integrating antennas fabricated in-house, and which had documented software as well as good costumer support. A comparison of the found radar systems is shown in Figure 2.20. Overall the Radarbook automotive radar was capable of creating a 32-element virtual array ([2.63]), however, the antennas could not be changed. The Infineon evaluation board [2.21] had only SIMO capability which would have limited the scope of its use.

Therefore, in the opinion of the authors, the Analogue Devices evaluation board has been the best option for the requirements of this project since it offered 2x4 MIMO capability and well documented software. Steps have been taken to synchronise four radar boards, for a 32-element MIMO virtual array however it has not been possible to synchronise them. The problem was with the external sync since this did not offer the same clock signal to the local oscillator of the transmitter, hence it was not possible to receive the signals at the same time from different boards. However, the 2x4 MIMO radar has worked well and a modular radar approach has been taken to circumvent the synchronisation problem.

Parameter	Goals project	Analogue Devices EVAL-BOARD 	Infineon Eval Board 	RadarBook 
SISO/MIMO	MIMO	MIMO (2TX 4RX)	SIMO (1TX 2RX)	MIMO (2TX 8RX)
FoV	(+/-)65°	N/A	10° x 25° patch antennas*	(+/-)60 (with digital beam forming)
SNR	10dB	10dB	5dB	N/A
Sensitivity	(-90dBm)	(-)70dBm for 250MHz	(-)68dBm	-57 dBm(-100dBV noise floor)
Noise Figure	10dB	10dB	12dB	10dB
BW	250	250MHz	250MHz	250MHz
3-dB beamwidth	<4°	N/A	N/A	76.5 (9/element)
Range	50m	N/A	50m	40m
Gain	20dB	22dBm	26dBm	13.2dBi
Output Power	10dBm	8dBm	11dBm	8dBm
Cost Radar (1 x radar)	Reasonable	\$700	€ 1,499.00	2,565.00
Cost DSP hardware		\$400	Included	Included
Cost DSP software(MIMO)		N/A	N/A	1,045
Cost Antenna		N/A	Included	1,045
Cost Software GUI		N/A	Included	522.5
Total cost (current c.)		1,100.00	€ 1,499.00	5,177.50
Total cost (£)		£902	£1,304	£4,504

What we calculate	Legend
From other sources	
N/A	

Figure 2.19: Comparison of off-the-shelf FMCW radar systems

## 2.9 Propagation model: Two-way propagation channel model

The model used in this thesis and to carry out the simulations for the radar trials is the two-way propagation model. This is the simplest form of propagation model for a multipath channel. This model is shown in Fig. 2.19. It represents a useful propagation model, which is based on geometric optics, and considers the direct line

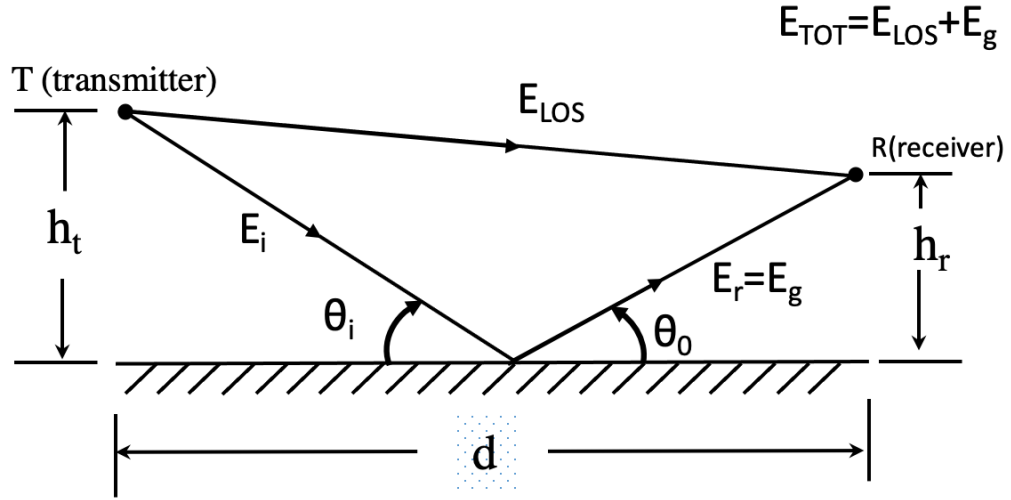


Figure 2.20: Two-ray ground propagating model taking into account multipath as found in [2.64].  $E_{TOT}$  is the total field,  $E_g$  is the ground reflected field,  $E_i$  is the incident field,  $\theta_i$  is the incident angle,  $\theta_0$  is the reflected angle,  $E_{LOS}$  is the line of sight field,  $h_t$  is the transmitter height,  $h_r$  is the receiver height,  $d$  is the distance between transmitter and receiver,  $E_0$  is the free-space electric field (in units of V/m).

of light, and the reflected propagation path between transmitter and receiver. The model is known to be accurate for predicting signal with high strength. Referring to Fig. 2.19 the E-field from a reference position  $d_0$  with a known E-field  $E_0$  is:

$$E(d, t) = \frac{E_0 d_0}{d} \cos\left(\omega_c \left(t - \frac{d}{c}\right)\right) \quad (d > d_0) \quad (2.9.1)$$

where  $\omega_c$  is the angular frequency, and  $|E(d, t)| = E_0 d_0 / d$  is the envelope of the electric field at  $d$  meters from the transmitter. There are two waves that propagate to the receiver: the direct wave (which has a distance  $d'$ ) and the reflected wave (which travels a distance  $d''$ ). The electric field which is related to the line of sight (LOS) is:

$$E_{LOS}(d', t) = \frac{E_0 d_0}{d'} \cos\left(\omega_c \left(t - \frac{d'}{c}\right)\right) \quad (2.9.2)$$

and the electric field due to the ground reflected wave is expressed as:

$$E_g(d'', t) = \Gamma \frac{E_0 d_0}{d''} \cos\left(\omega_c \left(t - \frac{d''}{c}\right)\right) \quad (2.9.3)$$

where  $\Gamma$  is the reflection coefficient for the ground. According to the laws of

reflection:

$$\Theta_i = \Theta_0 \quad (2.9.4)$$

$$E_g = \Gamma E_i \quad (2.9.5)$$

$$E_t = (1 + \Gamma)E_i \quad (2.9.6)$$

For small values of  $\Theta_i$  the reflected wave is equal in magnitude to the incident wave (and 180° out of phase). The total electric field can be expressed as a sum of Eq. 2.9.2 and 2.9.3:

$$E_{\text{TOT}}(d, t) = \frac{E_0 d_0}{d'} \cos\left(\omega_c \left(t - \frac{d'}{c}\right)\right) - \Gamma \frac{E_0 d_0}{d''} \cos\left(\omega_c \left(t - \frac{d'}{c}\right)\right) \quad (2.9.7)$$

while the resultant envelope function is  $|E_{\text{TOT}}| = |E_{\text{LOS}} + E_g|$ .

## 2.10 Radar Link Budget

After the selection of the radar hardware, a radar link budget analysis has been carried out as illustrated in Figs. 2.21 and 2.22. In addition, an amplifier has been chosen to improve receiver response (Analogue Devices HMC751LC4) and this added another 22 dB of gain. This device was necessary due to the high free space path loss (FSPL) at 24 GHz, which placed the received signal very close to the noise level, even at 1m distance.

Unfortunately, high flicker noise, demand for low noise figure, and requirements for low voltage supply as well as limited transmission power all affect the performance of the radar link budget in the case of the automotive radar [2.65]. Compensation is realised by implementing power amplifiers at the transmitter within the 30dBm limited transmission power implemented by the standards [2.66]. The received power of the radar ( $P_R$ ) is known to be [2.3]:

Look at the diagram	
1: Generated tone @ 24GHz (dBm)	-14.00
2: Gain G1	22.00
3: Gain of the Tx Module @ 24GHz (dB)	13.20
4: Space Losses @ 24GHz (dB)	94.03
5: Space Losses @ 24GHz (dB)	94.03
6: Gain of the Rx Module @ 24GHz (dB)	13.20
7: Gain G2	22.00

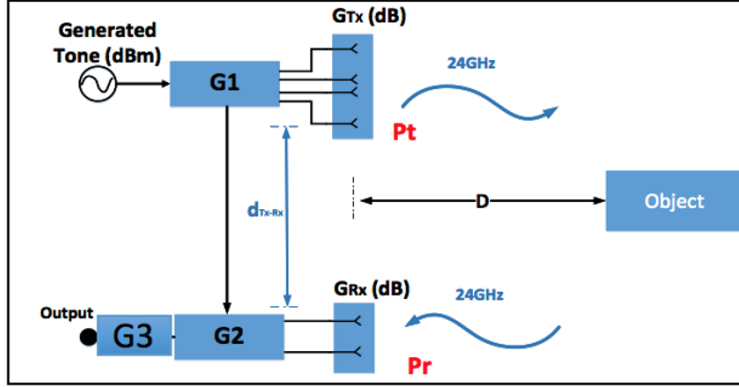


Figure 2.21: Illustration of radar link budget diagram showing all system components and values for the power budget calculation.

Radar Cross Section (in mxm)		1,5
------------------------------	--	-----

	dBm	mW
Pt	8.00	6.309573445

BW	250
SNR	10
NF	10

Distance (in m)	FSPL at 24GHz	Pr SISO in dBm	Pr MIMO in dBm	Pout SISO in dBm	Pout MIMO in dBm
5	74,03140814	-59,84	-50,84	-37,84	-28,84
10	80,05200806	-71,88	-62,88	-49,88	-40,88
20	86,07260797	-83,92	-74,92	-61,92	-52,92
30	89,59443315	-90,96	-81,96	-68,96	-59,96
40	92,09320788	-95,96	-86,96	-73,96	-64,96
50	94,03140814	-99,84	-90,84	-77,84	-68,84
60	95,61503306	-103,00	-94,00	-81,00	-72,00
70	96,95396886	-105,68	-96,68	-83,68	-74,68

What we calculate	Sensitivity (In dBm)
From other sources	-70,02059991

Figure 2.22: Calculation of received power levels for a Single Input Single Output (SISO) radar system and a MIMO radar system assuming a signal to noise ratio (SNR) of 10 dB, noise figure of 10 dB, radar cross section of 1.5m<sup>2</sup>

$$P_R = \frac{\sigma G_T G_R \lambda^2}{(4\pi)^3 L_{ATM} R^4} P_T \quad (2.10.1)$$

where  $\sigma$  is the radar cross section of the target,  $G_T$  and  $G_R$  are the transmitter and receiver gains (in this we include the amplifiers and the antenna gains)  $\lambda$  is the wavelength at 24 GHz (1.25 cm),  $R$  is the range to the target and  $L_{ATM}$  are the atmospheric losses at the carrier frequency. This equation was used when determining the received power in the the radar case for the single input single output case (SISO) or the multiple input multiple output case (MIMO) (see Figs. 2.21 and 2.22).

The free space path loss at 24 GHz is very high up to 5m, but then increases only by 6dB per decade. The anechoic chamber used in this experiment is only 5.5m long. Figs. 2.21 and 2.22 show the level of expected power for each of the antenna configurations of the radar, considering all other power levels of the system known.

## 2.11 Substrate Integrated Waveguide Technology

In order to make a good selection of antenna technology which will be used for the radar, classic technologies have been considered in the first instance in terms of antenna integration. It is preferable to integrate a technology which is compact and cost-effective when considering antennas for automotive radar. Hence, microstrip technology would be a first option. These are very lightweight, cost-effective and robust, but often exhibit coupling with adjacent lines and radiation losses at higher frequencies are very high. On the other hand, waveguides are less lossy and provide lower radiative losses at higher frequencies while providing outstanding isolation. Sadly, they are also bulky and cannot be easily integrated with mass-production radar systems which are encapsulated.

Substrate Integrate waveguide technology on the other hand can bridge a gap between the two. Instead of creating a waveguide out of hollow materials, it is possible to make a waveguide using planar technology, similar to how microstrip patch antennas are made, only that these use vias to restrict the current flow in certain areas of the antenna, while allowing more energy to be transmitted through slots present on the top layer. A simple depiction of SIW antenna can be seen in Fig. 2.23. Therefore SIW antennas can be considered as a rectangular waveguide

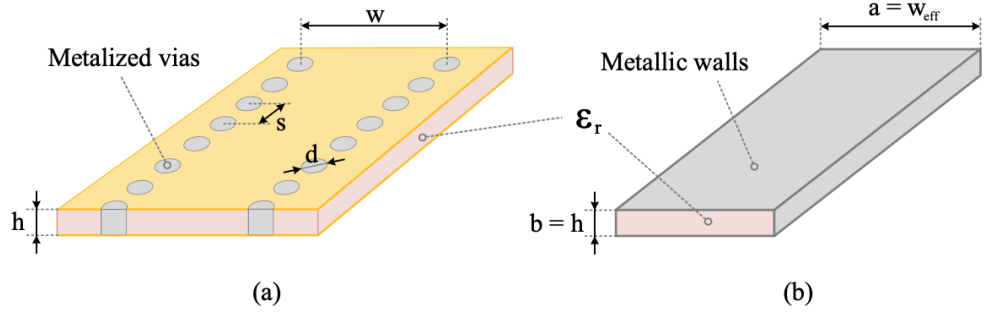


Figure 2.23: SIW antenna cross section showing metalized vias (a) and the equivalent dielectric waveguide (b) (courtesy of [2.67])

in planar form [2.67]. As seen in Fig. 2.23, the metallic dielectric waveguide has effective width  $a = w_{\text{eff}}$  and thickness  $b = h$ . The effective width of the dielectric substrate takes the following expression as determined in [2.68]:

$$w_{\text{eff}} = w - 1.08 \frac{d^2}{s} + 0.1 \frac{d^2}{w} \quad (2.11.1)$$

where  $w$  is the distance between the metallic vias,  $d$  is the diameter of the vias,  $s$  is the distance between two adjacent via centers. With this structure, only  $TE_{m0}$  mode exists and this is due to parallel flow of currents with respect to the vias. For other modes, the surface currents are cut by the vias which block propagation. The cut-off frequency for the  $TE_{m0}$  mode is given by [2.68]:

$$f_{m0} = \frac{m \cdot c}{2w_{\text{eff}} \sqrt{\epsilon_r}} \quad (2.11.2)$$

where  $c$  is the speed of light, and  $\epsilon_r$  is the dielectric constant of the substrate. Hence, the substrate dielectric height will not affect the cut-off frequency of the modes. The propagation constant for the fundamental mode has the following expression:

$$\beta_{\text{SIW}}(f) = \sqrt{\left(\frac{2\pi f \cdot \sqrt{\epsilon_r}}{c}\right)^2 - \left(\frac{\pi}{w_{\text{eff}}}\right)^2} \quad (2.11.3)$$

By making the two terms equal in Eq. 2.11.2 and 2.11.3, we are able to find exact dimensions of our structure which will satisfy the cut-off frequency condition and the operating frequency of the radar. A set of simulations have been carried out to find the best dimensions for our radar. More details can be found in [2.67]

and how to create similar structures based on specific cut-off frequencies.

## **2.12 Microstrip patch antennas versus SIW antennas**

There are other considerations why series fed arrays (using microstrip, similar to a patch antenna) have some issues when compared to SIW antennas. Because they act as leaky wave antennas [2.68], the beam can scan with variation in frequency. Hence, the antenna would deviate or squint from its position which will make this an undesirable effect. Hence, microstrip series fed arrays can present some issue which are not as much present in SIW antennas. Also, it is more difficult to design a broadband antenna using microstrip patch in comparison to SIW antennas. One microstrip patch antenna was designed and tested within our group as can be seen in Fig. 2.24. The beampattern of the patch antenna can be seen as very narrow in comparison to the SIW antenna depicted in Fig. 2.25. Although results are not shown here for brevity, but can be found in [2.67], where the patch antenna array can only reach 500 MHz by design, whereas the SIW antenna is able to show a bandwidth of at least 1.6 GHz. This helps improve the range resolution of the radar. Comparing Figs. 2.24 and 2.25 it can be seen that the SIW transmitting antenna is more broad in its beampattern, which is more desirable for a transmitter since targets which are at the edge of the field of view. Additional difference between microstrip patch antennas and SIW antennas can be found in [1.5].

## **2.13 State-of-the art limitations and Outlook**

This chapter has presented the background theory related to automotive radars used for collision avoidance applications and the state-of-the art radar systems present in literature. Radar systems have been analysed, and key performance parameters have then been described: range and angular resolution, design frequency, bandwidth, FOV, half-power beamwidth (-3dB point), side-lobe levels. From this investigation we can draw some conclusions about the current state-of-the-art radar system:

- On-chip glass resonator antennas require extended manufacturing capabilities,



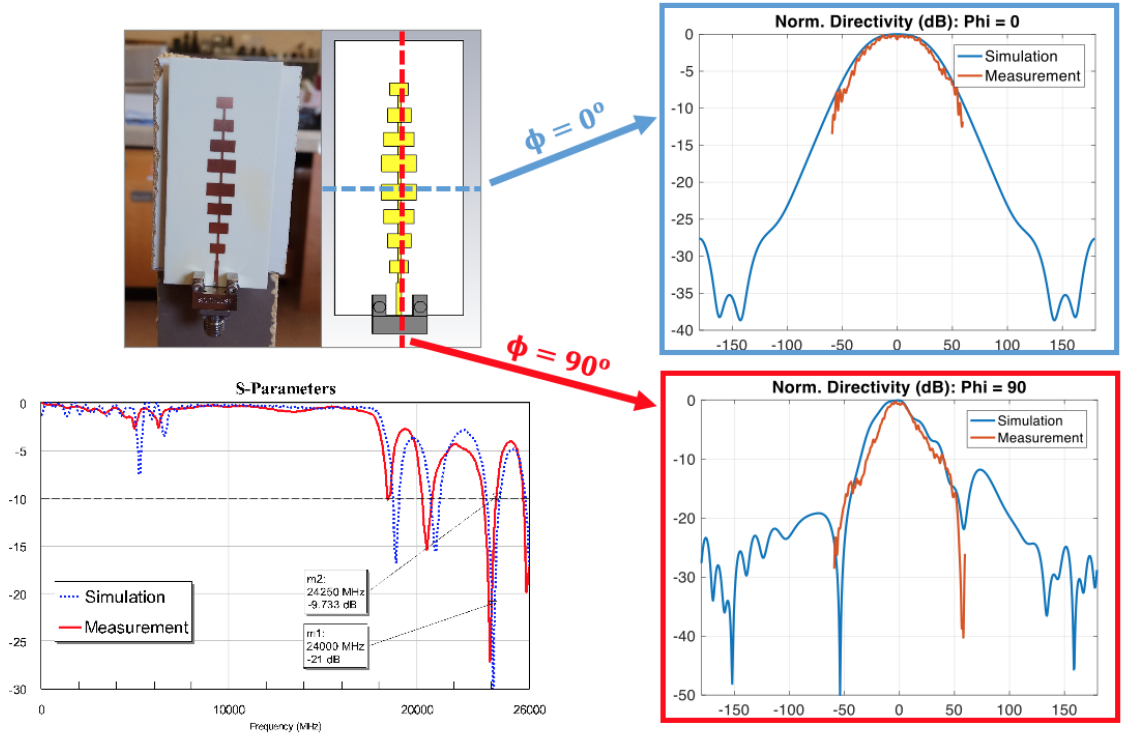


Figure 2.24: Microstrip patch antenna beampattern measurements in the azimuth and elevation plane. (courtesy of [2.67])

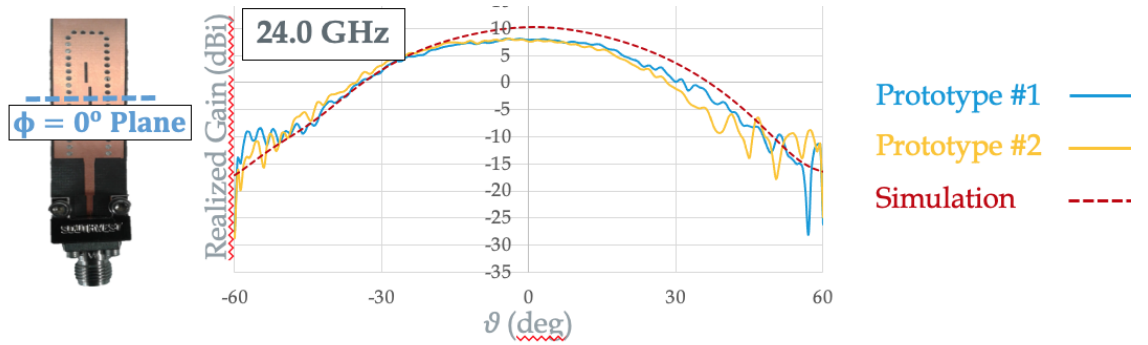


Figure 2.25: SIW antenna beampattern measurements in the azimuth plane. (courtesy of [2.67])

whereas SIW antennas can be easily fabricated due to the availability of the technology with current manufacturing processes. Quasi-optical antennas also have a limited FOV compared to other antenna systems.

- Radars are trending towards the digital domain. Many systems adapt a hybrid approach to benefit both from the capabilities of analogue and digital beamforming, with hardware reduction implying a further reduction in unit cost. Re-configurable hardware is a key advantage to digital radar systems.
- ULAs have less performance compared to a non-uniform array equivalent which

can increase angular resolution or reduce side-lobe levels.

- High resolution algorithms such as MUSIC have a longer processing time which is undesirable for certain automotive scenarios.

Due to these reasons, FMCW SIW radar systems are a good candidate as a system solution which can be integrated easily with current manufacturing processes, can transition to the digital domain by sampling the antenna receiver signals (as we will see in later chapters, with the use of ADCs), and is able to accommodate antennas with non-uniform spacing antenna arrays to offer an increased antenna aperture and resolution as we will see in later chapters.

## **2.14 Contributions by the candidate**

In this chapter, the presented work is a result of several pieces of several efforts exercised by the candidate. Specifically, the candidate has carried out the initial literature review and market survey for making a decision in acquiring the new radar system and developing the test rig. He has done the power measurements for the radar once it arrived. These were successful and the capabilities of the platform integrated in the anechoic chamber facilities at Heriot-Watt.

# Chapter 3

## FMCW SIW Radar Systems

### 3.1 Introduction

Due to the growing need for the automotive industry to obtain accurate localisation at radar proximity (up to 50m) [1.2, 3.1], many works address the topic of precise detection. In addition to this, it is important for industry to offer a cost effective solution which can be commercialised. In this chapter, radar system proof of concepts are presented which are based on the preliminary work carried out in [1.4] and further developed in [1.5].

#### 3.1.1 Motivation and goal

The aim of the work presented in this chapter is to show that combining multiple radar data using a network of sensors helps build an advanced system that is able to show better performance than an individual unit. The motivation behind this is building a system which is able to cover the entire field-of-view (FOV) of the radar with maximum resolution capability.

This chapter will present the following advancements:

- Sectorized radar systems for visualising the whole FOV of the radar.
- Sparse non-uniform antenna array design for side-lobe level mitigation and antenna aperture enlargement.
- SIW antenna arrays for enhanced transmission and reception with the reduction of radar losses at millimetre frequencies.
- Antennas with high bandwidths for high range resolution

Conventional patch array antennas provide a robust architecture and are easily fabricated at relatively low-cost, but often do not achieve high bandwidth performances when compared to SIW technology at millimetre frequencies [3.2, 3.3]. For example, SIW antennas can exhibit the same ratio of bandwidth and operational frequency.

Many works found in the literature approach the problem of radar resolution [2.23, 2.34, 2.45, 2.56, 2.58]. The discussions in this chapter will focus on both azimuth and range resolution while maximising the angular span, also termed as the field-of-view (FOV) and minimising side-lobe level for better target detection. These high performance radars are made innovative with techniques including but not limited to beamforming, antenna engineering, target detection algorithms, orthogonal transmission and clever RF front-end design.

The chapter is organised as follows: Section 3.2 will discuss concepts and state-of-the art automotive radars for increased angular resolution, Section 3.3 will present radar design, hardware and signal processing for the design of a sectorized automotive radar system, Section 3.4 will present simulations and experimental setup of the proof-of-concept sectorized radar system, Section 3.5 will discuss the advantages and disadvantages of using the sectorized radar system and Section 3.6 will present the findings of this thesis chapter.

## **3.2 Overview of Radar Concepts**

A single radar system with high angular resolution implies a large antenna front-end. Depending on the carrier frequency, car manufacturing requirements and space available on the vehicle, the designer has to restrict the size of the radar front-end to specific dimensions. A number of other radar solutions have been reported in literature for high angular resolution and are summarized in Table 5.1. The work presented in [2.23] used analog beamforming with 2 transmitter and 16 receiver elements (vertically polarised) defining the radar antenna front-end. While a range resolution of 2.5 cm was achieved with a 5.2% impedance matching bandwidth and minimal beam squinting (where the beam changes angle with change in frequency), the FOV only covers  $\pm 50^\circ$ . The half-power beamwidth ( $\Theta_{3dB}$ ) ranges between  $5.5^\circ$  to  $7^\circ$ . In

[3.4], a 120 GHz compact radar system was presented to show that it is possible to employ integrated circular antennas to achieve a high range resolution, whilst adopting a 5 GHz radar bandwidth. Furthermore, in [3.5], it was shown possible that different transmit-receive (TRX) architectural blocks can be configured and spaced appropriately to achieve better angular resolution when compared to more conventional MIMO strategies.

Recently, works have also been carried out in the low-terahertz frequency range. This is because research has shown that absorption losses between 100 GHz and 900 GHz does not exceed 3dB/km, hence detection ranges up to 200 m are achievable [3.9]. For example, high resolution images have been obtained with a  $1.2^\circ$  angular resolution (see [3.7, 3.8]) where increased frequencies allowed for larger bandwidths and thus improved range resolution. In addition, novel processing techniques such as Doppler beam shaping (DBS) have been adopted from aerospace engineering principles for advanced imaging techniques [3.7].

To advance these findings a novel radar system is presented in this chapter of the thesis. It consists of a sectorized radar system using SIW antennas arrays with non-uniform element spacing. This is a development which resulted from the work published in [1.4]. This antenna selection and distinctive features along with the radar electronics which offer high bandwidth in the 24 GHz band, provides significant benefits as compared to other radars in terms of FOV, the angular resolution (i.e.  $\Theta_{3dB}$ ), and detection time. More specifically, the novelty of this approach consists of designing a sparse antenna system, using virtual antenna apertures with MIMO technology to enhance angular resolution and boost target detection. The 24 GHz multi-radar system prototype uses three different sectors (also defined herein as a sectorized radar) as illustrated in Figure 3.1 for automotive applications. A comparison with the works found in the literature review and the work presented in this chapter can be found in Table 3.1

### 3.3 Sectorized Radar System Design

The system is capable of refined angular resolution due to the developed two-tier detection procedure by considering sparse arrays to achieve better angular resolu-

Table 3.1  
Comparison of Other Radar Systems as Reported in the Literature

Automotive Radar	Carrier Frequency	Target Estimation Algorithm	Antenna Type	Equivalent Uniform Linear Array	Element Spacing	Receiver Percentage Bandwidth (GHz)	Measured Field-of-View	Range Resolution	$\Theta_{3dB}$
[2.23]	77-81 GHz	Analog Beamforming	Microstrip Arrays	16	$0.6\lambda$ (system)	5.2% (4 GHz)	3.75 cm	$\pm 50^\circ$	$4.0^\circ$
[3.4]	120 GHz	MIMO Digital Beamforming	Circular Patch Antennas	16 (= $4 \times 4$ )	Non-uniform (distributed)	4.1% (5 GHz)	3 cm	$30^\circ$	$8.5^\circ$
[3.5]	61 GHz	Digital Beamforming	Scalable TRX MIMO radar	4 (= $2 \times 2$ )	$2\lambda$ (system)	14.7% (9 GHz)	1.7 cm	$\pm 15^\circ$	$6^\circ$
[2.56]	75-77 GHz	MIMO Digital Beamforming	Differential Microstrip Arrays	16 (= 4 TRX modules)	Non-uniform (distributed)	2.6% (2 GHz)	7.5 cm	$\pm 81^\circ$	$3.7 - 6.8^\circ$
[3.6]	78-80 GHz	MIMO Digital Beamforming	Planar SIW Antenna Arrays	8 (= $2 \times 4$ )	$1.75\lambda$ (system)	2.4% (2 GHz)	7.5 cm	$\pm 30^\circ$	$7^\circ$
[3.7], [3.8]	79 GHz / 150 GHz / 300 GHz	DBS / SAR	Horn Antennas	2 RX	One system	6.3% / 3.33% / 1.67% (5 GHz)	3 cm	$\pm 40^\circ$	$1.2^\circ$ at $v = 0.25$ m/s
<b>This work</b>	24 GHz	MIMO Digital Beamforming with Sectorization	Planar SIW Antenna Arrays	32 (= 4 $\times 2 \times 4$ )	Non-uniform (distributed)	6.25% / 1.5 GHz	10 cm	$\pm 90^\circ$	$4.4^\circ$ (Tier 1) <b>2.2°</b> (Tier 2)

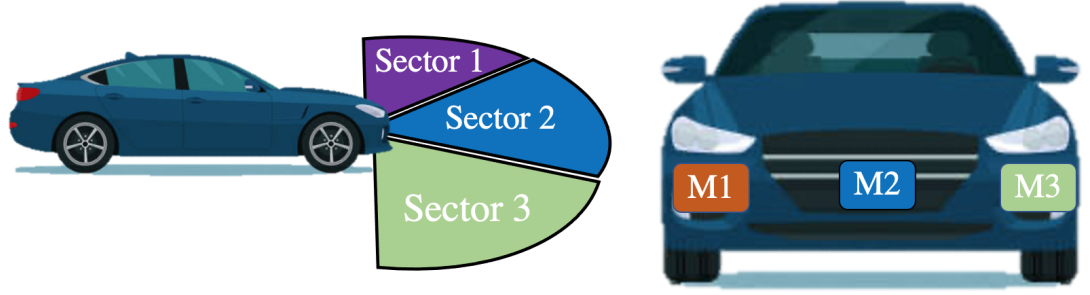


Figure 3.1: Modular sectorized radar concept using three modular MIMO radars across the front bumper of an automobile.

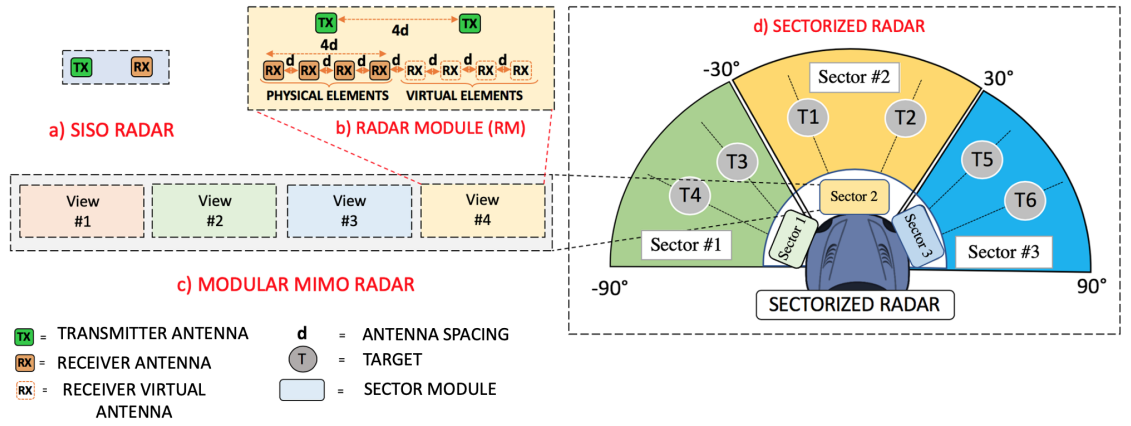


Figure 3.2: Proposed automotive radar and antenna configuration: (a) SISO, (b) a MIMO radar module (RM) defined by 2 physical transmitters (TX) and four receivers (RX), (c) modular MIMO radar defined by 32 antenna elements in total ( $= 4 \text{ RM} \times 2 \text{ TX} \times 4 \text{ RX}$ ), (d) sectorized MIMO radar system where 6 targets are illustrated.

tion, and multiple radar modules (RMs) for a larger effective FOV. Also, the use of the designed SIW antennas offers a broad impedance matching bandwidth to achieve high range resolution. Using this radar system configuration allows for several sectors to be illuminated to obtain a complete  $\pm 90^\circ$  image while achieving an angular resolution of  $2.2^\circ$  and a range resolution of 10 cm for the entire FOV, with a maximum detectable range of 50m.

In order to assess the benefit of using several modules together, the radar configurations have been simulated in MATLAB. The trialled radars and their configurations are illustrated in Figure 3.2 and are classified as follows:

- SISO Radar (Figure 3.2(a)): This refers to the single transmit single receive

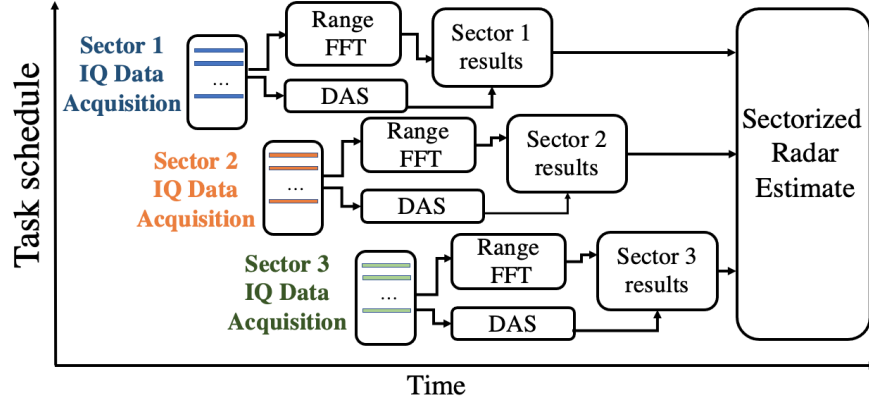


Figure 3.3: Workflow diagram for the signal processing of the sectorized radar for one acquisition cycle, showing in-quadrature (IQ) data, delay and sum (DAS) beamforming and Fast Fourier Transforms (FFT).

radar configuration.

- Radar Module (Figure 3.2(b)): This configuration is defined by two transmitters and four receivers defining an elementary MIMO radar module (RM).
- Modular MIMO Radar (Figure 3.2(c)) This radar configuration uses a combination of four MIMO sub-modules; i.e. four distinct RMs where each RM is defined by two transmitters and four receivers. This defines the modular MIMO radar system to have 32 ( $= 4 \times 2 \times 4$ ) virtual receiver antenna elements.
- Sectorized MIMO Radar Front-end (Figure 3.2(d)): The final configuration is composed of three modular MIMO radars which are assigned in three sectors to cover the range from  $-90^\circ$  to  $+90^\circ$ . Each sector is operating independently to other sectors, to reduce interference between radars. An overview of signal processing schedule for the radar can be seen in Figure 3.3.

The 24 GHz frequency band was chosen because the radar hardware as well as the supporting MMICs are commercially available. This offers simple integration, low-cost implementation for research and development, and proof-of-concept demonstration for our proposed radar system architecture. The frequency band range for automotive radars has been used in this work for making a proof-of-concept demonstrator. A scaled-down version of the radar system, for operation at 77 GHz for example, is possible and defines future work. The usage of the 24 GHz ISM bands



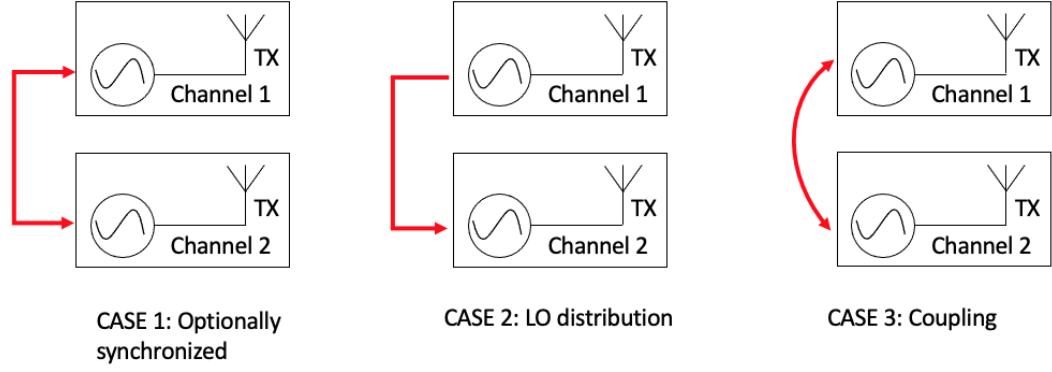


Figure 3.4: Comparison of radar synchronisation designs based on FMCW radar architectures ranging from non-coherent networks (left) to synchronized systems (right) [1.1]

are explained in [2.66] and [3.10]. However, the motivation of the present thesis is development and study of the proposed MIMO radar system using sub-modules whilst employing sparse antenna arrays for enhanced angular resolution. At the same time, the range resolution is also proven in advance of a scaled-down 77 GHz version of the radar.

There are several challenges at 77 GHz as mentioned in [3.11] and [3.12]. Firstly, 77 GHz are smaller in size and packaging is very important at these frequencies since they significantly contribute to the transition losses of the radar. This is a performance penalty for manufacturing with set tolerances. Some of these on-chip losses are described in [3.12] with several antenna-on-chip technologies. Another disadvantage for working at 77 GHz is the increased cost for antenna design and manufacturing. The size of an antenna design a 77 GHz is three times smaller than one at 24 GHz due to the wavelength and so it is more expensive to design and fabricate antennas at a smaller dimension, requiring more specialised equipment.

### Sectorized radar: synchronised vs. non-synchronised

In vehicles today, we see how several sensors are employed, and in this process, the functions of each radar needs to be combined defining a network of sensors. Radar networks show improved performance due to the diversity obtained by the much larger aperture created and the possibility of ego-motion estimation [3.13]. Results shown in [1.1] show that networks of radars, either coherent or not, are able

to improve the performance of radars. These types of radars have adopted a few terminologies such as netted radars, radar networks or multi-static radar. These concepts are often subdivided into sensor nodes, monostatic and bi-static radars.

A coherent network is one where synchronization is possible when the clock signal of the transmitter or the LO is distributed around the network for all sensor nodes, such that they have a common time and phase reference relative to a single node. Fig. 3.4 shows the different types of coherent radar. It is often difficult to implement a coherent radar in a practical system. Most time a common oscillator for the transmit and receive path for a monostatic radar is easily achievable. However, coherency for a radar network implies a common local oscillator for all of the network. In a passive radar, coherency is assured for the local node, however, if the TRX pairs are not all synchronized, they will not be all coherent. Partially coherent distributed radar is better than the monostatic case, but less performant in comparison to a fully coherent network.

The degree of coherence in a distributed radar system can be classified into two: the degree of coherence across the system and the level at which the coherency is combined on the system. Netted radars can be coherent in time, or space or locally coherent. In a coherent system, the RF frequency and phase are known locally and globally with good stability of the clock [3.14].

The question if a radar is coherent or not relates to several aspects. Coherence may be present in space, time, frequency and phase [3.15]. For automotive radar, typical coherence relates to phase synchronisation between different sensors in a network. In case there is no synchronisation or coherency between nodes they act as a single radar nodes which often do not record angular information about the target. However, these sensor nodes can collectively determine angular information through multilateration [3.16, 3.17]. This method suffers from target ambiguities, more specifically in scenarios with multiple targets. Another method of obtaining angles is through velocity evaluation [3.18].

Incoherent networks with synchronization (where space, time and frequency are coherent but not phase), provide angular diversity, however, they lack coherent processing gain [3.19, 3.20]. In [3.19], a bistatic incoherent network is presented where the phase differences between the sensor nodes are compensated in post-

signal processing. Methods for achieving phase coherence have been found and offer both a broad aperture and coherent processing gain. Coherence has been reported with transmission lines or optical fibres as a simple way of coherent coupling [3.13, 3.21]. Since coherence realized with hardware integration is more difficult to achieve, research is directed towards compensating coherence with signal processing means or system concepts [1.1]. Some signal processing techniques for coherent radar compensation can be found in [3.22] and [3.23]. A general FMCW architecture which describes  $N$  nodes is presented in: [3.23] and [3.24] in coherent form, while [3.25] uses repeaters for the same. Interferometric methods have been proposed in [3.26]. While most sparse apertures have a larger aperture, false targets are likely to appear due to the the side lobes. This can be avoided by using compressive sensing methods as presented in [3.25].

### **Sectorized radar design considerations**

We define our radar antenna system design as a multi-static radar system (design also used in Chapter 5.4) because we obtain a 32% improvement in angular resolution since the total array aperture size has the length of 47 elements spaced at half-wavelength, compared to 32 elements at half-lambda. Our approach can also reduce costs due to the scalability and repetition of the required sub-module hardware and radar antennas. This makes the system maintenance and repair simpler in that individual RMs can be replaced or fixed, rather than the entire radar system itself. This modular design strategy also fosters low-cost mass production of the RMs rather than the assembly and manufacturing of an equivalent radar system. Also, by considering pipelined signal processing for the individual RMs (as seen in Figure 3.3), interconnect lines are kept at a minimum electrical length, reducing losses and noise susceptibility. This would not be possible for an equivalent and more standard (or larger scale) radar architecture. In addition, the MMICs connected to the antenna front-ends can be physically separated (in practice discretely encapsulated for example) to reduce electromagnetic coupling between radar electronics.

## Grating lobe reduction: avoidance of false targets

The problem of grating lobes and possible false targets are also mitigated in our radar system by the implementation of a non-uniform MIMO radar receiver made possible by sparse array theory [3.27, 3.28, 3.29]. We define a MIMO array as array formed of transmitters and receivers which cooperatively combine several illuminations of the target for a larger aperture (or virtual array). Moreover, to study this for the developed radar system, a static  $\lambda/2$ -spaced receiver was designed for the RMs using substrate integrated waveguide (SIW) technology. Then, the required channels connected to the antenna elements were appropriately selected. In particular, during the radar signal processing of the simulated and measured system, the antenna elements (and the corresponding RF channels) that contribute to the grating lobes can be suppressed and mitigated. It is shown in the chapter thesis that the overall radar system performance can benefit from this MIMO sparse array approach whilst preserving a large antenna aperture for the equivalent virtual receiver array. Comparisons are also made in this chapter for the radar system response when considering more conventional  $\lambda/2$ -spaced and  $\lambda$ -spaced radar receivers.

## 3.4 Radar Antenna Design

Microstrip antenna arrays have seen a widespread use for automotive radar systems since this type of antenna is simple to design and is easy to manufacture [3.30]. On the other hand, the radiation losses of SIW antennas are significantly reduced for millimetre-wave frequencies when compared with microstrip patch antennas as described in [3.2] and [3.3]. Also, SIW-type antenna arrays generally are less dispersive when compared to series-fed microstrip structures and other patch-type arrays [3.31], leading to reduced beam-squint over frequency which is generally desired for improved radar accuracy. A detailed review of other automotive antenna types can also be found in [3.32] and a complete review of SIW technology can be found in [3.31].

Following these previous efforts, SIW antennas have been selected for the radars presented in this thesis (see Figure 3.5). This is because when considering more conventional microstrip patch antennas, the beam can become squinted depending

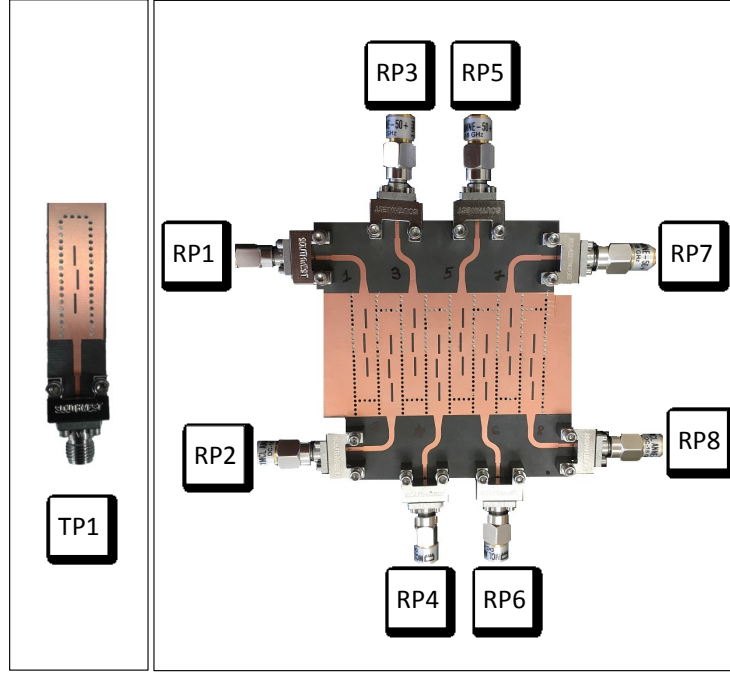


Figure 3.5: Single element SIW TX (left) and 8-element RX (right). The TX and RX SIW antenna ports, are labeled as  $TP_i$  and  $RP_i$ , respectively. The design has been carried out by Thomas Stoeber, another PhD student working in the automotive radar group.

on the transmission frequency; i.e. the undesired effect that the main beam position can change with frequency. This is due to the fixed distance of the radiating elements with respect to the wavelength [3.33]. More specifically, since the transmission frequency is constantly being changed in an FMCW radar, the beam angle can vary due to this dispersion, when employing more standard microstrip-based antenna arrays. A property which is undesirable in radar detection [1.4].

SIW structures on the other hand support fundamental and dominant  $TE_{01}$ -like mode excitation. This mode is generally known to have lower dispersion when compared to the quasi-TEM mode of microstrip [3.34, 3.31]. SIW slot-based antennas can also offer reduced (unwanted) beam squint over frequency and can also exhibit reduced electromagnetic coupling because of reduced surface wave losses [3.31]. This effect happens due to the change in frequency can also the phase of individual antenna elements, and hence the beam changes angle with the deviation of phase over the frequency change [3.35].

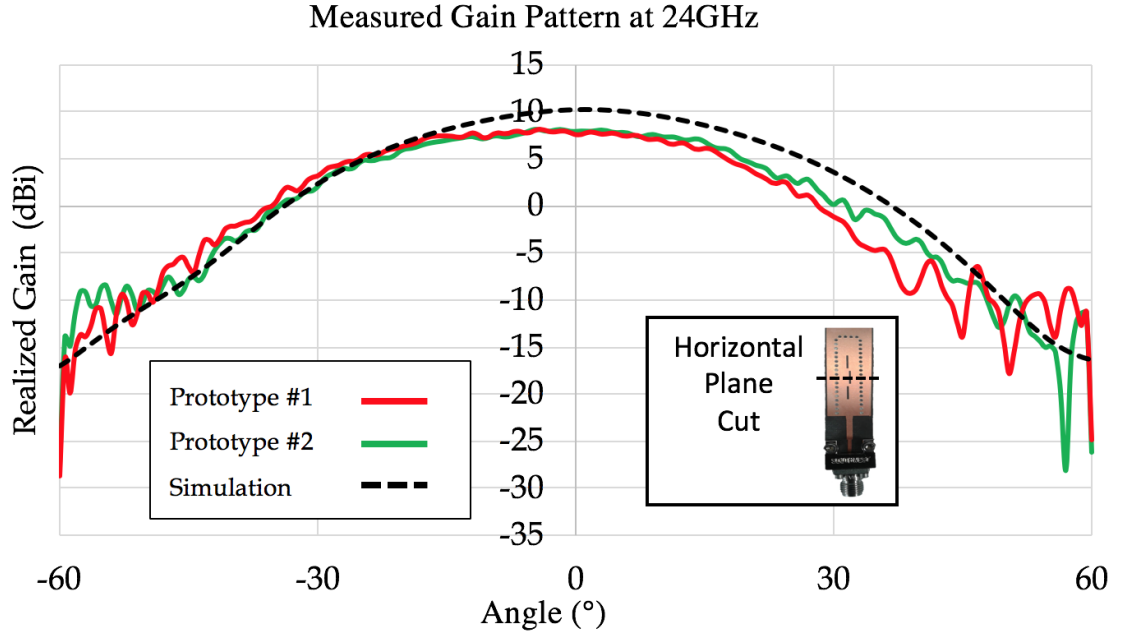


Figure 3.6: Realised gain beam pattern of the SIW transmitter antenna in the horizontal plane.

### 3.4.1 Transmit Substrate Integrated Waveguide (SIW) Antennas

SIW antennas generally have decreasing impedance bandwidth with a higher number of radiating slots [3.36]. However, the investigated structure employs three slots which not only increase the gain and bandwidth of the antenna but generates a fan-like far field beampattern in the horizontal plane. This is important such that a large angular range is illuminated by the transmitter. For example, the field of view is about 60 degrees (as seen in Figure 3.6).

The three radiating slots determine the transmit antenna fan-like beam in the horizontal plane and the resulting beam pattern can be seen in Figure 3.5 (left). It should be mentioned that results for two transmitter prototypes are reported, and as can be observed, similar results are shown with general agreement with the full-wave simulations. This beampattern characteristic allows the radar to have a wide coverage of the FOV in the transmit path, assuring electromagnetic scattering returns back from the targets at the required angles.

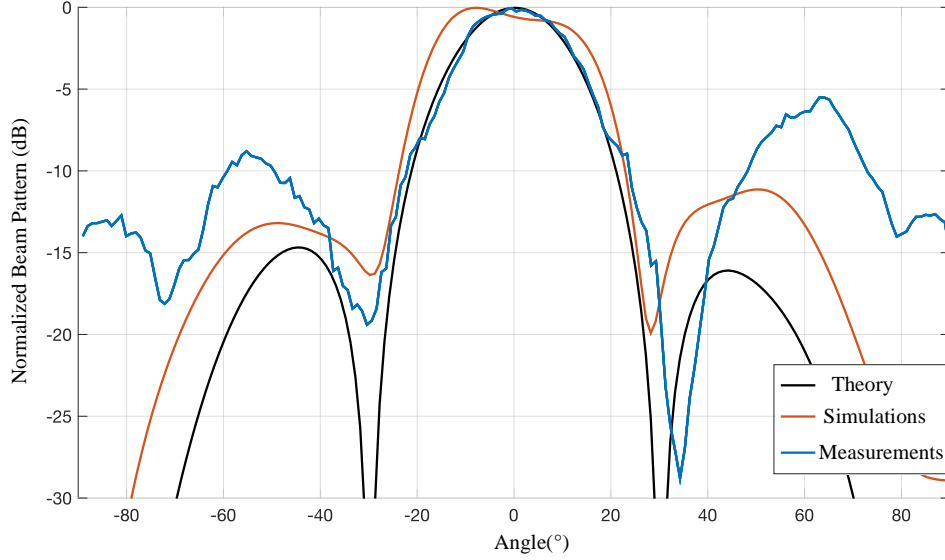


Figure 3.7: Comparison of theoretical array factor, simulations and measurements for the  $\lambda/2$  array with 4 RX elements using RP3, RP4, RP5, and RP6 (see Figure 3.5).

### 3.4.2 Receive Substrate Integrated Waveguide (SIW) Antenna Arrays and Dual-Mode Detection

In the receiver configuration, the designed SIW structure uses an array of longitudinal slots (as seen in Figure 3.5 (right)). As with the transmit antennas, the design parameters have been selected according to the guidelines presented in [3.37, 3.38] and optimised using CST Microwave Studio. The beam pattern measurements of both the transmit and the receive antennas were completed in a calibrated anechoic chamber using a near-field system (NSI) positioner which computed the far-field response of the antennas. Good agreement between CST simulations and the measurements can be observed for the horizontal patterns of the four-element array at  $\lambda/2$  inter-element spacing (see Figure 3.7).

The half-power beamwidth of the  $\lambda$ -spaced receiver is reduced by approximately a factor of two when compared to the  $\lambda/2$  spaced receiver due to the enlarged aperture, but it introduces grating lobes. The investigation of these two configurations can allow for the same target scenario to be viewed by the radar system to obtain useful data from both resolution perspectives. Consequently, this makes it advantageous to interrogate data from both radar receiver configurations because each set has

acquired complementary data for each radar measurement. Therefore, combining data with such a two-fold detection system (see Figure 3.10)) can offer improved angular resolution for the radar should that be desired. Since the radar presented in this thesis uses an antenna array which can detect at both  $\lambda/2$  and  $\lambda$  spacing (respectively RP3, RP4, RP5, and RP6, and, RP1  $\dots$  RP8, defining Tier 1, see Figure 3.10), a two-tier approach has been used to investigate further the possibility of improved angular resolution.

### 3.4.3 Two-tier process for non-uniform antenna design

The motivation for employing a two-tier process for the non-uniform antenna receiver realisation is the use of the  $\lambda$ -spaced antenna receiver elements, which allows for a much greater antenna aperture compared to the  $0.5\lambda$ -spaced antenna receiver array. This process is done with two sets of measurements. One where the 8-element antenna receiver is spaced at  $0.5\lambda$  and another at  $\lambda$  spacing for the same antenna receiver. If the measurements are done for the same scenario at different times, we are able to combine those results in order to achieve the best angular resolution and side-lobe-level reduction.

The employed method for obtaining the non-uniform antenna array (Tier 2) is to search through the antenna beampattern responses which result in an improved  $\Theta_{3dB}$  and SLL by combining both  $\lambda/2$  elements and  $\lambda$  elements. By removing unnecessary elements that contribute to the grating lobes and increased SLL, an improved array pattern was obtained and the beampatterns will be presented later in the chapter. However, this exhaustive search implies evaluating the patterns of over 10,000 antenna array configurations. Thankfully, an automated methodology in MATLAB was developed to identify the best antenna array combination of  $\lambda/2$  data and  $\lambda$  data, where the algorithm would choose only solutions which have improved  $\Theta_{3dB}$  and SLL compared to the previous solution. This process is illustrated in Figure 3.10, which also shows the best antenna configuration for our antenna array design.

### 3.4.4 Selecting the best antenna configuration

There are three stages before we can device on the optimal configuration of the antenna receiver:



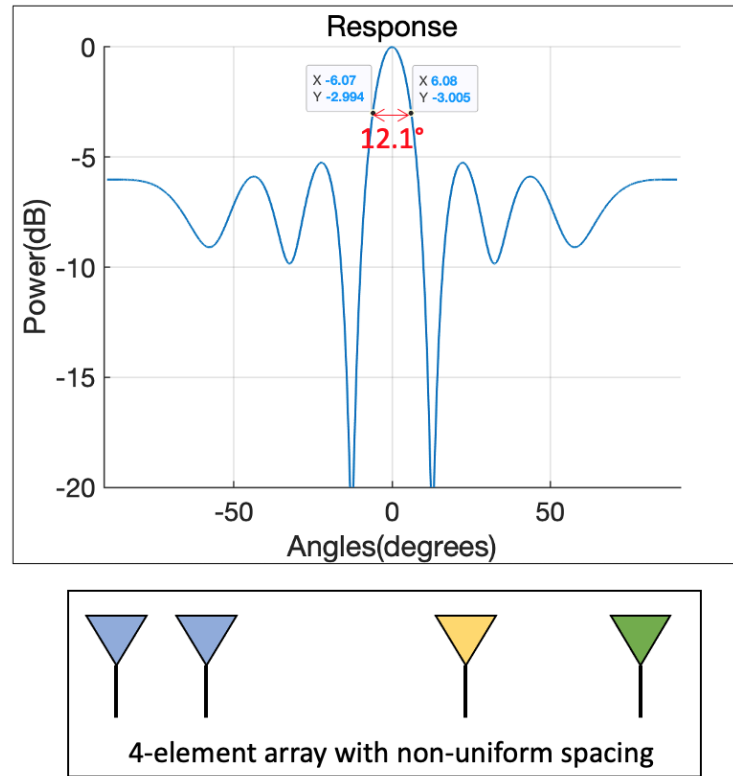


Figure 3.8: Best antenna configuration for four element receiver array with  $0.5\lambda$ -spacing between potential element positions.

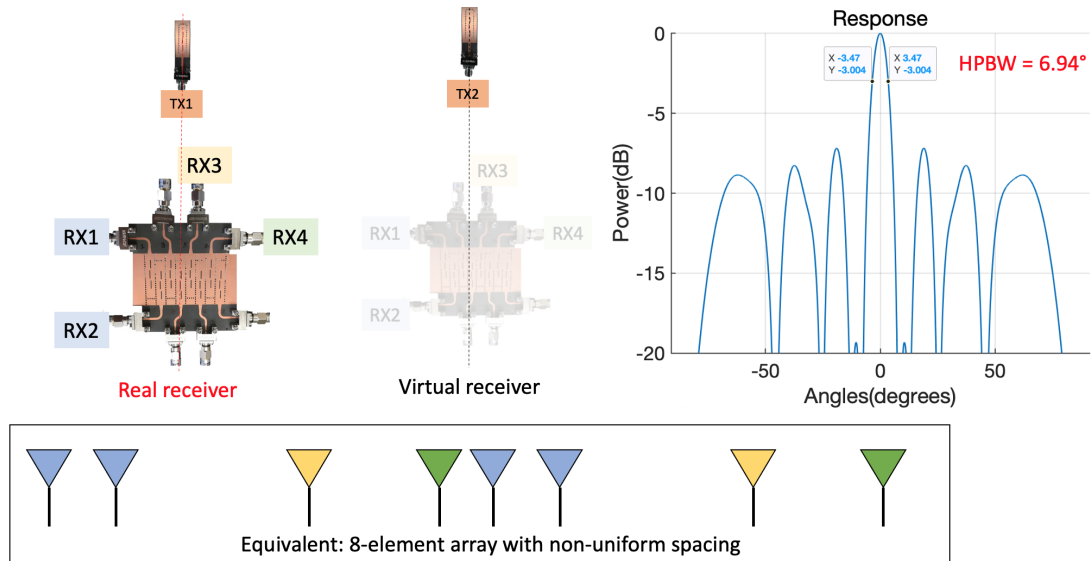


Figure 3.9: Best antenna configuration for eight element receiver array with  $0.5\lambda$ -spacing between potential element positions.

1. Find the best configuration for 4 elements (by choosing the best array factor).
2. Find the best configuration for 8 elements.

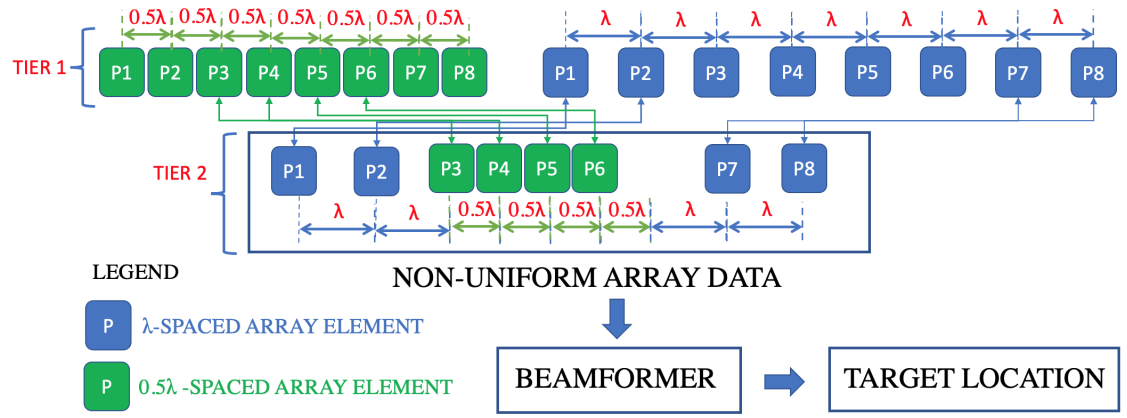


Figure 3.10: Two-tier process for determining the sparse, non-uniform antenna receiver from MIMO data for  $\lambda/2$  and  $\lambda$ -spacing.

### 3. Find the best antenna configuration for the SIW antenna receiver

For the first item (as seen in Fig. 3.8) we can easily discover which antenna array is most suited since there are limited number of possibilities. Using the array factor for several configurations we can easily find which offers best angular resolution and SLL. Then for the second array we can expand our search which will take more time for eight elements (as seen in Fig. 3.9.) Finally, we are ready for the 8-element and 32-element arrays by investigating .

Fig 3.11 depicts the 8-element receiver antenna connecting ports. A similar procedure was adopted for the modular MIMO radar (see Figure 3.2(c)) realising the effective 32-element receiver. This receiver configuration has a virtual aperture length of  $23.5\lambda$ , which is equivalent to an array of 47 antenna elements with a spacing of  $\lambda/2$ . Therefore, a 32% element reduction is achieved by employing just 32 elements for an aperture size of 47 antenna array elements. Further discussions on the measurements will be described in the next section considering the different spaced arrays.

The employed antenna array using the SIW approach exhibits less radiation on the edges of the element beampattern compared to a similar omnidirectional beampattern. Therefore, the total antenna receiver array response for the RM will also exhibit lower dissipated energy on the antenna edges. The expected array factors are computed in Figs. 3.12 and 3.13 for 8-elements and 32-elements respectively. These can be compared to the measured beampattern antenna response found in

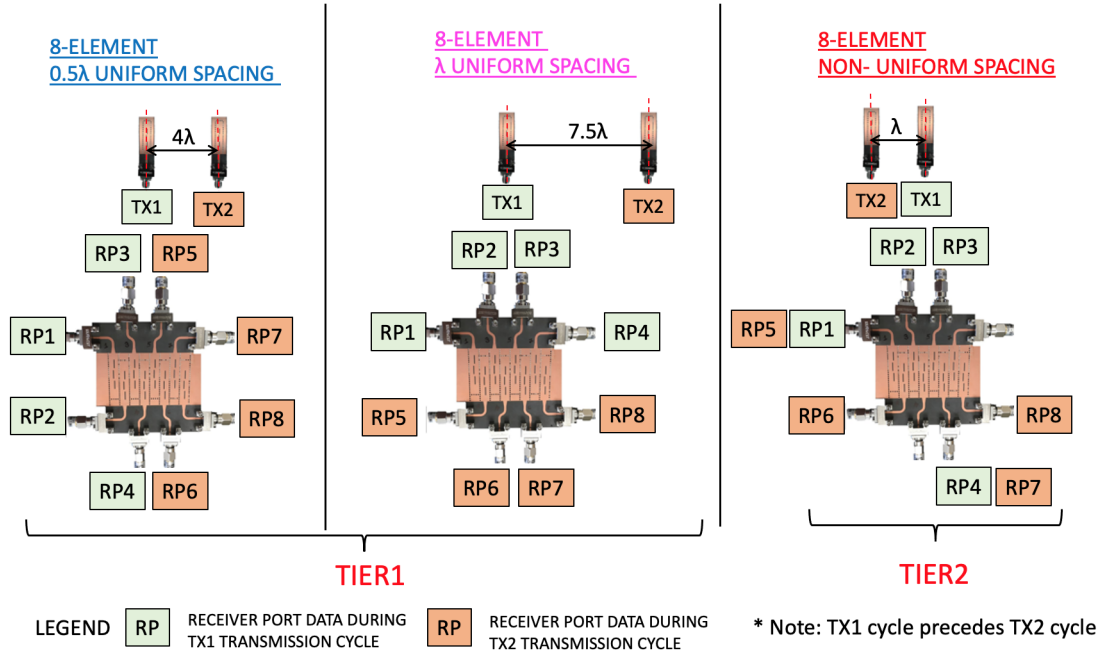


Figure 3.11: Radar receiver configurations for 8-element  $\lambda/2$ ,  $\lambda$ -spaced and non-uniform MIMO array receiver using SIW receiver antennas.

Figs. 3.14 and 3.15. The grating lobes for the  $\lambda$ -spaced receiver do not appear as high grating lobes as expected in the array factor due to the absence of radiation of the edges for the antenna element as described earlier. There are a few possible solutions to improve this. One solution as mentioned in [3.39], is to apply a spectral smoothing. This technique has also shown an improvement of 13 dB of SLL as mentioned in [1.7]. Other possible solution for this are the use of tapering functions such as Chebyshev, Hanning or Taylor window functions. These have a good success rate, however, they tend to alter the angular resolution of the radar.

### 3.4.5 Radar system specifications

The preliminary MIMO radar developed by the authors in [1.4] used two transmitting antennas (2TX) and four receiver antenna elements (4RX). This initially developed MIMO radar configuration is now used as a building block in the following for developing the proposed two mode radar system with FOV sectorization. Also, the antenna transceivers work in a time domain sequence; i.e. TDMA, in order to avoid signal interference while maintaining orthogonality. The process of acquiring a sectorized radar estimate is shown in Figure 3.3. A photo of the radar

system hardware and the radar block diagram can be seen in Figures 3.16 and 3.17, respectively. Also, the circuit-system architecture for an individual MIMO RM is outlined in Figure 3.18.

The radar system uses monolithic microwave integrated circuit (MMIC) components from Analog Devices and Hittite. Signals are generated at the transmitter (model: ADF5901) by using a calibrated voltage controlled oscillator (VCO) preceded by a varying ramp signal generated by a phased lock loop (PLL) (model: ADF4159). This allows for the signal to operate in FMCW transmission. Also, the signal obtained at the output of the VCO is then up-converted to 24 GHz. The ADF5901 has an internal amplifier to reach an output power up to +8 dBm. In addition, the transmitter antennas are used alternatively since the ADF5901 has an RF switch that can alternate the use of the transmitters by using a Hittite

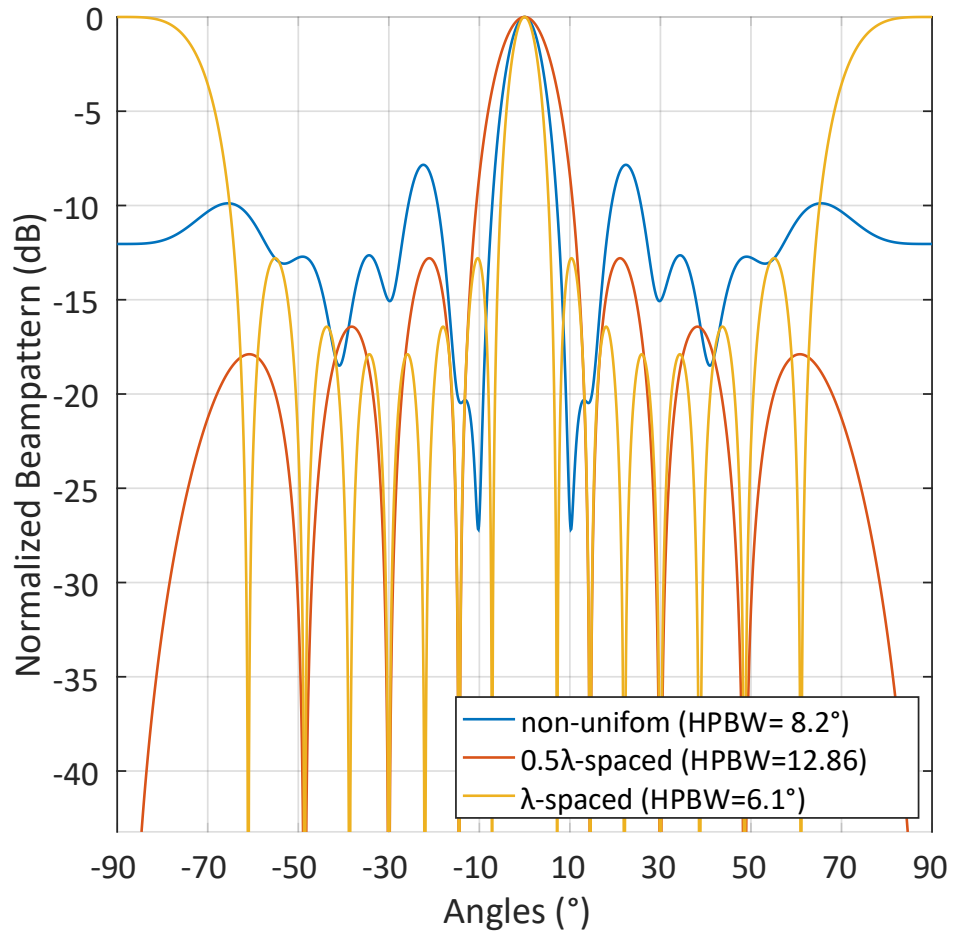


Figure 3.12: Array factor for beampattern array of RM with 8 elements at  $\lambda/2$  uniform spacing,  $\lambda$  uniform spacing, and sparse non-uniform spacing.

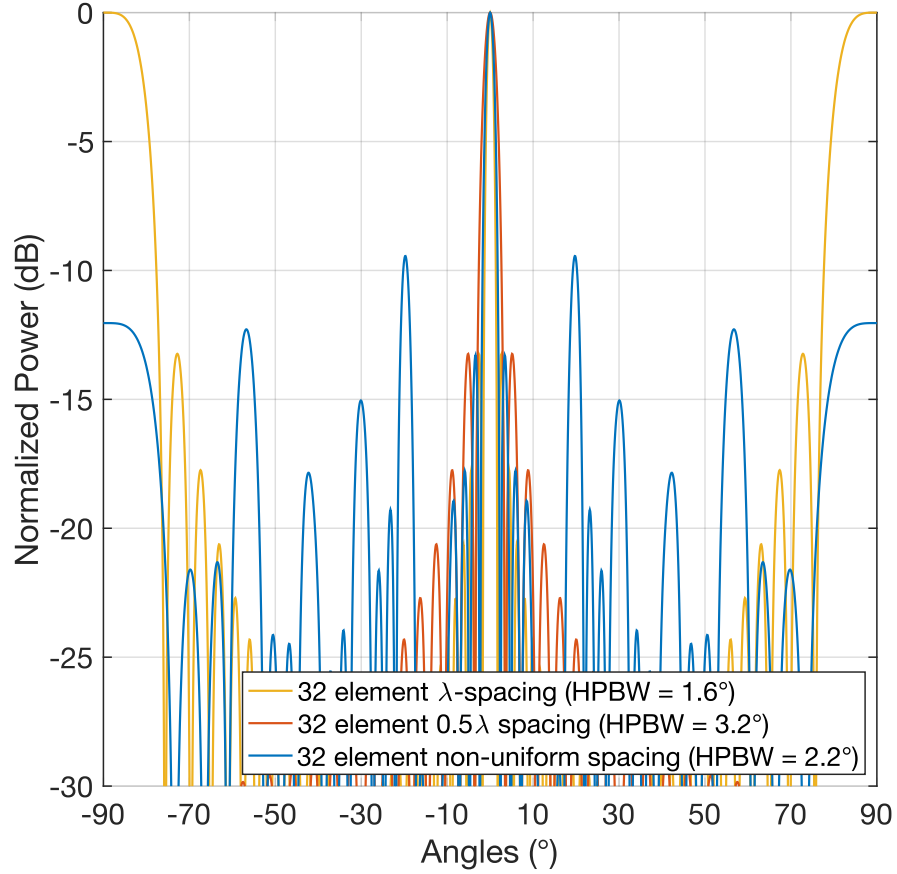


Figure 3.13: Array factor for beampattern array of RM with 32 elements at  $\lambda/2$  uniform spacing,  $\lambda$  uniform spacing, and sparse non-uniform spacing.

HMC1084LC4 switch (one for each RF channel).

The receiver is also connected to a 24 GHz VCO which is part of the down-converter. Including a low noise amplifier (LNA) (Hittite HMC751LC4) in cascade at the receiver input also lowers the noise level according to Friis's formula [3.40]. After the signal is down-converted, it passes through a band-pass filter in order to remove unwanted higher order modulation products generated by the mixer. The signal is then sampled by an analog-to-digital converter (ADC) and passed to the digital beamforming network. Differential lines are used to improve the common mode rejection ratio of the amplifier and reduce noise. A summary of the radar hardware is presented in Table 3.2.

Increasing the physical and virtual aperture size of the receiver front-end improves the angular resolution for the MIMO radar system. Consequently, it is con-

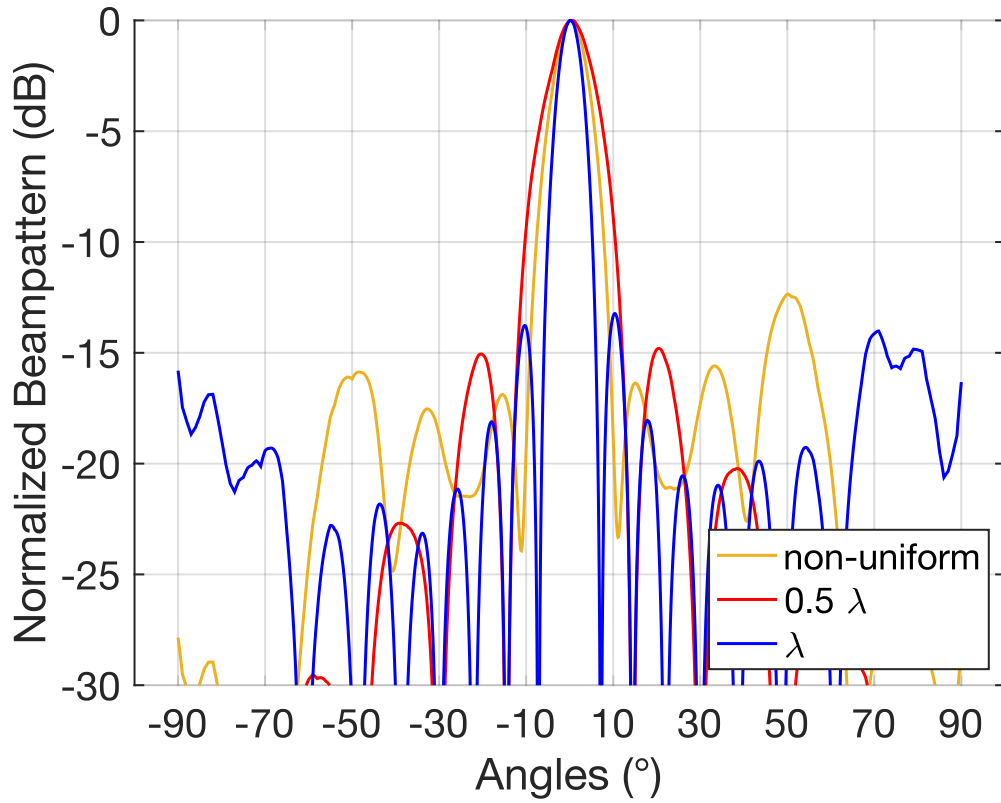


Figure 3.14: Comparison of measured 8 element modular MIMO radar at  $\lambda/2$  uniform spacing,  $\lambda$  uniform spacing, and non-uniform sparse array using element beampattern and array factor.

Table 3.2  
Circuit Components for the Radar

Circuit Component	Supplier	Part Number
Phased Lock Loop	Analog Devices	ADF4159
Transmitter MMIC (2TX)	Analog Devices	ADF5901
Receiver MMIC (4RX)	Analog Devices	ADF5904
Low Noise Amplifier	Hittite	HMC751LC4
MESFET Switch	Hittite	HMC1084LC4

ceivable that multiple MIMO RMs could be appropriately placed to collect data, and therefore, be able to achieve better system performance in terms of resolution

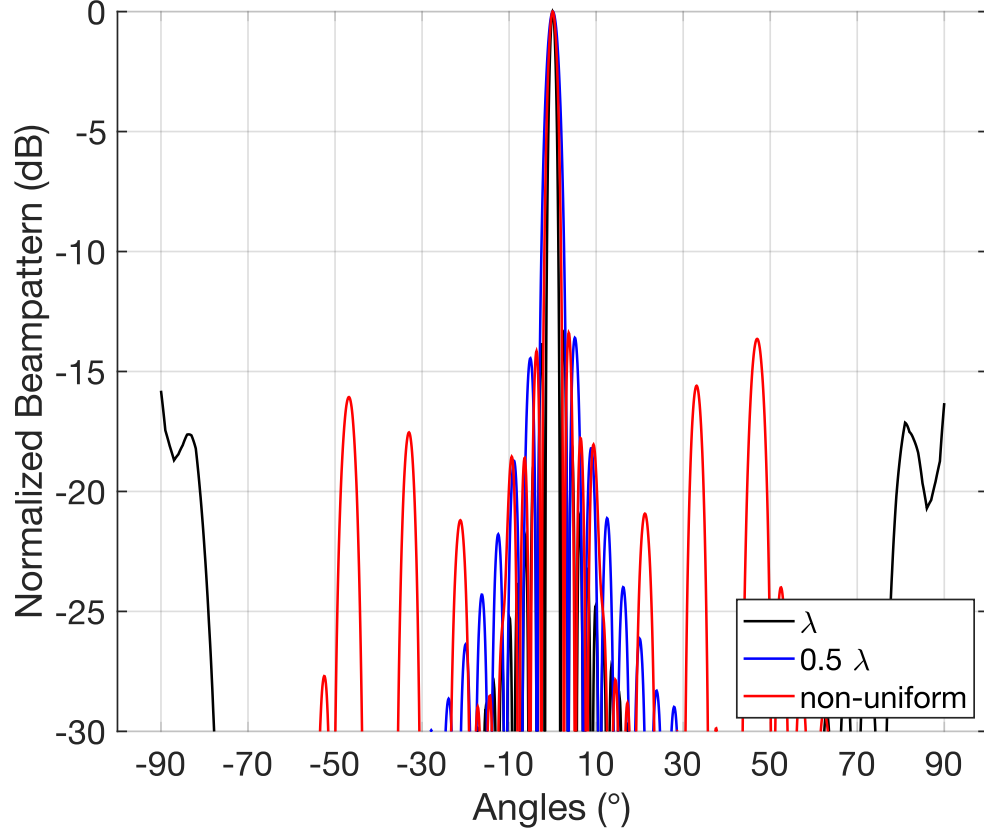


Figure 3.15: Comparison of measured 32 element modular MIMO radar at  $\lambda/2$  uniform spacing,  $\lambda$  uniform spacing, and non-uniform sparse array using element beam-pattern and array factor.

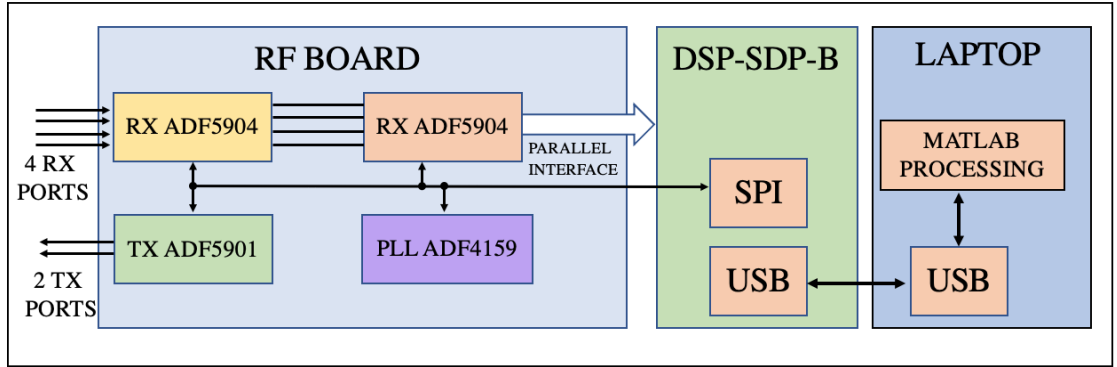


Figure 3.16: Radar connection and signal processing diagram for a single RM.

and target detection when compared to an individual MIMO RM. This design motivation follows the MIMO radar work in [3.41] which also employs highly separated antennas. However, it is important at this stage to validate that the individual

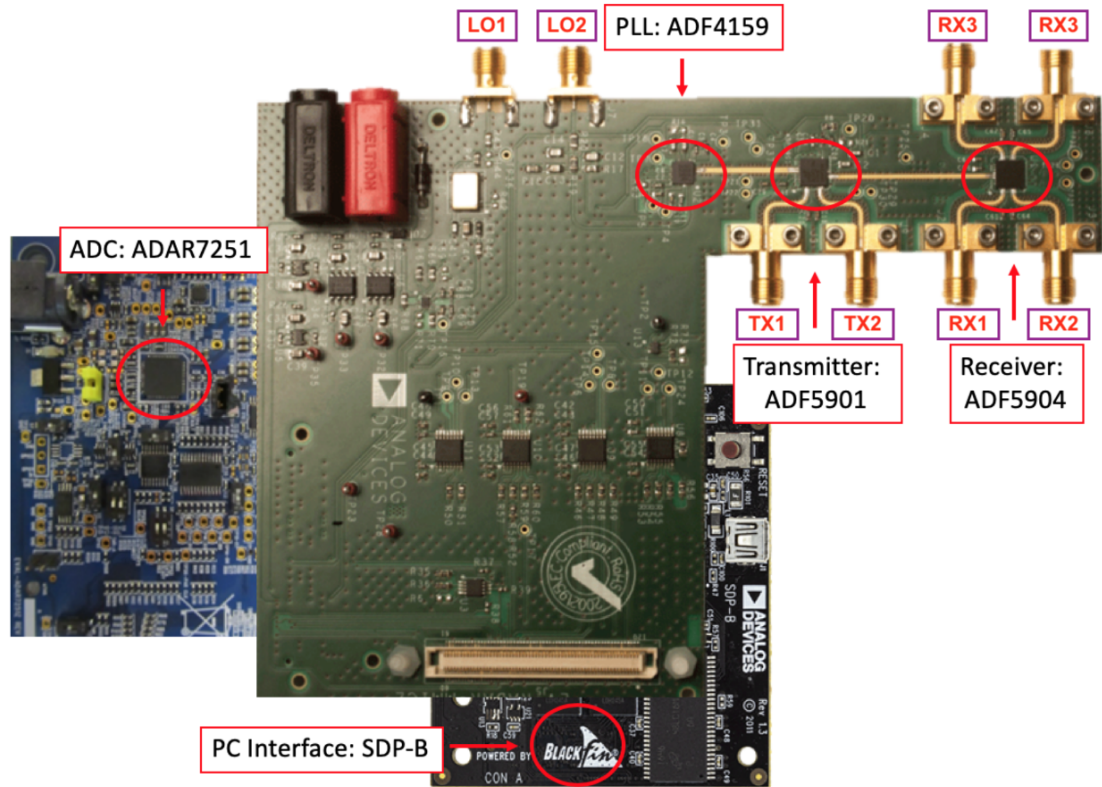


Figure 3.17: Photograph of the 2TX by 4RX radar electronics defining an individual RM.

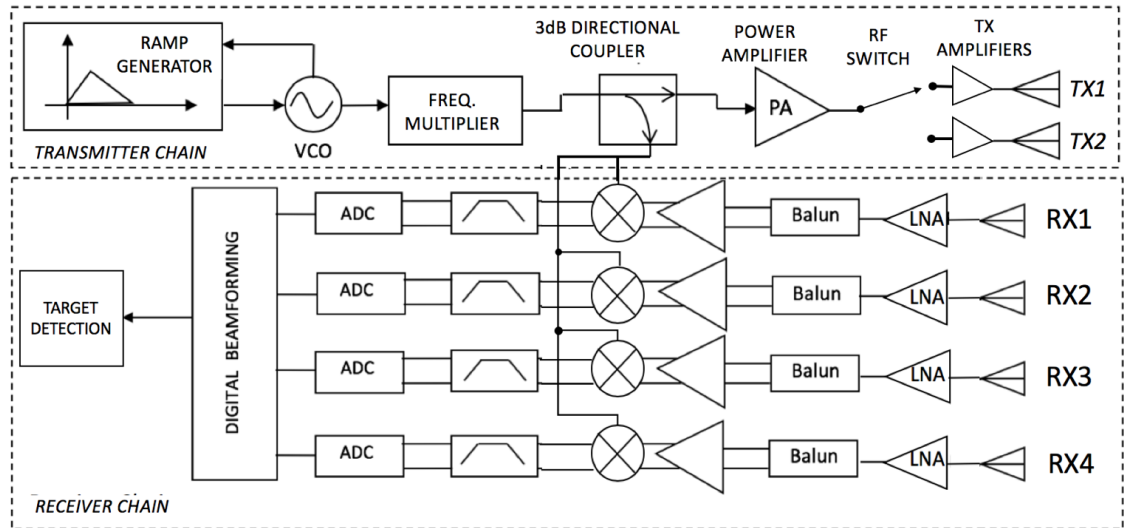


Figure 3.18: TX and RX block diagram for an individual RM.

MIMO RMs (see Figure 3.2(b)) first detect the targets individually, before integrating them further into a larger radar with multiple RMs. The following sub-sections investigate the sensitivity of detection for different radars starting from the funda-



mental mono-static radar, and then, leading to the proposed sectorized radar system (Figure 3.2(d)) which uses a network of MIMO-RMs.

## 3.5 Sectorized Radar System Measurements

### 3.5.1 Radar Measurement Setup

The radar for proof of concept has been tested in an anechoic chamber. Several trials have been carried out to verify: range approximation, range resolution and angle of arrival estimation with delay-and-sum digital beamforming. The experiments included a SIMO setup for radar range testing as well as three RMs (see in Figs. 3.19(a) and (b)), which were assigned to each sector of the FOV. This meant multiple readings were required to achieve the effective virtual apertures for the modular MIMO radar and the sectorized radar systems with each RM were required to achieve the virtual aperture of the modular MIMO and sectorized radar systems (see Figure 3.2) as outlined previously. Also, as shown in Figure 3.19(c), three square metallic targets have been used with different sizes during the experiments. A photograph of the measurements can be seen in Figure 3.19 (d).

### 3.5.2 Radar Linearity and Range Resolution Measurements

A summary of the measured linearity parameters for three radar sectors for three different RMs, representative of the three sectors, see Figure 3.2(d) are also reported in Table 3.3 while output power spectrums are shown in Figure 3.20. Measurements have been completed using a N9030B PXA Signal Analyzer from Keysight Technologies. The signal bandwidth which could be analysed for the linearity parameters was limited to 50 MHz due to the inner circuit constraints of the PXA analyzer hardware.

In comparison with the results presented in [3.42] which uses direct digital synthesis (DDS), the transmitter presented in our paper uses a fractional-N frequency synthesizer capable of generating 2 GHz of bandwidth. However, the device can transmit a signal using 13 GHz of bandwidth when triggered by an external source. Clear advantages have been further explained in [3.43], while both PLLs and DDS

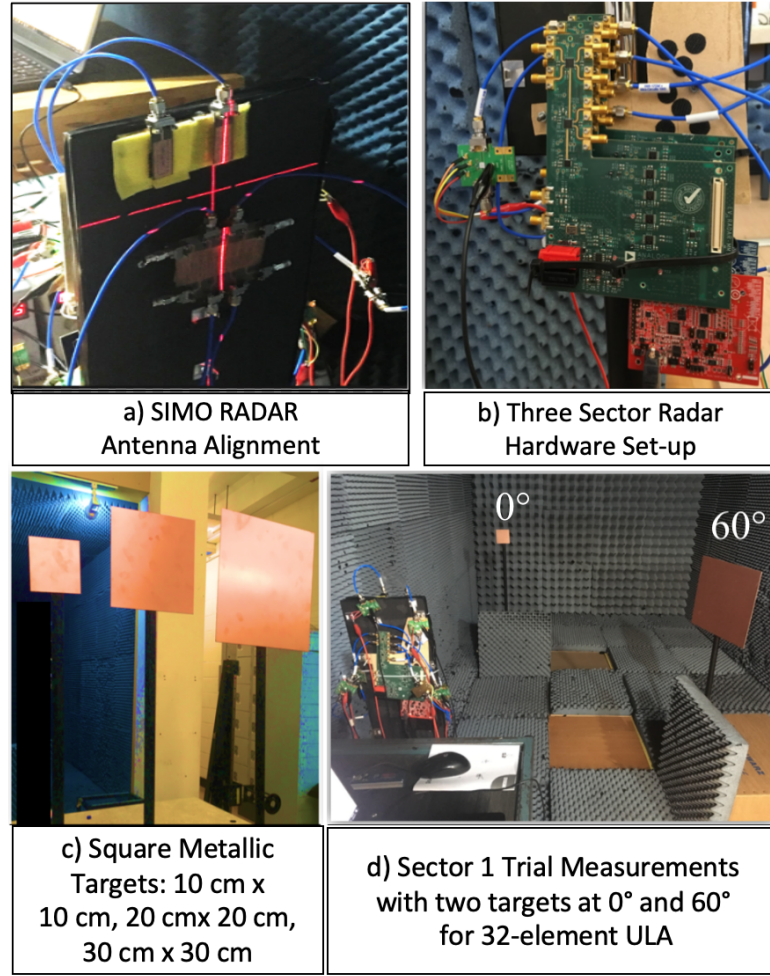


Figure 3.19: Measurement setup for the radar detection trials within an anechoic chamber with 3 RMs and three targets of dimensions: 10 cm x 10 cm, 20 cm x 20 cm and 30 cm x 30 cm. A diagram with the radar setup can be seen in appendix C

Table 3.3: Three Different Measured RM Transmitter Outputs<sup>1</sup>

Sector	Power Mean (dBm)	Average Power Deviation (dB)	Phase Error (deg)	Frequency Error (kHz)	Slope Frequency Error (kHz)	Bandwidth per Time Period (MHz/ $\mu$ s)	Impedance Matching Bandwidth(%)
1	5.01	0.52	3.59	17.18	72.41	480	6.25
2	4.95	0.53	2.97	14.17	72.21	480	6.25
3	4.82	0.55	4.12	17.17	68.37	480	6.25

<sup>1</sup>See the photos in Fig. 3.17 and 3.19(b) for an individual RM and three RMs clustered for system measurements, respectively.

can be tailored for certain applications. However, PLLs can be more cost efficient than DDS [3.43]. This defines a clear advantage when employing such modular radar systems for automotive applications.

As further explained in [3.44], the ADF4159 PLL uses a 25-bit fixed modulus .

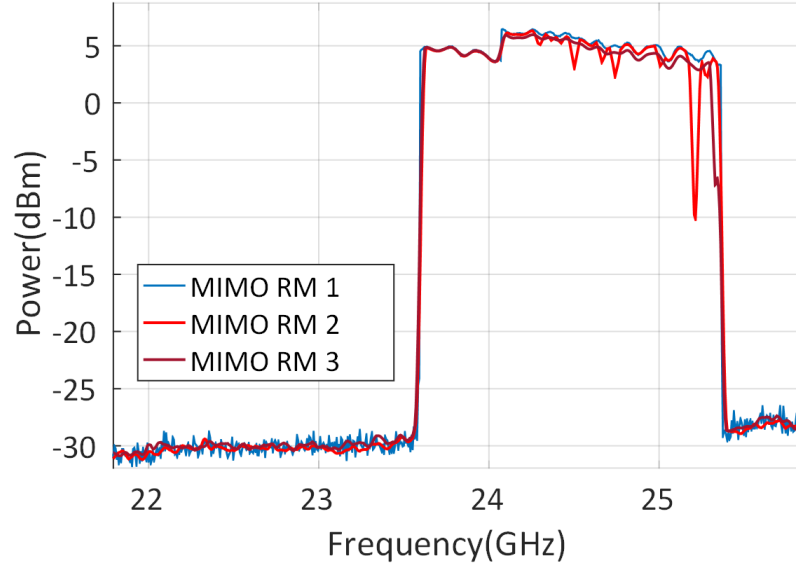


Figure 3.20: Measured transmitter spectrum response for three different 2TX by 4RX MIMO RMs (see Figure 7) by sampling TX port 1 only.

In addition, a 12 bit DAC powers the VCO and the average power consumption of the ADF4159 module is 100 mW. Also, the spurious-free dynamic range (SFDR) for the VCO can reach -90 dBc [3.44], while the frequency update time per step is 100 ns. The FFT gain of the system is 33 dB. Except for the update time, the fractional-N frequency synthesizer, employed here, shows improved figures of merit for generating the transmitting signal, in comparison to the DDS solution outlined in [3.42].

For a 1.5 GHz radar bandwidth we observe a theoretical range resolution of 10 cm by Eq. 2 (see Chapter 2). This is also confirmed by the measurements. Furthermore, a target has been swept at several distances up to 4 meters in order to check the range accuracy at both 250 MHz and 1.5 GHz bandwidths. Results are reported in Figure 3.21 where it can be observed that the radar was able to track the target in range. Also, with increased radar bandwidth, it can be observed that the measured range accuracy improved. Radar detection of targets was first measured using a SISO configuration (see Figure 3.2(a)). As can be seen from Figure 3.22, both the targets (30 cm x 30 cm and 20 cm x 20 cm) are visible for a 13 cm separation. Another test has been carried out for target separations below 10 cm and the targets are just separable. This experiment confirms that the lower limit

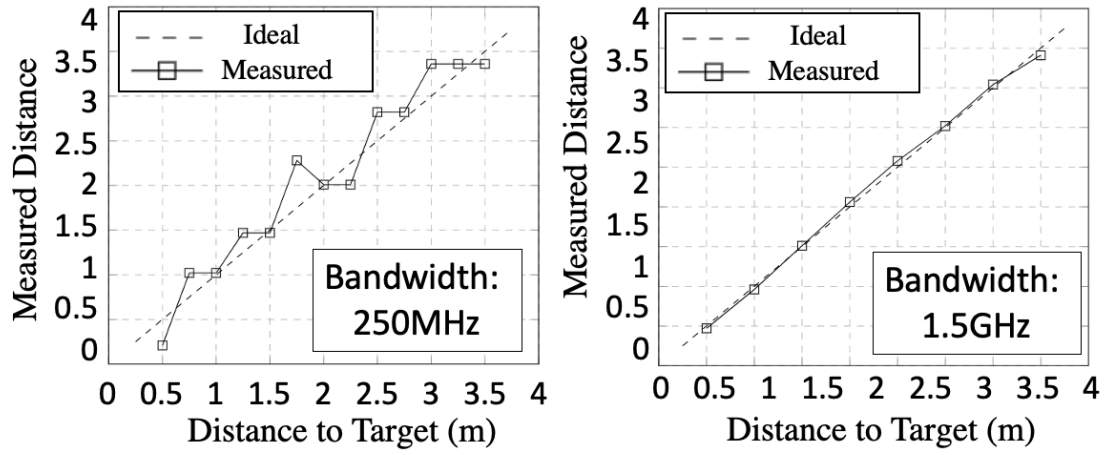


Figure 3.21: Range accuracy comparison using one target for a distance up to 4 meters using 250MHz and 1.5GHz bandwidth.

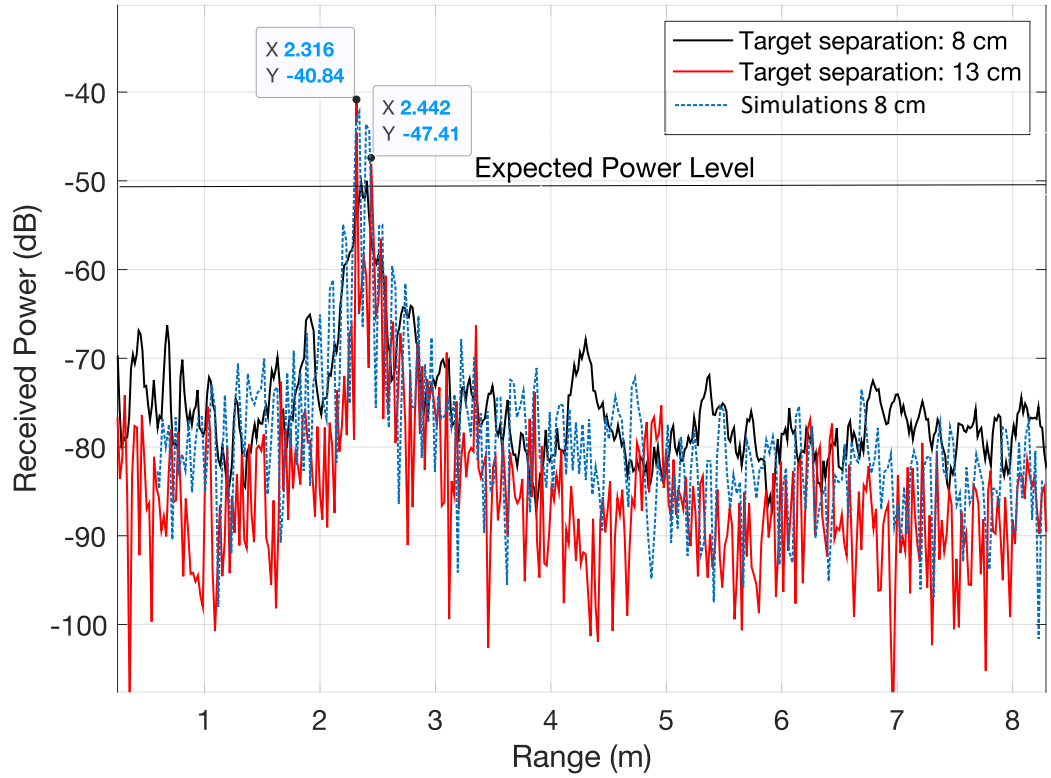


Figure 3.22: Range resolution simulations and measurements with two targets separated above and below the angular resolution limit of 10 cm using a 1.5 GHz bandwidth.

for the range resolution of the radar is just above 8 cm.

### 3.6 Angular Resolution Measurements

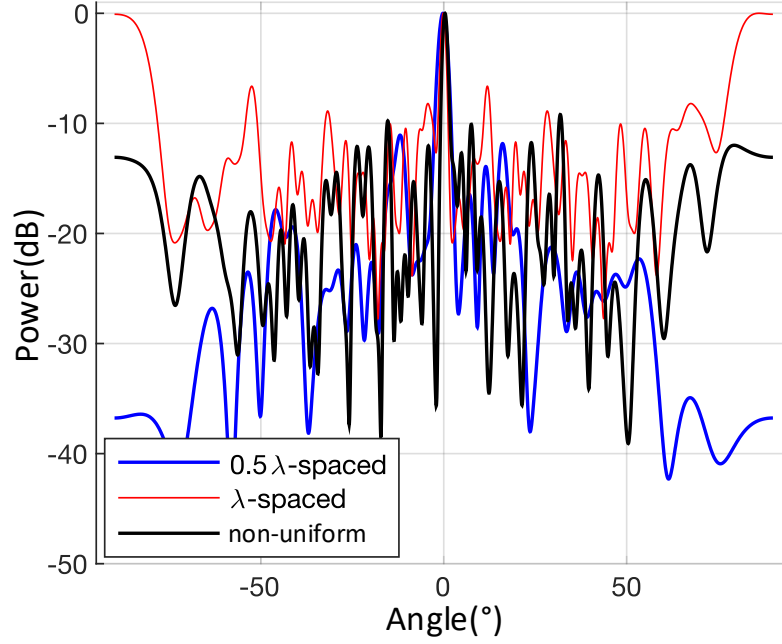


Figure 3.23: One target comparison:  $\lambda/2$ ,  $\lambda$  and non-uniform spacing with setup as described in C.1, just for one target.

Measurements have been carried out for  $\lambda/2$ -spaced,  $\lambda$ -spaced and non-uniform sparse receiver configurations. Since each RM is defined by using only two transmitters and four receivers, the measurements for the 32-element virtual receiver array, for each sector, have been carried out by displacing the MIMO RMs at positions displaced exactly  $4\lambda$  from each other. This measurement approach and by considering the same target scenario, has permitted the authors to predict the performance of the modular MIMO radar system for the 32-element virtual receiver array, whilst considering both uniform and non-uniform spacing.

The results of the measurements with one target as well as two targets spaced at different angular separations are shown in Figs. 3.23, 3.24, 3.25 and 3.26. For the multiple target scenarios, the targets have been measured while spaced at decreasing offsets of  $2^\circ$  in order to observe the responses. The results show that the non-uniformly spaced radar is managing to detect both targets in all situations, even when these targets are spaced at an angular distance of  $\pm 2^\circ$ . Also, the side-lobe levels (SLLs) are about 7 dB below (or better) from the main target estimates for

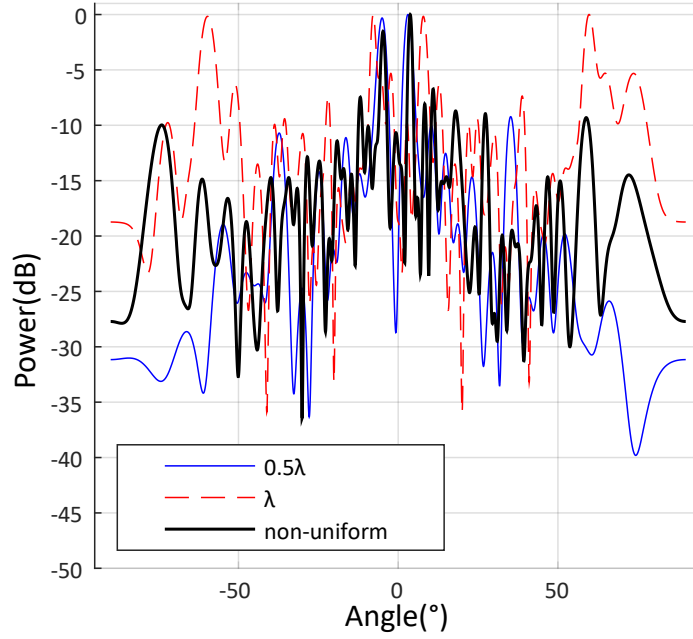


Figure 3.24: Radar measurement comparison for an 8 degree angular target separation:  $\lambda/2$ ,  $\lambda$  and non-uniform spacing. It should be mentioned that grating lobes are observed for the  $\lambda$  spaced array at about  $\pm 60^\circ$  while the radar measurement with the non-uniform receiver array clearly distinguishes the targets and where grating lobes and SLLs are about -10 dB or lower. The setup is presented in Fig. C.1

the angular spectra. In addition, it can be observed that the grating lobes are mitigated at about  $\pm 90$  degrees for the non-uniform spaced array when compared to the  $\lambda$ -spaced radar receiver. For example, grating lobes are reduced to about -12 dB (or more) in Figure 3.23 for the non-uniform array. Similar results are observed in Figs. 3.24, 3.25, and 3.26. These SLLs could generally be further improved, and providing motivation for future research. For example, different strategies to reduce SLLs include amplitude weighting for the antennas (such as Gaussian or Tchebyshev [3.45]) as well as time-domain smoothing through spectral multiplication [1.7, 3.46].

Most radar systems assume that a single radar covers the FOV in the horizontal plane. The sectorized MIMO radar system, on the other hand, presents a novel and improved solution to previous radar works (see Table 3.1) by employing multiple RMs in order to discretely sample the angular space. The front horizontal plane of the radar can be divided into three sectors allowing for precise detection (see Figure 3.2(d)). Moreover, this allows for data to be sampled at each RM, giving a combined

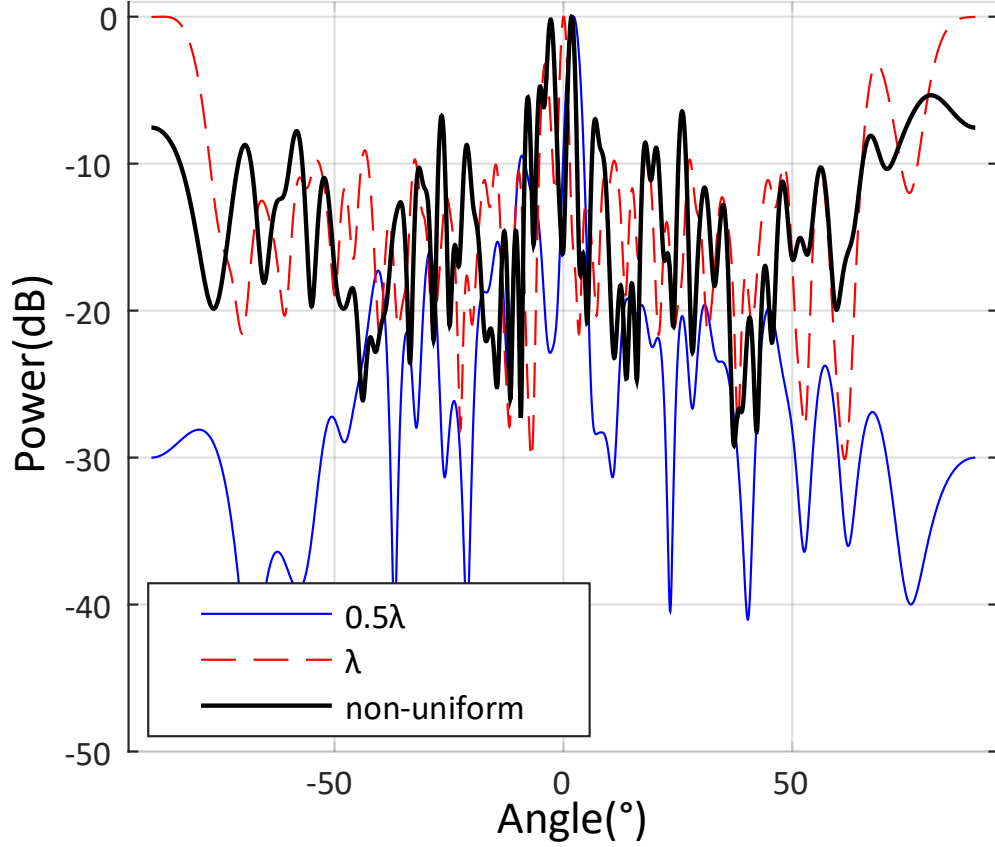


Figure 3.25: Radar measurement comparison for a 6 degree angular target separation:  $\lambda/2$ ,  $\lambda$  and non-uniform spacing, which, is the only effective radar antenna which can clearly distinguish the two targets; i.e. the non-uniform spaced array. The setup is presented in Fig. C.1

response for the three sectors by data fusion. Results are shown in Figure 3.27.

Each of the modular MIMO radars for each sector is defined by a 32-element virtual receiver array with non-uniform spacing as described in the previous sections. Since the switching speed of the RF ports is completed in approximately 50 ns between each transmitter, the total switching time for the radar system is estimated to be 0.3  $\mu$ s. Also, the time required to process the targets by the beamforming algorithm varies between 22 ms and 30 ms for each sector. The computer hardware used for this data processing is performed using a laptop running MATLAB. In particular, the computer characteristics are as follows: a 2.6 GHz Dual-Core Intel Core i5 processor (I5-4278U), with 8 GB of DDR3 memory, using an Intel Iris graphics card of 1536 MB. It is expected that the performance can be improved if the system is transitioned to FPGA-based processing. The modular MIMO radars,

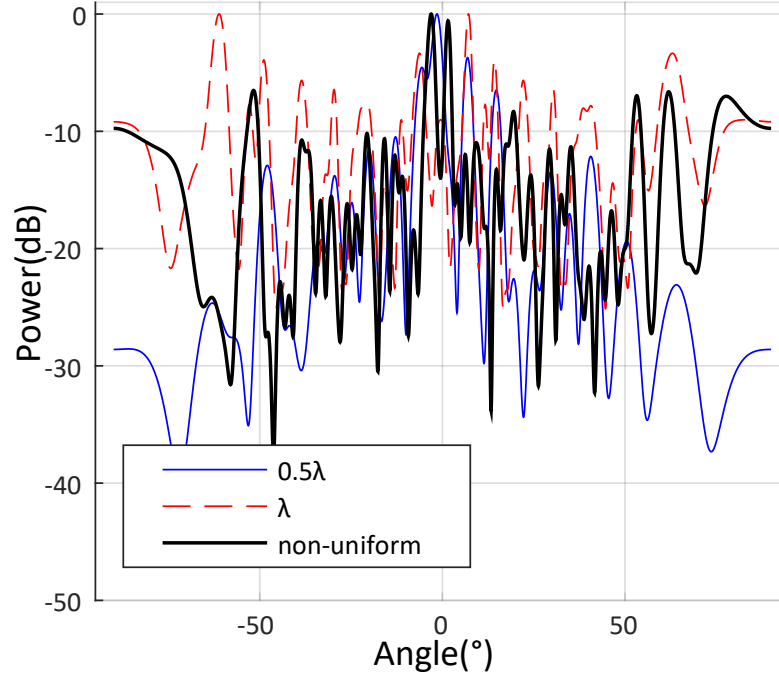


Figure 3.26: Radar measurement comparison for a 4 degree (or  $\pm 2$  degrees) angular target separation:  $\lambda/2$ ,  $\lambda$  and non-uniform spacing. Again, similar to Figure 3.25, the non-uniform spaced array is the only virtual receiver than can decipher the two targets and with low SLLs for the angular spectrum estimate. The setup is presented in Fig. C.1

see Figs. 3.2(c and d), are also tilted which are representative of the final front-end configuration, so that non-overlapping horizontal coverage can be obtained uniformly for the combined radar views. If the radar beams would overlap then it is possible to see some unexpected effects in detection due to the interference caused by the adjacent radars.

Figs. 3.27 (a) and (b) show how multiple radar sub-modules extend the horizontal coverage of the radar system and that non-uniform spacing can avoid false target detection. The modification of the antenna beamwidth with respect to angle can be found in 5.5.1. This figure highlights two targets consisting of one larger metal plate (30 cm x 30 cm) at  $60^\circ$  from the middle line of the radar system at 2.5 m distance while the smaller (20 cm x 20 cm) is situated at 4 m distance at the middle line of the radar. It can be seen from the simulation results of the scenario, depicted in Figure 3.27 (a) how  $\lambda$ -spaced antenna arrays suffer from grating lobes.



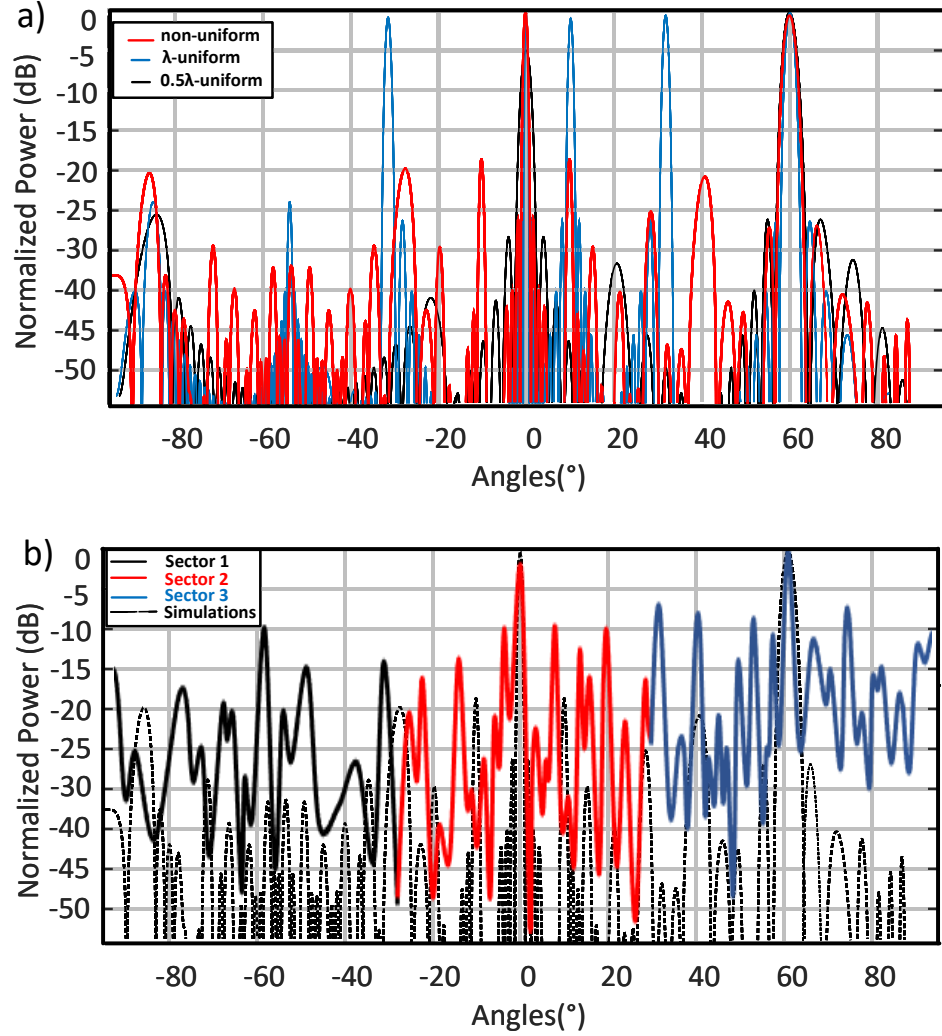


Figure 3.27: Simulations (a) and measurement (b) results for a radar trial detecting two targets at  $0^\circ$  and  $65^\circ$  as identified in Figure 3.19(d). The targets have been placed at an angular separation of  $65^\circ$  to highlight the improvement of the sparse array approach compared to the  $\lambda/2$ -spaced and  $\lambda$ -spaced uniform array. The setup is similar to the previous measurements which are described in Fig. C.1

### 3.6.1 Power budget for complicated radar scenarios

In order to get correct measurements, the radar system has to be calibrated with regards to the losses of the system due to several component such as cables and other elements on the transmit/receive path. As can be seen in [3.47], targets such as a car can have complex shapes and metallic targets will always reflect back more energy in comparison to a target which is made of a non-reflective material. Therefore, pedestrians are much more difficult to detect in comparison to a car [3.47]. If we

refer to the initial calculations for the radar link budget (see Section 2.10), we can easily recognise that some targets will overshadow other targets. In this case, the SNR and grating lobes will affect radar performance. One solution for this problem is to provide more amplification on either transmit or receive path, however, another idea that was implemented by another colleague in the Samsung project is the use of passive transmitter beamforming techniques, such as the use of a Butler matrix system, where the transmitter is able to scan the field of view and offer more power in the direction where there is less scattered energy. For more information about this solution, please see [3.39]. The other issue with radar detection is the formation of clutter, and multipath signals which come back at the receiver and make the transmission more difficult to carry out. Some of these scenarios are also discussed in Appendix C where the multiplication algorithm is used for improving SLL response.

### 3.7 Discussion

In comparison to the mentioned literature [2.23, 2.34, 2.45, 2.56, 2.58, 3.6], the non-uniform radar presented in this chapter provides maximum performance in all areas of detection in terms of  $\pm 90^\circ$  FOV, angular resolution  $\Theta_{3dB}$ , and detection time (see Table 5.1). Increased receiver aperture length improves the angular resolution of the radar while range resolution is improved by the operating bandwidth of the employed SIW antennas. When used appropriately, the modular MIMO radars can maximize FOV for the three sectors while targets are detected due to the simple digital beamforming method and MIMO processing. This introduces a sectorized MIMO radar architecture which achieves full coverage of the horizontal plane ( $\pm 90^\circ$ ) using numerous modular MIMO RMs and supports low-cost mass production rather than the assembly and manufacturing of a larger scale and equivalent radar system with the same number of receiver elements.

In comparison with other methods presented in other chapters of this thesis, the sectorized radar approach is preferable for situations where a larger FOV is desired, such in the case of short-range radars (SRRs) since these need to cover a wide FOV and also increased range resolution is necessary for targets that are up to a range determined by the near field region of the radar system [1.1]. The sectorized

radar approach also would benefit from a reduced SLL scheme, where improved non-uniform spacing combined with either spectral smoothing or tapering would offer a significant advantage in terms of angular resolution for target detection.

### 3.8 Summary and Conclusions

This chapter has presented a sectorized MIMO radar system which achieves high range resolution while being able to detect targets with an field-of-view of  $\pm 90^\circ$  and resolving targets with an angular resolution of  $4^\circ$ . Despite increased signal processing requirements due to the multiple radar sub-modules and data fusion for the three sectors, scalability and repeatability make this design a good candidate for mass production. Also, the angular resolution achieved by the non-uniform sectorized two-mode MIMO radar is better than the standard  $\lambda/2$ -spaced array, offering an experimentally verified half-power beamwidth of  $2.2^\circ$ .

It should also be mentioned, that by employing the aforementioned non-uniform radars, channel noise and signal delays are reduced to a minimum in comparison with a larger scale and more conventional transmit and receiver array, mainly due to the fact that microstrip-based corporate feeding network or other large-scale beam forming networks (i.e. a Rotman lens for example) are not required. In addition the two-tier detection approach allows for a three-fold aperture in comparison to an uniform array alternative. This distributed sensing concept will also prove useful in the application of the spectral smoothing multiplication technique when multiple radars are employed (explained in more detail in the next chapter, Chapter 4) In summary, the presented system design allows for individual sub-sector sampling enabling a modular and sectorized MIMO radar approach. This can support the development of new beamforming techniques for automotive short-range radars with competitive range and angle target resolution.

### 3.9 Contributions by the candidate

In this chapter, the candidate has taken the idea of sectorization from idea to practical implementation with radar system measurements in the anechoic chamber. Specif-

ically, the receiver antennas designed by Pascual Hilario has been tested with the sectorized radar idea by the candidate. The candidate has done the measurement setup and taking the measurements in the anechoic chamber and also designing the beamforming algorithm for the MIMO processing, taking beampattern measurements of the transmitter and receiver antenna using the near field and far field systems of Heriot-Watt University. Moreover, the candidate has developed the two tier process of beamforming with non-uniform antenna spaced array, allowing for improved radar performance and doing the measurements of such system. The results of this work was also published in the Journal of Microwaves after a peer-review process. Throughout the thesis, the candidate shows a comparison of theory simulations and measurements which have been carried out by himself. The transmitter spectrums of the three radars and the range accuracy tests have also been completed by the candidate. Each of the radar measurement scenarios with the three radar configurations has been measured by the candidate in the anechoic chamber.

# Chapter 4

## Signal processing techniques with improved target detection for MIMO Automotive Radar

When considering imaging resolution capabilities, microwave and millimeter-wave radar systems have less resolution compared to camera and LiDAR[1.3], however they are able to image in adverse weather conditions where other technologies have difficulty obtaining the same.. Hence, achieving improved resolution for automotive radar and accurate target detection plays a key role in the progress towards autonomous driving [1.2]. This is especially important in high density urban environments where the radar has to discriminate between multiple targets in a short period of time.

The constraint with radar performance is limited by the actual physics of the problem [1.3]. The angular resolution of the radar is given by the RF front-end antenna aperture dimension and the capability of the signal processing back-end given by the beamformer [1.4]. The aperture length can be real or virtual, as described in Chapters 2 and 3 with MIMO antenna arrays, while having more transmitter receiver pairs increases resolution at the expense of creating bulkier sensors [1.3]. Higher frequencies of operation and larger bandwidths can drastically enhance key performance indicators, however, these are often limited by frequency regulation, manufacturability readiness, and large scale production [1.3].

## 4.1 Motivation and goal

This chapter has the goal to introduce and describe three signal processing techniques that help smooth out the response of the radar and advance its performance:

- Spectral smoothing multiplication
- Interpolation
- Extrapolation

In addition to these concepts, highly separated radars are also discussed as a possibility of enhancing accuracy for automotive radar detection. The motivation for this work is to find other techniques which improve both the resolution and accuracy of the radar.

## 4.2 Spectral smoothing using beampattern multiplication

### 4.2.1 Background

In radar detection, angular target estimates such as the ones processed using digital beamforming are mostly shaped similarly to a Bell-shaped curve as seen in a normal or Gaussian distribution with a mean and standard deviation. Chapter 2 introduces the concept of beamforming, and explains both analogue and digital beamforming. In this section, the response given by the radar can be combined and smoothed in order to provide a more realistic angular target response. In the following, an explanation is given as to why this feature is possible.

The beamwidth of the radar angular return determines the radar capability of being able to discriminate between multiple targets. If the angular target returns are narrower in width, then the radar is capable of resolving multiple targets. The goal is to find the best description of the mathematical result of "thinning" the beamwidth of radar returns by angular target multiplication. A frequency domain signal  $E(f)$  is defined as a sinc-shaped function as shown in Figure 4.1.

The goal is to find the best description of the mathematical result of "thinning" the beamwidth of radar returns by angular target response multiplication. A

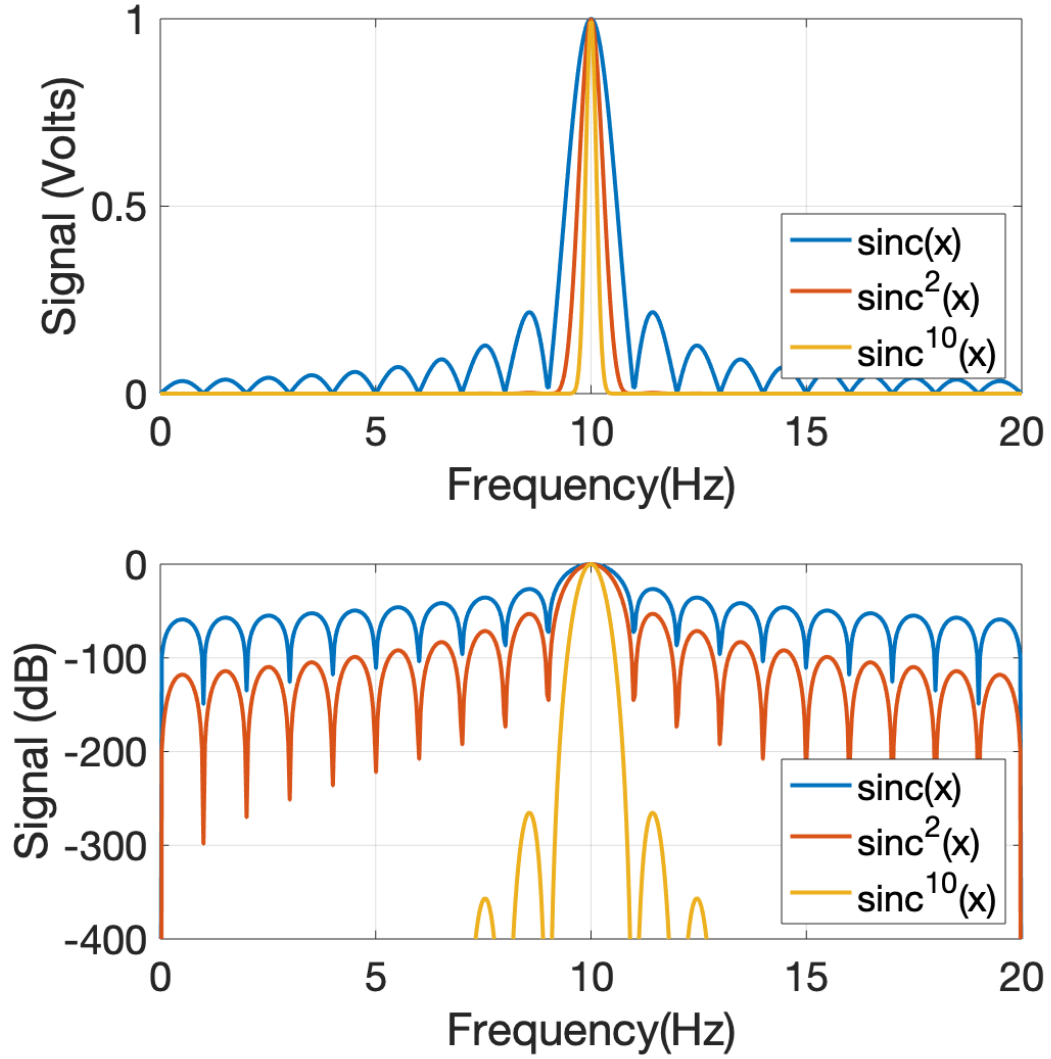


Figure 4.1: Comparison of linear (upper) and logarithmic (lower) representations of  $\text{sinc}(x)$ ,  $\text{sinc}^2(x)$ ,  $\text{sinc}^{10}(x)$ .

time domain signal  $E(t)$  is defined as a sinc-shaped function and the beamforming response for this signal is shown in Figure 4.1,

$$E(t) = 2T \text{sinc}(2\pi t/T) \quad (4.2.1)$$

where  $T$  is the period of the function and  $t$  is the time of the signal. In order to quantify the efficiency of the angular target response multiplication, let us also define a noise-free signal in the time domain  $E_0(t)$ . The height of such a signal is

given by its zero-point. Thus:

$$E_0(0) = \int_{-\infty}^{\infty} E_0(t) dt . \quad (4.2.2)$$

After smoothing, the noise-free general line becomes:

$$E'_0(0) = W(0) \cdot E_0(0) \quad (4.2.3)$$

$$= \int_{-\infty}^{\infty} A(t) dt \cdot \int_{-\infty}^{\infty} E_0(t) dt \quad (4.2.4)$$

where  $A(t)$  is our time domain smoothing function. Now the relative distortion,  $\Delta(t)$  of the line shape  $E_0(t)$  can be defined as:

$$\begin{aligned} \Delta(t) &= \frac{E'_0(t) - E_0(t)}{E_0(t)} \\ &= \frac{W(t) \cdot E_0(t) - E_0(t)}{E_0(t)} \\ &= W(t) - 1 = \mathcal{F}[A(t)] - 1 \end{aligned} \quad (4.2.5)$$

$$= \int_{-\infty}^{\infty} A(t) e^{-i2\pi ft} dt - 1 \quad (4.2.6)$$

while the maximum relative distortion can be found at the peak height:

$$\Delta(0) = W(0) - 1 = \int_{-\infty}^{\infty} A(t) e^{-i2\pi 0 \cdot t} dt - 1 \quad (4.2.7)$$

$$= \int_{-\infty}^{\infty} A(t) dt - 1 . \quad (4.2.8)$$

Another indicator highlighting smoothing effects is the relative distortion at full-width half maximum (FWHM) of the line,  $\delta_{1/2}$  as defined in [3.46]. This is a measure of how much the resolution is improved after smoothing, compared to the overall line smoothing.  $\Delta f_{1/2}$  is the full-width half maximum of the signal, while the  $\Delta' f_{1/2}$  is the full-width half maximum of the signal after smoothing. The relative distortion at FWHH is therefore defined as [3.46]:

$$\delta_{1/2} \approx \frac{-E_0(0)\Delta(0)}{E'_0(0)} = -\frac{\Delta(0)}{\Delta(0) + 1} . \quad (4.2.9)$$



A measure of enhancement is the signal-to-noise ratio (SNR) improvement. In order to reach this result, the random noise white spectrum needs to be found. The SNR of the smoothed signal is thus the ratio between its peak and the root-means squared (RMS) of the noise:

$$\left(\frac{S}{N}\right)' = \frac{E'_0(0)}{\sqrt{N_A^2}} = \frac{\sqrt{2f_b} \int_{-\infty}^{\infty} A(t)dt \cdot \int_{-\infty}^{\infty} E_0(t)dt}{n^2 \int_{-\infty}^{\infty} A^2(t)dt} \quad (4.2.10)$$

If we want to compare different smoothing functions, it is possible to define an intrinsic smoothing function  $A_0(t)$  and thus quantify the SNR enhancement, annotated with  $Q$ . The intrinsic smoothing function can be defined as any of the aforementioned functions: *sinc*-like functions, *sinc*<sup>2</sup>-like functions, and Lorentzian functions. As mentioned in [3.46],  $Q$  is defined as:

$$Q = \frac{(S/N)'}{(S/N)_0} = \frac{\int_{-\infty}^{\infty} A(t)dt \cdot \sqrt{\int_{-\infty}^{\infty} A_0^2(t) dt}}{\int_{-\infty}^{\infty} A_0(t)dt \cdot \sqrt{\int_{-\infty}^{\infty} A^2(t) dt}} \quad (4.2.11)$$

In the following, we will apply this smoothing approach on these base functions in order to determine the best SNR enhancement from the existing set of functions. This process will allow us to determine which response will produce a better smoothing when applying the multiplication procedure.

### 4.2.2 Smoothing Using a sinc Function

Smoothing with a sinc function has less distortion in comparison to other smoothing, such as a Lorentzian smoothing function [3.46]. The equivalent time domain response for this smoothing is the boxcar apodization function [3.46]:

$$A(t) = \begin{cases} 1 & , |t| \leq T \\ 0 & , |t| > T \end{cases} \quad (4.2.12)$$

The smoothing factor ( $K$ ) is dependent on the the standard deviation ( $\sigma$ ) and the

relative distortion of signal ( $\Delta(t)$ ) [3.46], whereas the maximum smoothing factor ( $K_0$ ) is dependent on the standard deviation and the maximum relative distortion ( $\Delta(0)$ )

$$K = \frac{2\sigma}{\Delta(t)} \quad (4.2.13)$$

$$K_0 = \frac{2\sigma}{\Delta(0)} \quad (4.2.14)$$

We are able to quantify the exact improvement of our smoothing multiplication function of the signal to noise enhancement by evaluating Q:

$$Q = \sqrt{\frac{K_0}{K}} \cdot (1 - \exp(-S_0/2)) . \quad (4.2.15)$$

, where  $S_0$  is the resultant signal from the smoothing process [3.46].

### 4.2.3 Multiplication Smoothing Function Practical Implementation

The radar system has been designed so that a target is seen in multiple frames. After receiver beamforming, the spectral beam pattern return generally takes the form of a sinc function. As it was discussed at the beginning of the chapter, the smoothing of spectral data can occur as a result of applying sinc, sinc<sup>2</sup> and Lorentzian functions [3.46]. According to [3.46], the best smoothing function is the sinc function for spectral data. Similarly when considering radar beamforming, sinc functions based on the multiplication of radar beam patterns can provide a smoother response with the precondition that target returns are above the noise level.

The composite radar system formed by 4 sub-modules has been designed to allow multiple spectrum multiplication of the individual radar patterns. The MIMO sub-module radar configuration can be observed in Figure 4.2(a). In this case, the radar sub-module is formed by 2 transmitters (2TX) and 4 receivers (4RX), forming 8

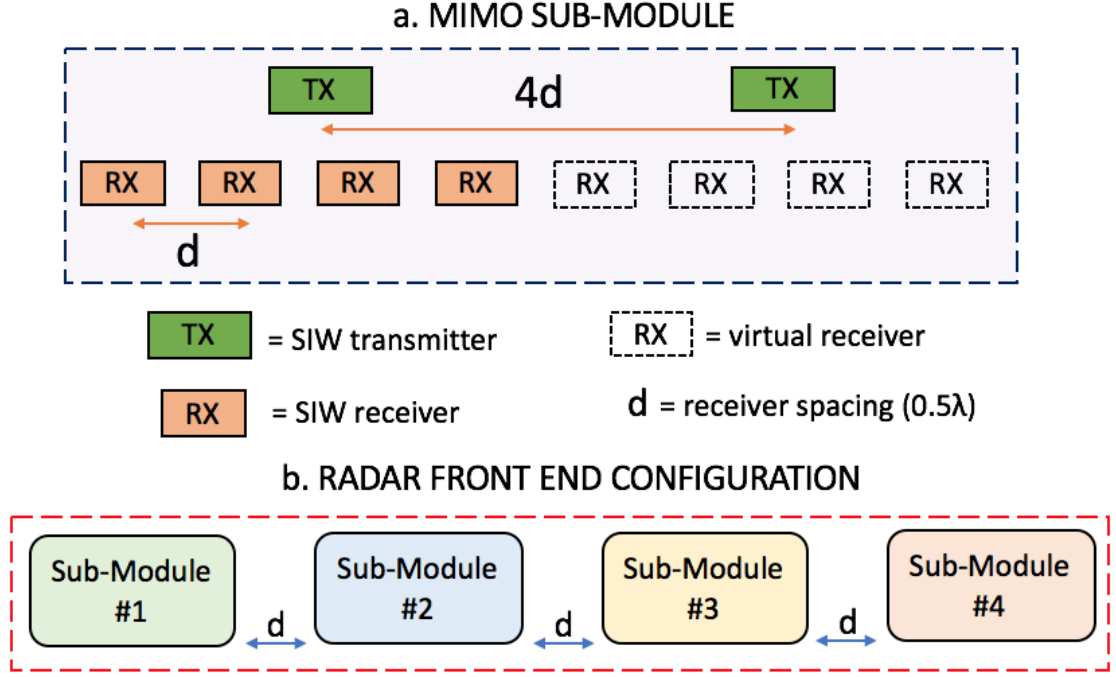


Figure 4.2: Radar configurations: a. sub-module b. complete radar.

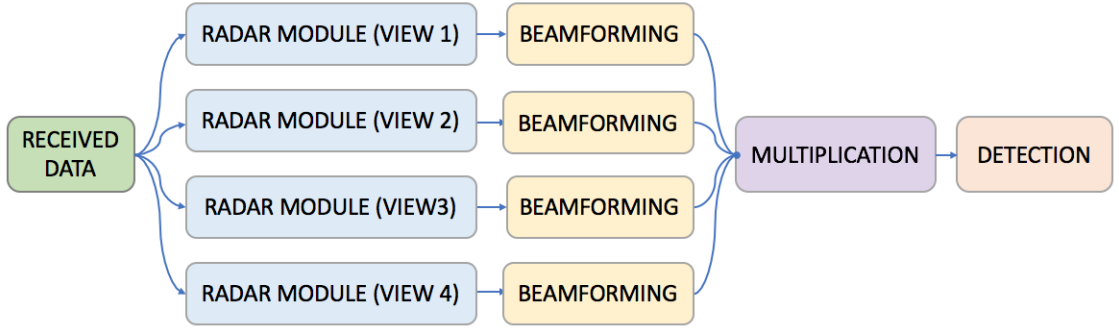


Figure 4.3: Radar signal processing approach where multiplication is employed in the spectral domain.

virtual elements in total. Each separate radar view contributes to the rendering of an image of the target. By combining the data from 4 radar sub-modules, we are able to obtain a 32-element virtual array. MIMO radar configurations allow for large virtual arrays to illuminate the target, while being small in size. The configuration of the radar sub-modules are depicted in Figure 4.2(b). The  $0.5\lambda$  distance between multiple views is the same as the inter-element spacing ( $d$ ) since that preserves the uniformity of the virtual linear antenna array.

Multiplying the sub-module radar beam patterns results in smoothing of each sub-radar view. The result converges to a combined sinc function with the peaks increasing and the troughs decreasing in magnitude. This characteristic is advan-

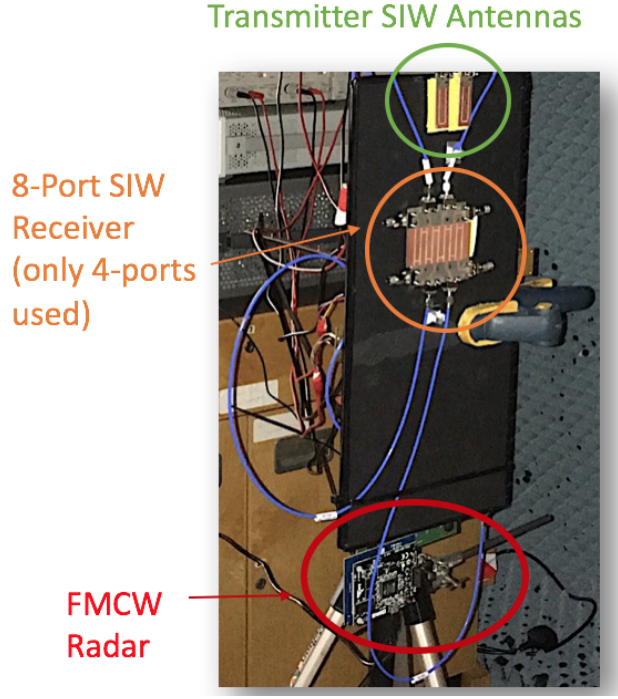


Figure 4.4: FMCW MIMO radar sub-module calibrated in an anechoic chamber with antenna transmitters at the top, 8-port receiver underneath the transmitter and radar system connected with 2.92mm cables connected from the back of the radar stand.

tageous in radar beam pattern analysis since the target levels are increasing in magnitude while the side lobe levels decrease, refining radar accuracy.

To process the receiver data, the digital beamforming network will first process radar responses individually and then apply a beamforming algorithm for each view. The spectral beam pattern for each response is then multiplied, after which target detection takes place for the composite radar system. The process is illustrated in Figure 4.3. The system has been measured in a calibrated anechoic chamber with a metallic target as described in Chapter 3. The setup of a radar sub-module can be seen in Figure 4.4, while the modular beampatterns, their spectral multiplication and the MIMO response are plotted in Figure 4.5.

#### 4.2.4 Measurement Results

The side-lobe level improvement by the proposed method is 13dB and the beam pattern of the MIMO response is seen to have a smaller half-power beamwidth than the multiplication technique. This is caused by the sub-radar antenna array aperture length of 4 elements while the virtual array for the MIMO radar will have

Table 4.1: Radar Specifications for Multiplication Measurement Trial

Number of Modules	4
Sub-Module Transmitters	2
Sub-Module Receivers	4
Virtual Array Elements	32
Carrier Frequency	24GHz
Bandwidth	1.5GHz
Sweep Period	5ms
ADC resolution	12-bit
Half-power Beamwidth	14°
Range resolution	10cm

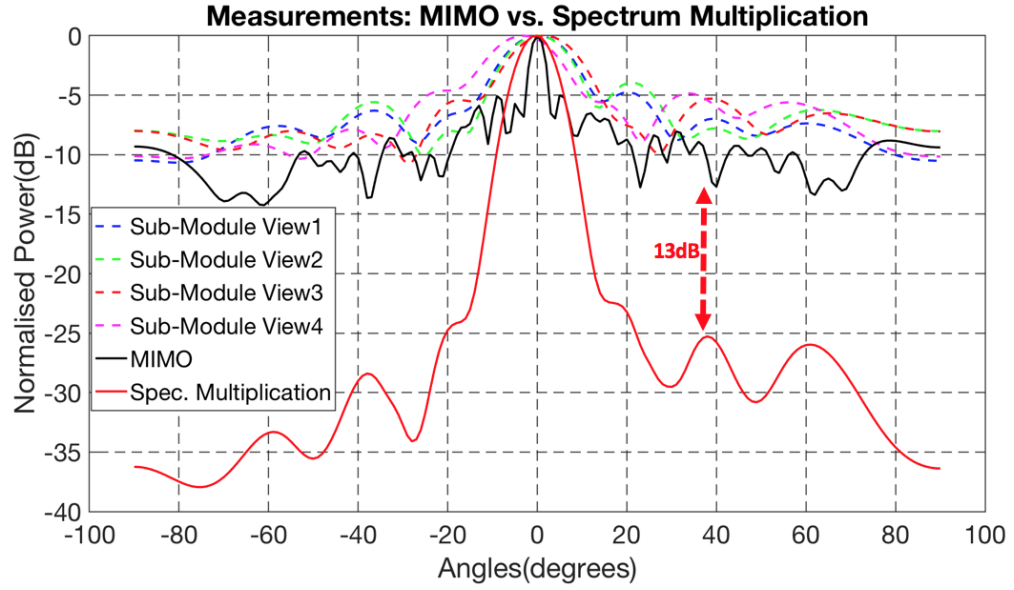


Figure 4.5: Measurements for a target at broadside for MIMO radar (4TX by 8RX elements) and spectral beam pattern multiplication (4 sub-radars with 2TX by 4RX for each).

the resolution of an equivalent 32-element array at the receiver. Also, the angular resolution of each sub-radar module can be improved by increasing the number of elements. As a result of this change, the half power beamwidth of their pattern multiplication decreases. The individual MIMO responses are multiplied to increase SNR, improve the pattern resolution, and reduce side lobe levels compared with individual MIMO and multiplication algorithms.

#### 4.2.5 Additional simulations for the Multiplication method

Although the improvement for the multiplication method can be clearly seen for the single target scenario, it is often the case that many targets are present in the

Table 4.2  
Additional simulations for Multiplication (Appendix B for full results)

Case No.	Radar cross section difference between targets (dB)	Multiplication factor	Side lobe level (dB)	Are both targets identifiable?
1	10	1	-15	Yes
1	10	2	-100	Yes
1	10	3	-200	Yes
2	20	1	-13	No
2	20	2	-100	No
3	2	1	-11	Yes
3	2	2	-45	Yes
3	2	3	-150	Yes

environment when detection takes place. It is often that there are multiple SLL levels which might hinder the detection of some targets. In the case of a pedestrian and a car, the difference between the two is about -20 dB, which makes multiplication behave differently, and these cases are analysed in Appendix B . These simulations probe the cases where we would have either a pedestrian and a car, with two different radar cross sections, as well as applying the multiplication method with two cars present in the environment. A summary of the simulated cases can be found in Table 4.2.

## 4.3 Interpolation and Extrapolation of Antenna Array Data for Enhanced Radar Detection

### 4.3.1 Background

Radar front-ends are characterised by an effective aperture length which is usually quantified by equally spaced elements either at the transmitter or receiver and in general it is defined as Uniform Linear Array (ULA). In this section we will approach two methods which can potentially enhance detection accuracy for automotive radar scenario:

- **Interpolation** is a method for adding new data points within a range of a set of known data points. In our case, we want to use the interpolation method to add pertaining data points which will improve resolution for the receiver antenna array within the data set of raw data signals from the antenna element sensors.

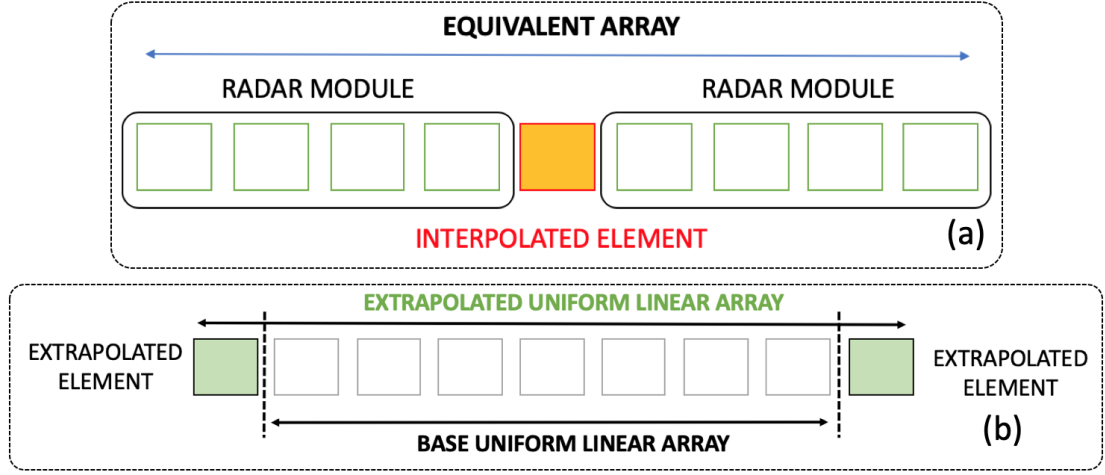


Figure 4.6: Template for obtaining an interpolated (a) or extrapolated (b) antenna array design for an uniform linear array (ULA), with elements spaced at  $\lambda/2$  inter-element spacing.

- **Extrapolation** is similar to interpolation but it differs due to its approximation of the missing element data on the outskirts of receiver element array positions.

MIMO radar can provide increased angular resolution for automotive radar because it uses a larger antenna aperture size. This idea is further expanded in order to achieve higher angular resolution with just a small fraction of signal processing time. Radar front-ends are characterised by an effective aperture length, which will be quantified in this paper in terms of an ULA. We will assume a baseline ULA, which will be the same as the hardware setup and all additional elements are interpolated/extrapolated elements. This concept is illustrated in Figure 4.6. For a MIMO antenna array, the transmitting and receiving steering vectors can be written as [2.11]:

$$s_t = [e^{-j\phi_{t1}}, \dots, e^{-j\phi_{tM}}] \quad (4.3.1)$$

$$s_r = [e^{-j\phi_{r1}}, \dots, e^{-j\phi_{rN}}] \quad (4.3.2)$$

where  $M$  and  $N$  are the number of transmitting and receiving sensor elements, the transmitting phases are  $\phi_t = \omega_0 \tau_m$ , where  $m = 1, \dots, M$  are the transmitting antenna indices, and receiving phases are  $\phi_r = \omega_0 \tau_n$ , where  $n = 1, \dots, N$  are the receiving antenna indices,  $\omega_0 = 2\pi f$  is the angular frequency of the incoming wave,

and  $\tau_m/\tau_n$  are the delays for the transmitting and receiving antenna elements.

The MIMO steering vector in this case is the Kronecker product of the two vectors[2.11]:

$$s = s_t \otimes s_r \quad (4.3.3)$$

$$s = [e^{-j(\phi_{t1}+\phi_{r1})}, \dots, e^{-j(\phi_{N+1}+\phi_{M+1})}] \quad (4.3.4)$$

It is possible by using a piecewise function, formed of a set of polynomials to estimate the first and last element data values:  $e^{-j(\phi_{t0}+\phi_{r0})}$  and  $e^{-j(\phi_{N+1}+\phi_{M+1})}$  for the steering vectors. In our approach, a shape-preserving extrapolation method is used. The data point which is queried, is estimated based on a piece-wise cubic extrapolation method of the adjacent values at the grid points. The condition of applying this method is  $C^1$  continuity over the acquired data, meaning the function we are trying to obtain must be differentiable and its derivative must be continuous, or monotone.

Let  $p(x)$  be the function we are trying to estimate on the subinterval  $I_i$  and  $f_i$  and  $f_{i+1}$ , two adjacent data values at the breakpoints in this subinterval, where  $i$  is the index of the data point.  $I_i$  is defined as  $[x_i, x_{i+1}]$ . According to [4.1], it is possible to reconstruct  $p(x)$  using Hermite blending functions. Thus  $p(x)$  can be written as:

$$p(x) = f_i H_1(x) + f_{i+1} H_2(x) + d_i H_3(x) + d_{i+1} H_4(x). \quad (4.3.5)$$

where  $H_i$  are the basis Hermite functions as defined in [4.1], and  $d_i, d_{i+1}$  are the derivatives of  $p(x_i)$  and  $p(x_{i+1})$  respectively. The Hermite basis functions find their application in geometric modelling and have been chosen here since these types of splines are known to successfully predict motion trajectories in three-dimensional space, hence they are able to better estimate the travelling of wavefront.

The limitations of this method come with the smoothness of the collected data, which means that a large number of extended elements will fail to predict with accuracy, based solely on the convexity. However, the resolution improvement can still be significant [4.1].

It is possible by using a piecewise function, formed by a set of polynomials to



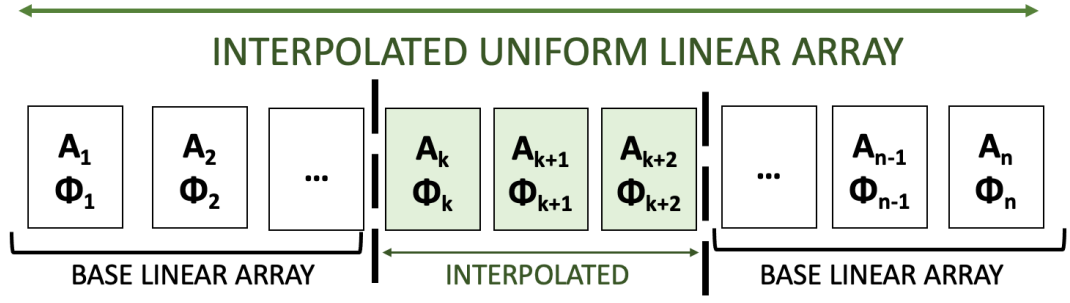


Figure 4.7: Illustration of the interpolation method for predicting missing inter-array data for the improvement of detection accuracy.

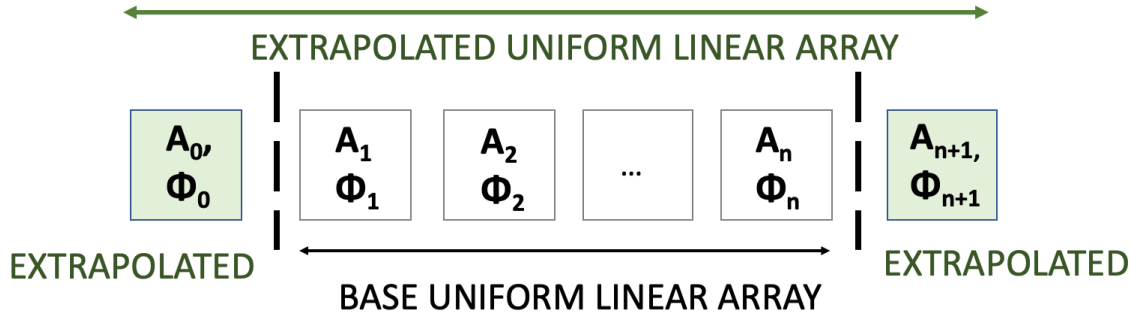


Figure 4.8: Illustration of the extrapolation method for estimating extra-array data for the enhancement of antenna aperture

estimate the previous and next element data values:  $e^{-j(\phi_{t0}+\phi_{r0})}$  and  $e^{-j(\phi_{N+1}+\phi_{M+1})}$  for the steering vectors. More information of the theory behind virtual arrays and MIMO radar can be found in Chapters 2 and 3. In this approach of estimating the element data, a shape-preserving interpolation and extrapolation methods are used. The data points are estimated with a piece-wise cubic function for the adjacent values at the grid points. This is illustrated for the interpolation method in Figure 4.7 and in Figure 4.8 for the extrapolation method.

These are related to the receiver spacing and position for the physical array. In order to efficiently predict the values for the grid points, the condition of smoothness must be met between two points.  $C^1$  is the property which assumes continuity of the tangent vector of two such points, so that the derivative and integral between said points are continuous or monotonic [4.2].

The limitations of this method come with the smoothness of the collected radar data. A large number of extended elements will fail to predict accurately, based solely on a reduced data sample. However, for a large-enough array size, the res-

Table 4.3: Baseline ULA and Extended Receiver Comparison

Base ULA Size	Base $\Theta_{3dB}$ (°)	Extended ULA Size	Interpolated/Extrapolated $\Theta_{3dB}$ (°)
4	30.00	6	19.47
8	14.48	12	9.59
12	9.59	16	7.18
16	7.18	24	4.78
32	3.58	44	2.61

olution improvement of the extrapolated array can be significant [4.1]. A possible explanation for this behaviour is that the angular resolution of the radar can be determined by using the Rayleigh criterion which is based on the number of elements  $N$ . For example, when considering  $\lambda/2$  receiver element spacing, the angular resolution can be defined in degrees as  $\Theta_{3dB} = \sin^{-1}(2/N)$  [1.4]. Table 4.3 shows resolution predictions for interpolate/extrapolated ULAs.

### 4.3.2 Practical Implementation of Interpolation and Extrapolation for Radar System

Since the signal processing methods have been described, some results are presented here for the practical implementation of these methods and assessing their performance. In order to highlight the benefits of data interpolation and extrapolation at the radar receiver the hardware setup is used in a similar manner to the experiments presented in Chapter 3. The measurements have been carried out using the 24 GHz frequency-modulated continuous wave (FMCW)  $2 \times 4$  MIMO radar system with 1.5 GHz SIW transmitter and receiver antennas. The characteristics of this radar have been previously described in Chapter 3 of this thesis, together with the antenna design principles as well as the resulting range resolution and field-of-view capability.

### 4.3.3 Measurements with extrapolation

Measurements have been carried out in a controlled anechoic environment. A picture with the extrapolation measurement front-end setup can be observed in Figure 4.9(a). Two targets of size 30 cm x 40 cm with an angular spacing of  $25^\circ$  between

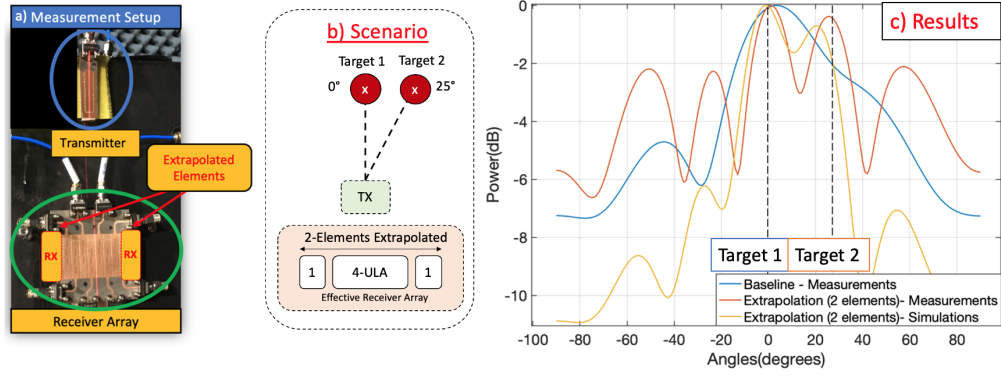


Figure 4.9: Real, simulated and measured angular target estimates considering a SIMO (1TX4RX) radar configuration which identifies two targets at:  $0^\circ$  and  $25^\circ$  (with a theoretical resolution of  $30^\circ$ ) at 24 GHz, with two extrapolants using a piecewise cubic extrapolation function: (a) SIW Transmitter and receiver array with highlighted extrapolation elements, (b) front-end configuration and illustration of the radar scenario, (c) simulations and measurements comparing the baseline and extrapolated cases.

them have been placed at 2 meters in front of a SIMO 1TX-4RX configuration as shown in Figure 4.9(b). The minimum separation which can be distinguished is  $30^\circ$ . With regards to the sensor calibrations, corrections have been applied to ensure phase balance of the electrical length of the antenna front-end using a known calibration target. A relative phase factor correction,  $\Delta_\phi$ , has been applied to each of the receiver channels. The SIMO results of the simulations and measurements for the extrapolation trials can be seen in Figure 4.9(c).

A comparison of different interpolation/extrapolation functions applied for the SIMO measurement data can be observed in Figure 4.10. In particular, the following extrapolation methods have been used: linear, nearest, next and previous (a variant of linear extrapolation), piecewise cubic extrapolation (pchip, used in this work, see Figure 4.9(c)), modified Akima (makima) and spline extrapolation. A brief comparison is made here:

- ‘Nearest’, ‘next’ and ‘previous’ extrapolation functions are the fastest. They also do not require the function data to be monotonous.
- ‘Linear’ extrapolation entails smooth continuous data while taking more time than the previous methods.
- ‘Pchip’ extrapolation demands more time and computational space than ‘linear’, however it provides better smoothing than previous methods [4.1].

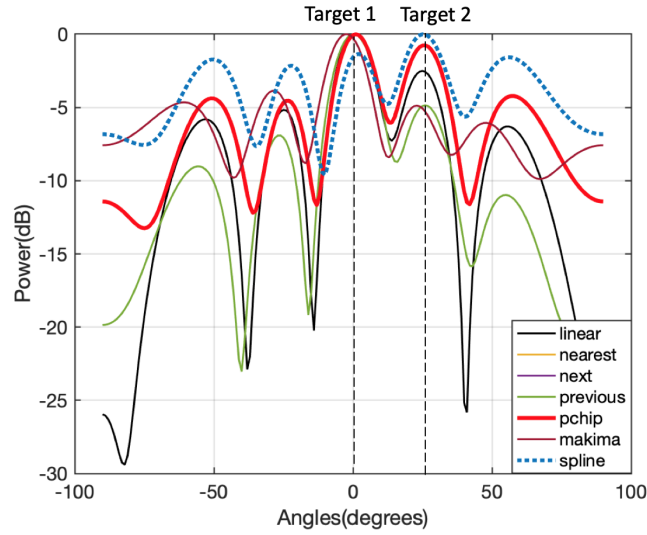


Figure 4.10: Trial runs on 1x4 SIMO measurement data comparing discontinuous extrapolation functions (nearest, next and previous) and continuous extrapolation functions (linear, pchip, makima and spline) with pchip rendering an optimal response for target detection and resolution.

- ‘Spline’ and ‘makima’ are the most computationally expensive, however they account for data which contains overshoots.

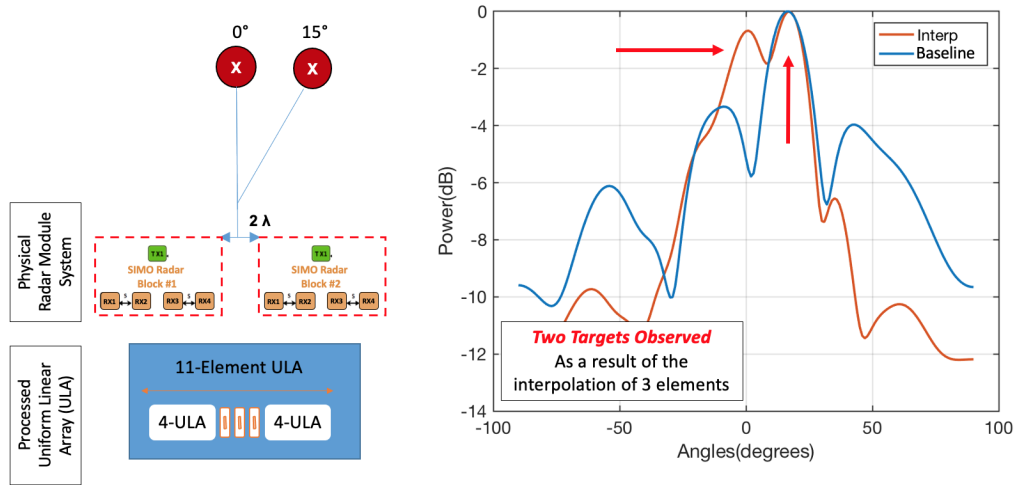


Figure 4.11: Simulated and measured interpolated angular target estimates considering a MIMO (2TX4RX) radar configuration which identifies two targets at: 0° and 15° at 24 GHz, showing a baseline and results for three interpolants using a linear extrapolation function.

### 4.3.4 Measurements with the Interpolation Method

Measurements and simulations have also been carried out and results are available for both MIMO 2TX-4RX (see Figure 4.11) and MIMO 6TX-12RX (see Figure 4.12) using the same radar architecture as before but taking multiple images of the same scene and displacing the radar module with each measurement, similar to how synthetic aperture radar (SAR) is formed. The results for the 2TX-4RX case (Figure 4.11) shows that even three interpolants can increase accuracy with target detection, due to the extended aperture size of the receiver antenna array mimicked by the processed elements using the interpolation method as previously described in the first sections of the chapter. In this case the SIMO radar configuration is measured at a distance of  $2\lambda$  apart from each trial and then the data is processed together with the interpolation function. The second case looks at 3 views of a 2TX 4RX antenna configuration and it can be seen that from the interpolation method, a 20% improvement is possible in antenna aperture size. The targets are now seen with better accuracy, and the half power beamwidth in Figure 4.12 is thinner for the interpolated 32-element ULA than the measured 24-element ULA.

Table 4.4 shows a summary of the rest of the measurements for interpolation and extrapolation. With these results we are able to see that with higher number of elements, it is possible to have more errors appearing if the configured antenna

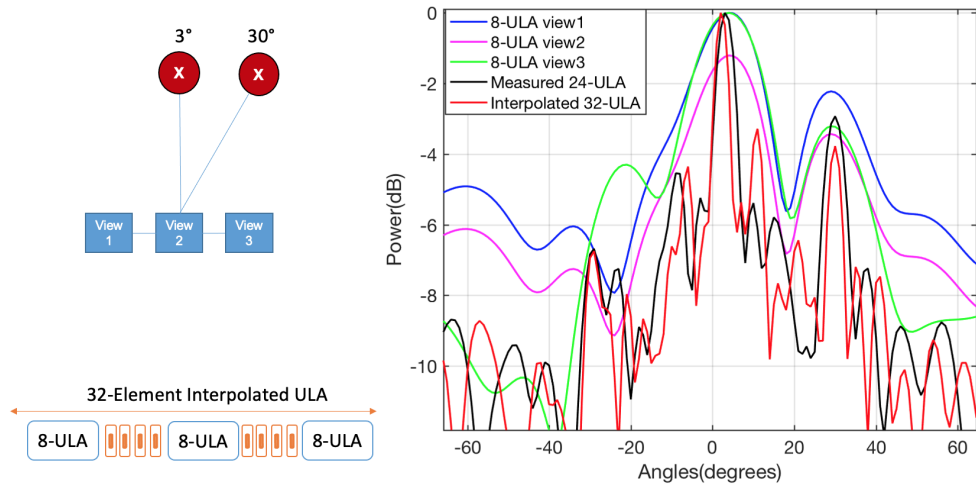


Figure 4.12: Simulated and measured interpolated angular target estimates considering a MIMO (6TX12RX) radar configuration which identifies two targets at:  $3^\circ$  and  $30^\circ$  at 24 GHz, with eight interpolants using a linear extrapolation function.

Number of Targets	Number of Real Elements (ULA Size)	Interpolants Between Modules	Total Number of Processed Elements	Half-Power Beamwidth No Interpolation (Sims./Meas.)	Half-Power Beamwidth Total Array (Sims./Meas.)	Detection By Interpolation
1 Target	24	1	26	24 ULA - 5.8°/5.6°	26 ULA - 5.2°/5°	Yes
	24	2	28	24 ULA - 5.8°/5.6°	28 ULA - 4.8°/4.7°	Yes
	24	4	32	24 ULA - 5.8°/5.6°	32 ULA - 4.6°/4.5°	Yes
2 Targets	24	1	26	24 ULA - 5.8°/ 6.3°	26 ULA - 5.3°/5.6°	Yes - Errors
	24	2	28	24 ULA - 5.8°/ 6.3°	28 ULA - 6.3°/ 5.2°	No
	24	4	32	24 ULA - 5.8°/ 6.3°	32 ULA - 4.3° / 4.1°	Yes
1 Target	32	1	35	32 ULA - 4.3°/4.2°	35 ULA - 3.98°/3.89°	Yes
	32	2	38	32 ULA - 4.3°/4.2°	38 ULA - 3.52°/3.5°	Yes
	32	4	44	32 ULA - 4.3°/4.2°	44 ULA - 3.0°/2.9°	Yes
2 Targets	32	1	35	32 ULA - 4.3°/4.4°	35 ULA - 3.8°/4°	Yes - Errors
	32	2	38	32 ULA - 4.3°/4.7°	38 ULA - 3.4°/4°	No
	32	4	44	32 ULA - 4.3°/ 4.7°	44 ULA - 3°/3°	Yes

Table 4.4: Summary of interpolated and extrapolated measurements for various antenna element sizes

array is not able to model an adequate SLL, as in the case of two targets with 2 interpolated array elements in comparison to 4 interpolated elements which are able to distinguish the targets.

## 4.4 Highly Separated Radar Systems for Improved Target Illumination

### 4.4.1 Background

Another concept discussed in this thesis is the scenario where antennas for the radar are placed at a certain distance apart, with a large separation between them. This introduces the concept of highly separated antennas for radar and will behave in a different manner than what we have seen so far in the previous chapters. According to [3.41], MIMO radar can be seen as a sort of multi-static radar system. While it is true that position deviation from the uniform linear array (ULA) will alter side lobes, it can be the case that with non-coherent processing, the radar cross section (RCS) variation for a target can offer increases diversity gain [3.41].

Hence we can see an angular resolution improvement due to reducing the coupling of collocated radars. There are several algorithms which offer improved angular resolution at the expense of either computational cost or detection error. A method of

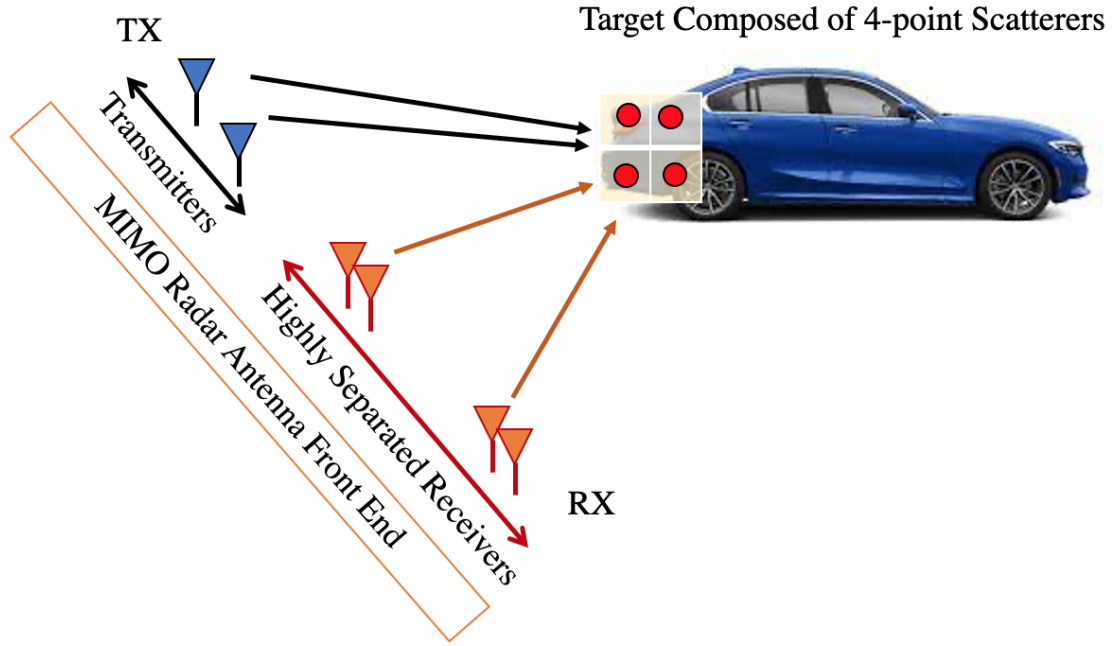


Figure 4.13: Illustration of highly separated radar detection showing 4 point scatters.

doubling the total antenna aperture is to space receiver elements at spacing, which reduces the field of view but increases antenna aperture. In this case, multiple radars have to be used to cover the radar field of view. When using multiplication and highly separated radar modules, target accuracy is significantly improved when compared to classic MIMO radar. This concept has been applied with the Power+ algorithm [2.67] which uses this multiplication smoothing function at multiple steering angles of the transmitted beam.

The concept of spatial multiplexing which is used in MIMO radar is actually setting up a multidimensional space for the signals which are either transmitted or received at the radar antennas [3.41]. Several arrays, such as adaptive arrays and phased arrays optimise the processing of signals in order to maximise the signal-to-interference ratio [3.41]. From a modelling point of view, when spacing antennas at large separation, the target is seen rather as an extended target, different than a point modelled with no spatial properties, as seen with co-located antenna systems. However, each of the antenna configurations, both collocated and widely separated have their advantages and disadvantages. Some of these are:

- With collocated MIMO antennas, the processing gain (related to the bandwidth) can be compensated with gain in time with an uniform illumination.

On the other hand, complex targets with a large number of scatters have a complex RCS which is dependent on the angle.

- For a target which has a complex geometry, positioning the MIMO elements can lead to diversity gain, quantified in improved SNR levels.
- The addition of MIMO radar in combination with widely separated antennas offers improved angular resolution due to the larger antenna aperture formed by receiver antenna elements spaced at a larger distance.
- MIMO radar systems in combination with phased arrays can provide diversity gain for direction finding applications [3.41].

In order to verify if the elements are uncorrelated, [3.41] presents how this property can be verified. Let us assume a model formed of four antenna elements with two transmitters having coordinates  $(x_{ta}, y_{ta})$  and  $(x_{tb}, y_{tb})$  for the receiver elements  $(x_{rc}, y_{rc})$  and  $(x_{rd}, y_{rd})$ . In addition, let us define  $D_x$  and  $D_y$  as the target dimensions in the x and y planes respectively while  $d(T_a, X_0)$ ,  $d(T_b, X_0)$ ,  $d(R_c, X_0)$ ,  $d(R_d, X_0)$  are the distances between target and the transmitter and receiver elements. It is expected that the channel matrix will have uncorrelated elements if and only if the following inequalities apply:

$$\begin{aligned}
 \frac{x_{ta}}{d(T_a, X_0)} - \frac{x_{tb}}{d(T_b, X_0)} &\ll \frac{\lambda}{D_x} \\
 \frac{y_{ta}}{d(T_a, X_0)} - \frac{y_{tb}}{d(T_b, X_0)} &\ll \frac{\lambda}{D_y} \\
 \frac{x_{tc}}{d(R_c, X_0)} - \frac{x_{td}}{d(R_d, X_0)} &\ll \frac{\lambda}{D_x} \\
 \frac{y_{tc}}{d(R_c, X_0)} - \frac{y_{td}}{d(R_d, X_0)} &\ll \frac{\lambda}{D_y}
 \end{aligned} \tag{4.4.1}$$

where a,b are the indices of the transmitters and c,d are the indices of the receiver elements. This concept is also illustrated in Figure 4.13. As an example, we are able to define a target at  $d = 10^4\lambda$  with dimensions  $D = 10\lambda$ . At 24 GHz, this means that we have a 10 cm<sup>2</sup> target located 12.5 meters. In this case, the transmitters and receivers have to be distanced at  $10^3\lambda$  for Eq. 4.4.1 to be satisfied. Therefore, the size of the radar front-end in the automotive scenario becomes 1.25 m in size, which



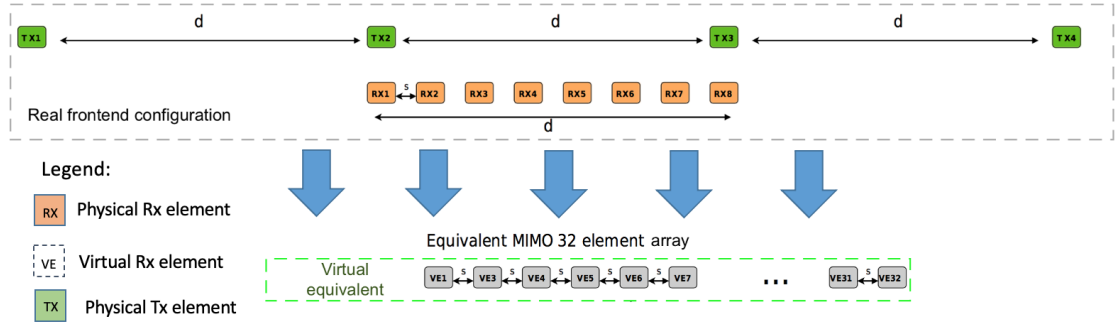


Figure 4.14: Highly separated antenna configurations showing the spacing of the transmitters and receiver antennas with 10cm and 45cm apart.

is less than the size of the bumper in most situations. Hence, the radar designer is able to play with the antenna elements to obtain uncorrelated elements and ripe the benefits as further mentioned at the beginning of this sub-section.

#### 4.4.2 Highly Separated Radar

For highly separated radars, a trial has been carried out to prove the performance claims as highlighted in the theory section of this chapter. A similar radar architecture to the multiplication method has been used in order to compose a 32-element equivalent antenna system (Figure 4.14 for reference). The measurements for the 45 cm and 10 cm inter-element spacing can be seen in Figure 4.15, which highlights these two configurations. The case where the elements are spaced at 45 cm shows an immediate advantage, where the target is illuminated from a wider perspective, thus increasing spatial gain, showing the benefits of MIMO antennas now with widely separated transmitter elements.

A target with complex RCS can be better illuminated with the widely separated antennas and this response can be improved with the use of multiplication. Combining the multiplication and highly separated radar will complement the weakness of each and improve radar response. The methods is illustrated in Figure 4.16. The measurement in Figure 4.17 shows the illumination of one target, the diversity gain can be clearly identified for the separation of the MIMO base detection and MIMO radar with separation at 45 cm plus multiplication, with the later having a better side-lobe level response, at the expense of beamwidth.

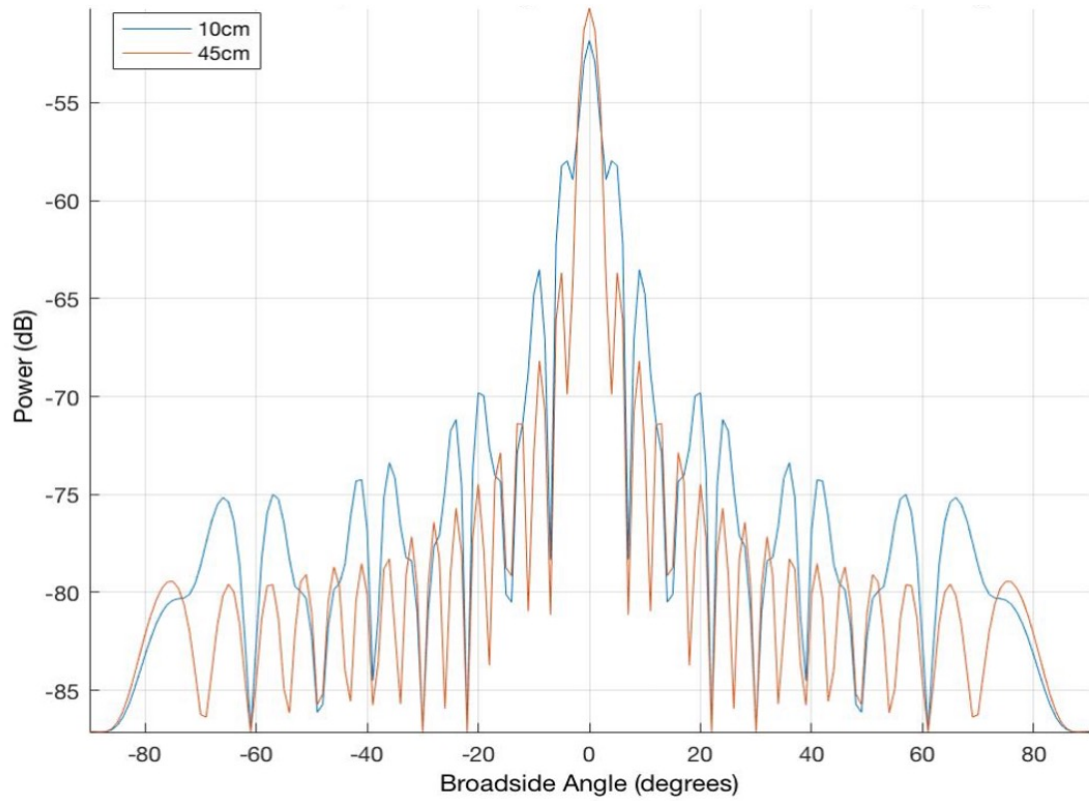


Figure 4.15: Results of highly separated radar measurements showing 10 cm and 45 cm separation (without normalisation).

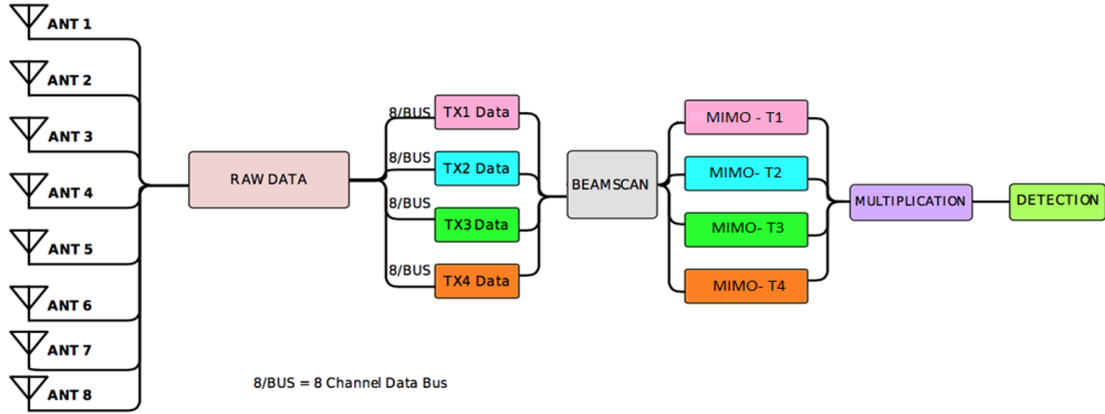


Figure 4.16: Highly separated radar signal processing chain showing the data acquisition of each radar and post-processing for complete target detection.

In order to see the benefits of radar multiplication and highly separated radar for multiple targets these two methods have been combined into a new type of detection and processing which improves the response of the radar. The delay-and-sum algorithm can be applied to individual SIMO blocks. When this data is combined, the MIMO data sets can be sampled at different times (i.e. time T1,

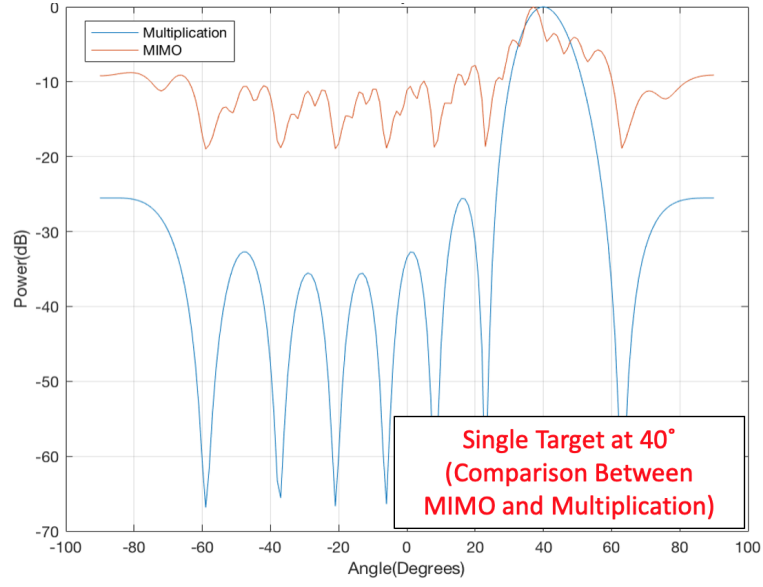


Figure 4.17: Highly separated radar target detection of one target with multiplication.

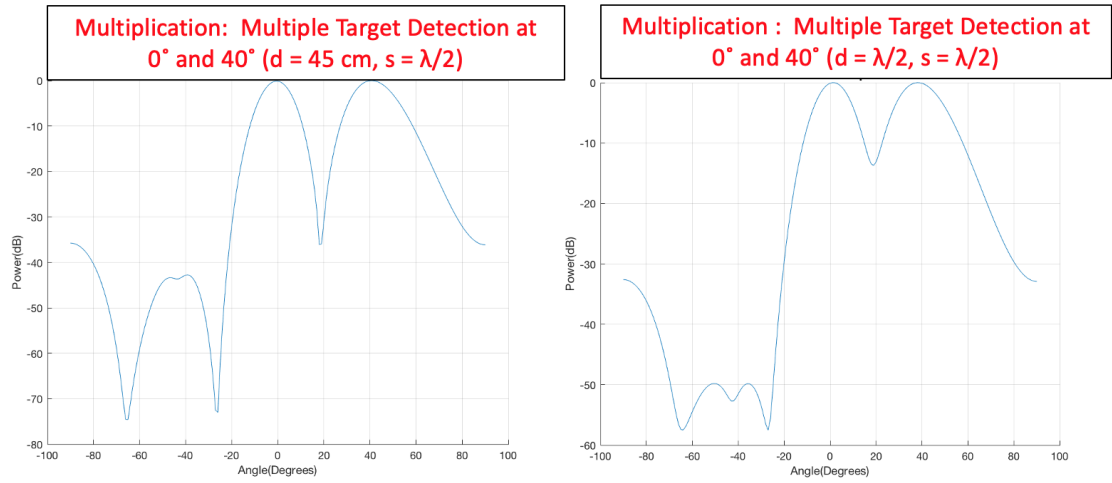


Figure 4.18: Highly separated antenna configurations measurements showing two scenarios with antennas separated at either  $0.5\lambda$  or  $45\text{cm}$  apart, showing the benefit of using highly separated radar antennas.

time  $T_2, \dots$ , time  $T_4$  ). This is the same principle applied for synthetic aperture imaging, where the antenna aperture is enlarged by taking multiple samples of the data at different points in the time and spatial domain.

In Figure 4.18, we analyse measurements of highly separated radars for two targets using multiplication. Since the separation between radar modules is now bigger ( $d = 45\text{ cm}$ ), the two targets can be noticed easily in comparison with the half-

lambda case ( $d = 0.5\lambda$ ) when considering the multiplication algorithm. Accuracy for the separated case ( $d = 45$  cm), is improved when compared to classic MIMO. For the case of two targets at  $0^\circ$  (broadside) and  $40^\circ$ , the MIMO radar modules can identify the two targets with good accuracy. This considers more classic MIMO radar signal processing approaches. Accuracy is reduced for the off broadside target, and for the highly separated radar case; i.e.  $d = 45$  cm.

## **4.5 Conclusions and future work**

In this chapter, four methods have been presented for enhancing target detection for automotive radar sensing. The methods demonstrated that with the help of interpolation and extrapolation, the effective aperture of the receiver antenna array can be improved or enlarged, which in turn relates to a better detection of the target due to the narrowing of the receiver antenna beam pattern. At the same time, the spectral smoothing multiplication function is able to improve the target response by narrowing the main lobe of the receiver and suppressing the side-lobes. This overall improves the accuracy of the detection, however, that does not improve the aperture length, which is related to the physical or virtual size of the antenna. On the other hand, highly separated antenna arrays are improving the decorrelation between antenna elements, and thus providing a better illumination of the targets provided that the space between antenna elements and the size of the targets satisfy some conditions outlined in detail at the beginning of the chapter. In Chapter 5, compressive sensing in conjunction with non-uniform sparse antenna arrays will also be discussed as a method for an improved radar detection due to the use of a wider aperture length and sparse processing.

## **4.6 Contributions by the candidate**

In this chapter, the candidate has developed the idea of multiplication for radar detection and has related to spectral physics to find a mathematical expression of the overall improvement, especially for an FMCW radar using MIMO SIW antennas. The candidate has also implemented the concepts of interpolation and extrapolation

in radar detection for FMCW MIMO in the angular domain, using the same template with signal reconstruction. In addition, simulations and measurements have been carried out by him to prove the theoretical improvements. For the extrapolation measurements, the candidate has identified several extrapolation techniques which have been compared. In the same manner, the highly separated radar concept has been probed and measured by the candidate within the anechoic chamber. All of the processing methods have been developed by him in Matlab.

# Chapter 5

## Compressed Sensing for High Resolution Radar Detection

### 5.1 Introduction

In radar detection the number of total possible targets outnumbers the number of reflections that the radar receives back from a detection, even for higher resolution sensors. Hence, the amount of information of the signal is much lower than the number of resolution cells or the number of samples. Therefore radar systems typically solve a compressible problem, be it in range, angle or velocity. Therefore radars resolve sparse problems when it comes down to minimal information offered by the environment. By solving this sparsity problem, undersampling techniques such as compressive sensing (CS) allows robust sampling beyond the Nyquist-Shannon limit [1.1]. Radar signals may be sparse in each of its dimensions. Hence, the signal can also be sparse in the angular domain, or it can be sparse in the frequency domain. When we refer to sparsity in the following sections, we will refer to sparsity in the angular domain. To apply CS it is important to note that it is aperiodic and random. It was shown that only 20% of the resolution bandwidth was enough to accurately recover targets. CS is very popular in direction of arrival (DOA) estimation [5.1].

Accurate localisation of targets is important for collision avoidance applications and the industry is seeking to obtain a high resolution radar system which is able to generate 4D data (x,y,z and time) of the targets. This has been presented in detail in Chapter 2, showing the preliminary works undertaken to solve this solution. In

this chapter, the following concepts are introduced:

- compressive sensing for target detection using undersampling methods and image reconstruction.
- sparse non-uniform antenna array configurations tailored for compressive sensing algorithms.
- YALL1 algorithm for a versatile compressive sensing approach.

### 5.1.1 Motivation and goal

This chapter has the goal of demonstrating how compressive sensing is able to offer high resolution images with a few number of samples compared to classical beam-forming techniques. The chapter also presents the mechanics of one particular algorithm which is known to be used in other compressive sensing application. Moreover, the motivation of this work is to prototype compressive sensing detection with the FMCW radar equipped with SIW antennas, and see the performance improvement in cases we have analyzed in previous chapters.

While signal to noise (SNR) ratios need to be above a certain threshold to detect targets, another challenge is to be able to discriminate between closely spaced targets, especially in an environment where clutter is present. While MIMO systems provide enhanced performance, Nyquist spatial sampling is not always needed for enhanced radar performance [5.2]. The number of transmitters  $M$ , together with the number of receivers  $N$ , form the virtual array of the radar, also termed the virtual ULA. This virtual ULA needs to scale linearly with the number of elements due to the Nyquist rate, hence the resolution of the radar is limited by the array aperture length [5.2]. In a sparse array architecture employing sub-Nyquist rates, it is possible to apply reconstruction to achieve a similar goal in comparison to a full ULA, however, the antenna is sparse.

## 5.2 Compressive Sensing (CS)

Compressive sensing (CS or compressed sensing or sparse sensing) represents a mathematical framework for measuring signals with reduced sampling or compressing them. However, in this thesis, when referring to sparsity, it would refer only to

the sparsity of the antenna positions, due to the design of the non-uniform antenna array. The underlying principles behind compressive sensing can be summarised in the following points:

- *Sparsity*: Real-world signals can reveal essential information in small amounts [5.3]. It is therefore possible by acquiring basic components of the signal to retrieve a basis for the original signal with far fewer measurements.
- *Measurement scheme*: By employing a random measurement scheme it is possible to obtain samples that allow accurate reconstruction. Typically, an approach which finds distinct samples helps identifying the basis faster. [5.3].
- *Reconstruction algorithm*: Good approximations of the original signal are going to be dependent on the reconstruction procedure and the convergence criterion of the algorithm. [5.3].

In this context, compressive sensing is able to offer reconstruction based on reduced number of samples. The above principles are critical to the successful reconstruction of the signal since each contribute equally to the end result. For example, poor signal compression will lead to ineffective measurement of the signal, hence the reconstruction algorithm is prone to fail signal reconstruction. On the other hand, if reconstruction algorithms are too slow and costly or if results are inaccurate, then the reconstruction will again be ineffective.

### 5.2.1 CS in Automotive Radar

While hardware developments in automotive radar progressed in more recent years, the point of interest on millimetre wave radar systems has been directed towards digital technologies [1.1]. Although analogue systems are still used today, with a combination of both analogue and digital components, the focus on more recent research has been directed towards digital technologies [1.1]. Topics such have included digital modulated radar, compressed sensing, radar networks, grid mapping and automotive synthetic aperture radar (SAR) [1.1]. There has been significant development in compressive sensing for automotive radar since its adoption has reduced sampling requirements and data rates [5.1], especially since higher bandwidth radar sensors require more powerful hardware. Recently, innovative proof-of-concept systems have been designed and presented in the literature. Some of the early works



present MIMO radar systems that show improvement compared to the FFT method [5.4], even better than adaptive subspace search methods such as Multiple Signal Classification (MUSIC). The work presented in [5.4] describes an X-band radar system which is formed of 12-folded dipole antennas separated at  $\lambda/2$  and the outer receive channels separated at  $0.25\lambda$  from the transmitters. Although it is not specified which type of reconstruction is used in [5.4], the targets separated at  $6.4^\circ$  in the angular domain are being easily detected with CS, clearly surpassing the performance of the FFT and MUSIC angle of arrival (DoA) estimation. Several CS algorithms have been developed since then. In [5.5], the focus is directed towards identifying the CS algorithm which can give the best accuracy by minimising the RMS of the detected signal, coupled with reducing SLL. Although the azimuth resolution is not specified for the set of measurements, the half-power beamwidth (HPBW) of the antenna array configuration is less than  $10^\circ$ .

The methods presented in [5.5] confirm that increased accuracy requirements for the algorithm implies more complex computations, and therefore increased detection time. It can be seen that orthogonal matching pursuit (OMP) requires less computational time than NESTA (a shorthand notation for Nesterov's algorithm). However, NESTA benefits from improved reconstruction and could be used for static scenarios or with slow moving targets. The same research group has compared the same algorithms with another radar platform in [2.21], where the CS algorithms are compared for angular resolution and several algorithms are used for detection of the best sparse antenna configuration. In this later work, tapering is applied to improve SLL for detection and simulated annealing is used to vary the search pattern of the antenna configuration. This investigation shows results the side-lobe levels versus the HPBW. A trade off is therefore needed between these two performance metrics, as large aperture antenna arrays using a sparse configuration can suffer from high side lobe levels. The work also shows that the probability of detection is lower for targets that are closer than the azimuth resolution limit. Target detection for sparse antenna configurations is better than ULAs as can be seen with the results shown in [2.21]. The OMP algorithm can for example detect targets separated at  $13^\circ$  for an ULA while only separated of  $7.7^\circ$  by a sparse array. The improvement is consistent with the other algorithms, with Focal Underdetermined System Solver (FOCUSS)

reaching almost a two-fold improvement. Maintaining a good FOV is also very important, hence the FoV has been measured to be  $\pm 60^\circ$  with an  $\text{SNR} = 5\text{dB}$ . On the other hand, other methods for improving angular resolution exist. The authors in [3.39] obtain improved target detection by scanning the medium with the help of a beam switching network and together with signal smoothing of each detection, the combined view of the detection is further improved. This is done with the use of a beampattern multiplication method as highlighted in Chapter 3 of the thesis.

It can be seen from Table 5.1 that there has been a sustained effort for improving angular resolution and range resolution, especially with higher number of antenna elements being present. This shows that the academia and industry is seeking for a compact modular solution which has a high number of elements [1.2], which can be either high performance or cost optimised. As it can be seen from the table, the most effective solutions are the ones which incorporate sparse array design, while ULA type of approaches may not experience the same level of performance. It is desired that modular radar systems be manufactured as a chip solution, which incorporates the power management, antenna and signal processing all on the same chip, leaving the possibility of adding machine learning at a later stage. From Table 5.1, it is clear that the higher the operating frequency, the better for the radar since the percentage bandwidth also increases the range resolution of the system, as can be seen in [5.6]. However, the issue at the moment is that these systems tend to be bulky and costly, while the industry might want to choose a different solution such as the one found in [5.7], which offers similar or better performance. The targets are obtained by applying the FFT, and while this allows fast detection due to the size of the array, it can also result in a loss of angular resolution. There are other beamforming methods which will result in a better detection, however, the speed of such detection needs to be optimal, hence new digital beamforming methods need to be optimally configured for larger array sizes. The work presented in [5.8] and summarised in Table 5.1 suggests that sparse MIMO array design can increase angular resolution, while uniform MIMO and ULA solutions may achieve less performance in terms of angular resolution.

### 5.2.2 Problem formulation

How does compressive sensing allow reconstruction with a reduced number of samples? Let us assume that we are reconstructing a complex signal  $\mathbf{x}$  from a linear number of measurements such that:

$$\mathbf{y} = \mathbf{A}\mathbf{x}, \mathbf{y} \in \mathbb{C}^m, \mathbf{A} \in \mathbb{C}^{m \times N} \quad (5.2.1)$$

where  $\mathbf{A}$  is the measurement matrix,  $\mathbf{y}$  is the measured signal of size  $m$ , where  $m \ll N$ , i.e. the number of sparse measurements ( $m$ ) are far less than the total number of measurements ( $N$ ). This process is called *encoding*, while the process of obtaining  $\mathbf{x}$  is called *decoding* [5.9], by solving the set of linear of equations which derive from Eq. 5.2.1:

$$\mathbf{x} = \mathbf{A}^{-1}\mathbf{y} \quad (5.2.2)$$

This complements the fact that  $\mathbf{x}$  is known before hand to be  $k$ -sparse, where  $k$  is the sparsity of the signal. A vector is  $k$ -sparse if it has at most  $k$  non-zero entries. When looking for the solution, it is assumed that one would look for the sparsest signal available. Mathematically, it would translated into the following form:

$$\min \|\mathbf{x}\|_0 : \mathbf{y} = \mathbf{A}\mathbf{x} \quad (5.2.3)$$

where  $\|\mathbf{x}\|_0$  represents the the non-zero entries from  $\mathbf{x}$ . This problem is actually computationally hard since going through all the possible solutions is too complex, and hence not practical. This form represents the " $l_0$ -norm". An alternative practical solution is to choose the nearest approximation to the  $l_0$ -norm, which is the " $l_1$ -norm" [5.9]:

$$\min \|\mathbf{x}\|_1 : \mathbf{y} = \mathbf{A}\mathbf{x} \quad (5.2.4)$$

This approach is also termed basis pursuit. A key result for compressive sensing is that if the measurement matrix  $\mathbf{A}$  satisfies the Restricted Isometry Property (RIP) with high probability, then the original signal  $\mathbf{x}$  can be reconstructed. The property takes the following form [5.3]:

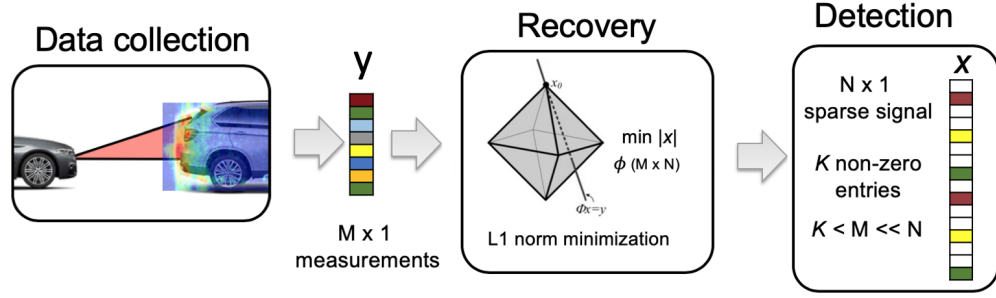


Figure 5.1: Diagram showing the steps taken to apply CS reconstruction.

$$m \geq Ck \ln(N/k) \quad (5.2.5)$$

where  $C$  is a constant. Nyquist sampling rates are thus not required in this case, significantly reducing the need for extensive processing of the signal [5.3]. A more intuitive answer is that CS gathers only the essential information from a sparse signal, hence it reduces the number of measurements altogether. There are two basic needs for compressive sensing: recoverability and stability. With recoverability, the point of interest is the types of measurements and their number to extract a sufficiently sparse signal. Stability refers to the robustness of the algorithm over time and noise variation.

While CS seems like an all encompassing solution to problems requiring Nyquist sampling, sparse-like signals are only half of the battle. Measurement matrix design and reconstruction algorithms represent the second problem to overcome. Greedy algorithms and iterative algorithms that have to converge to a certain solution often need a right set of initialisation parameters, hence their design is also a considerable challenge [5.3]. An illustration of the CS reconstruction steps is shown in Figure 5.1, showing data acquisition, sparse data formation and reconstruction using  $l_1$  minimisation.

With a known measurement  $y$  of high sparsity, it can be assumed that a reconstruction algorithm will look at the sparsest solution for the measurement

Table 5.1  
State-of-the-Art Radar System Comparison as Reported in the Literature

Automotive Radar (Year)	Carrier Frequency (GHz)	Target Estimate Algorithm	Receiver Array Architecture	Antenna Type	Equivalent Receiver Array (ERA)	Planar	Receiver Percentage Bandwidth	Range Resolution (cm)	Angular Resolution (°)
[5.4] (2011)	12	CS	Uniform MIMO	Microstrip Patch	18 (= 2×9)	Yes	16%	9.3	6.3
[2.21] (2019)	76	CS (OMP/ SPGL1/ FOCUSS)	ULA	Microstrip Patch	12 (= 3×4)	Yes	1.3%	15	5.5
[5.12] (2019)	76.5	CS (IMAT)	Sparse Array	Microstrip Patch	32 (= 4×8)	Yes	2.62%	7.5	2.6
[5.6] (2020)	300	CS (Elastic Net Algorithm)	Sparse by Single element (with Mechanical Movement in Time)	Horn Antenna	5 TX-RX channels	No	6.2%	0.083	1
[5.8](2022)	24	CS (YALL1)	MIMO Sparse	SIW	32 (= 4×8)	Yes	6.25%	10	2

### 5.2.3 Application of CS to Radar

CS radars have been introduced in the 2000's with the underlying mathematical model being understood [5.10], [5.11] and being developed in a wide range of applications. Radar detection requires robustness and making sure the target is detected with an adequate SNR ratio and relatively low SLLs [5.11]. This allows for multiple applications like tracking or target recognition and classification. CS comes as a 'revolution' for radar science [5.11] since the high data rates of traditional radar processing is now significantly reduced with CS, which means less power consumption and lower hardware costs. Moreover, it is possible to develop and design waveforms for accurate target recognition of sparse signals with sub-Nyquist sampling [5.11].

## 5.3 Your Algorithm for L1 (YALL1)

In the effort of finding the best CS algorithm, several options have been considered. Methods such as basis pursuit (BP) and orthogonal matching pursuit (OMP) show a quick convergence however, the algorithms are not always converging to the optimal solution [5.13]. Your Algorithm for L1 (YALL1) is a versatile solution which provides solutions to several  $l_1/l_2$ -norm problems. It is particular faster than other algorithms of its category according to [5.13]. Specifically the YALL1 algorithm solves  $l_1/l_2$  constrained non-negative regularization [5.3], which follows the following form:

$$\min_{\mathbf{x} \in \mathbf{R}^n} \|\mathbf{x}\|_1 \text{ s. t. } \|\mathbf{Ax} - \mathbf{y}\|_2 \leq \delta. \quad (5.3.1)$$

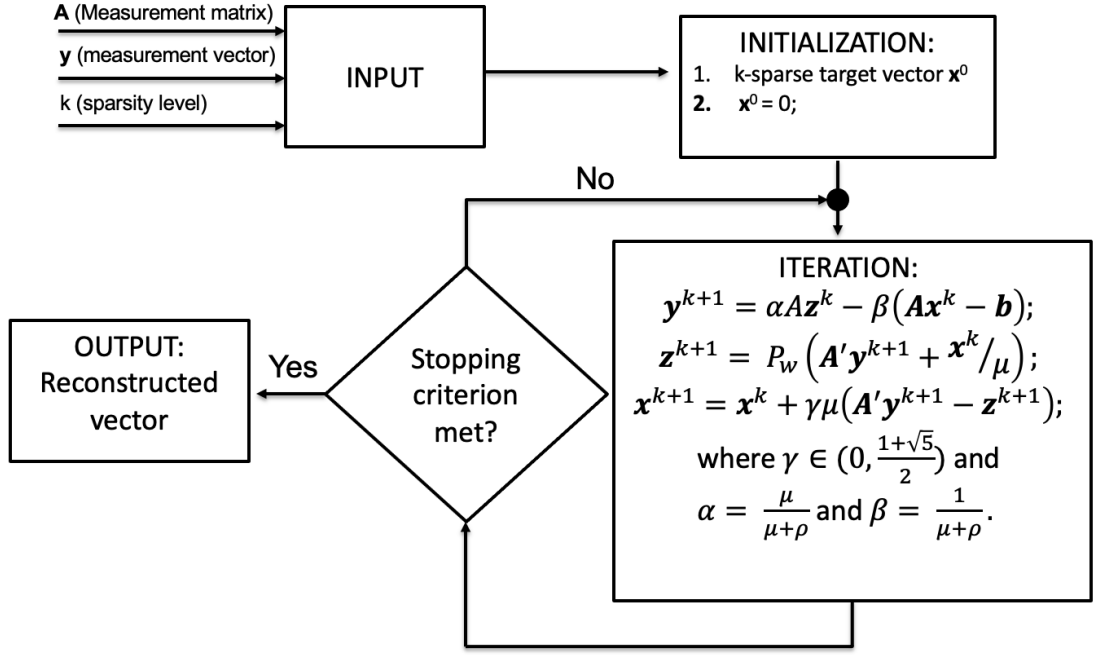


Figure 5.2: Your Algorithm for L1 (YALL1) procedure diagram.

where  $\delta$  is the detection threshold. Moreover  $x \geq 0$ , and  $\|n\| \leq \delta$ . Thus it is important that the threshold is not lowered too much so that the detection does not reach the noise levels and detect false targets.

Some studies focus on optimisation of  $l_1$  minimisation algorithms but also the sparsity analysis of real traffic scenarios, meaning the success and failure of sparse reconstruction can be known if contributing factors such as sparsity and SNR are considered [5.14, 5.15, 5.16]. This can be achieved with phase transition diagrams [5.14]. Similarly, it is reported that different antenna array configurations and sparse recovery algorithms are contributing elements to the failure or success of automotive radar detection. Sparsity-SNR transition diagrams are a good tool to discover the optimal detection parameters for the system as shown in [5.14].

YALL1 is a complex algorithm which necessitates a few iterative steps to find the reconstructed vector  $x$ . A flow diagram depicted in Figure 5.2 shows the procedures taken in the algorithmic process. As previously mentioned, there is a necessity of a matrix dictionary or a measurement matrix  $\mathbf{A}$ , which will use a set of measurement values found in  $\mathbf{y}$ . This signal  $\mathbf{y}$  needs to be  $k$ -sparse as mentioned in the previous sections of this chapter. It is important to initialise the target vector but also the

Table 5.2  
YALL1 Input Value Parameters

Parameter	Range	Description
$\rho$	(1e-2;1e-3)	This parameter assigns the L1/L2 model, usually with a positive value.
w	(0;1)	YALL1 can compute the conversion with non-uniform weights.
$\delta$	0.1	Noise level threshold
Print	[0,1,2]	Levels of printout
Maxit	[0:9999]	Maximum iterations
$\nu$	[0:1]	$> 0$ for L1/L1 model
$\rho$	1e-3	$> 0$ for L1/L1 model
nonneg	0	1 for non-negativity
$\mu$	set by user	penalty parameter

YALL1 parameters. These parameters refer to the tolerance, noise threshold, maximum number of iterations, mean, etc. These parameters have been summarised in Table 5.2. Setting the parameters for YALL1 is important since its convergence depends on setting adequate parameters, especially for initialisation. In the iteration phase of the algorithm as shown in Figure 5.2, the method for obtaining the reconstructed signal is by using minimised Lagrangian functions through an alternating minimisation procedure and update each multiplier after each sweep. This method is an iterative solution which solves a convex optimisation problem by dividing it into smaller pieces which are simpler to solve. The full pseudo-code of the algorithm can be found in Appendix A. A key step with YALL1 is appointing  $P_w$  which is a projection box onto the user defined  $B_w$  matrix. This can be found with an iterative method once the algorithm has been setup as can be found in Appendix 5.2.

## 5.4 Non-uniform sparse array

Recently, there has been a wide interest in sparse antenna array design for automotive radar systems due to the capability of obtaining a larger aperture and modelling SLL for better target detection [5.1, 2.21, 5.6, 5.12, 5.7]. While most works use different algorithms to obtain the optimal solution based on a set of constraints (antenna size, number of elements, desired SLL, etc.). It is reported in this thesis that a clear methodology of how to obtain an array with optimal design based on an heuristic technique is not currently present in automotive radar literature, most solutions implement algorithms to find the best antenna configuration.

## 5.5 Design of the non-uniform sparse array

In chapter 3, we have seen how the combination of a half-lambda spaced array and lambda spaced array can result in a non-uniform array, which we are able to use without the side-lobe level penalty and with better angular resolution. In this section we describe the method of design for the SIW non-uniform sparse array. In order to fully appreciate the number of possibilities in the array design process, Fig. 5.3 shows how an SIW receiver configuration for 4 elements can be used in a MIMO setting in order to make an enlarged array. Changing the element positions as to make an empty or full space determines the positions of the side lobes and the angular resolution. Therefore, by placing the physical receivers on several of the receiver positions for the 8-element array positions, we are able to choose the configuration with best angular resolution and SLL.

In the scenario depicted in Figure 5.3, the same MIMO antenna system with 2TX and 4RX is used to obtain a sparse antenna design by re-arranging the two antenna tiles (one being a physical antenna array, while the other is a virtual antenna array). Varying the spacing between the two antenna transmitters allows for creating a larger antenna aperture, which can enhance the total aperture length. However, this extra degree of freedom comes with the possibility of introducing grating lobes and raising the SLL, which is undesirable.

In fact, there are only a handful number of combinations which would result in the best angular resolution and SLL. These are obtained by searching through



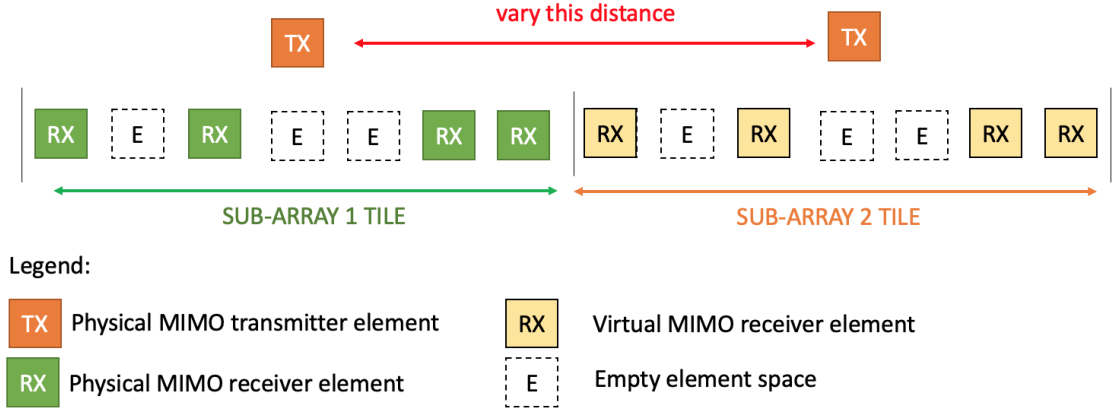


Figure 5.3: Template for obtaining a sparse array design for a 2TX 4RX receiver MIMO array, with elements spaced at  $\lambda/2$  inter-element spacing.

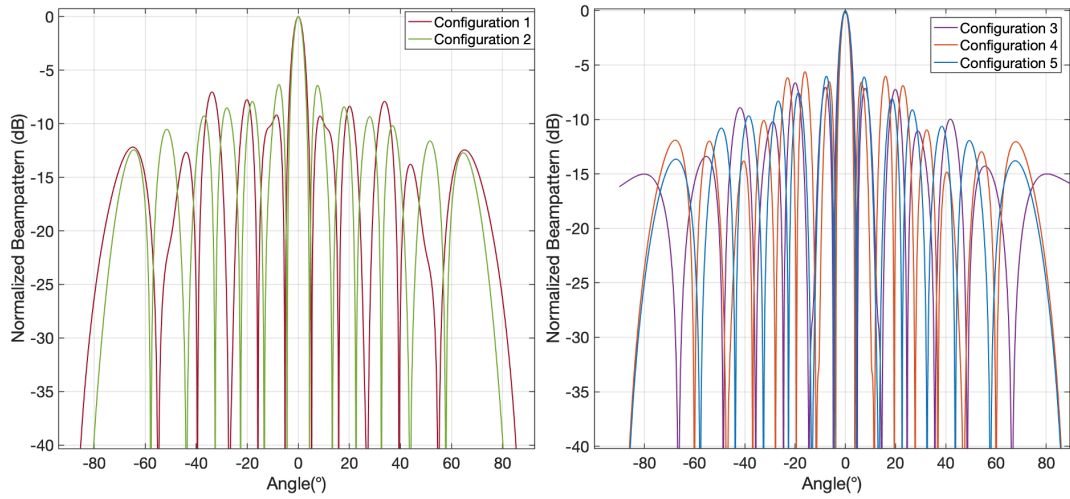


Figure 5.4: Comparison of measured beampatterns using the element beampattern multiplied with the array factor of the configurations found in Table 5.3.

all of the array factors of each configuration and deciding which has acceptable performance. In Table 5.3, the best five configurations are being presented for SLL and HPBW while Figure 5.4 two of the configurations found are presented in a side by side comparison and both the array geometry and the associated array factors are available for comparison. These configurations are gathered by first discovering the best solution for an individual antenna array tile, and then for different spacing between the antenna arrays.

The element positions are specified in terms of  $\lambda$  spacing, which is 1.25 cm at 24 GHz. It should be mentioned that there is no perfect solution even among the first five configurations, as some configurations offer improved HPBW while others

Table 5.3  
Comparison of Optimal Sparse Antenna Receiver Array Configurations

Config. Nr.	Inter-array spacing( $\lambda$ )	Element Positions ( $\lambda$ )	Angular Resolution( $^\circ$ )	SLL (dB)
1	7.5	-1.75, 0.25, 1.25, 1.75, 5.75, 7.75, 8.75, 9.25	3.6	-5.23
2	7	1.75, -1.25, 0.25, 1.25, -5.25, 5.75, 7.25, 8.25	4	-5.06
3	6.5	-1.75, -0.75, -0.25, 1.75, 4.75, 5.75, 6.25, 8.25	4	-6.17
4	6	-1.75, -1.25, 0.25, 1.25, 4.25, 4.75, 6.25, 7.25	4.4	-5.86
5	5.5	-1.75, 0.25, 1.25, 1.75, 3.75, 5.75, 6.75, 7.25	4.6	-5.00

better SLLs. Five antenna element patterns have been compared in Figure 5.4. The u-v response coordinate system helps even more to detect the side lobe levels when varying the antenna scanning angle and the representation of the simulated response for array configuration No. 1 (as seen in Table 5.3) can be observed in Figure 5.5. Measurements of the same can be observed in Figure 5.6, where a maximum SLL of -4.185 dB is reported.

### 5.5.1 Non-uniform antenna array scanning with angle

Even if the SLL is under a certain margin when scanning at different angles, it is possible to have two side-lobes in the azimuth or elevation plane by scanning the angle. Therefore, sweeping the  $\theta$  angle allows the detection of these lobes. Therefore, simulations and measurements of the scanning pattern have been carried out.

Figure 5.7 shows the SLL variation with scanning angle for all configurations highlighted in Table 5.3. This graph, shows the SLL variance with steering antenna angle, and it is observed how at a displacement of  $30^\circ$  the SLL can drop as low as -2.5 dB. This indicates that the antenna array cannot be used for beamsteering in certain cases, as the target detection may see false targets caused by the grating

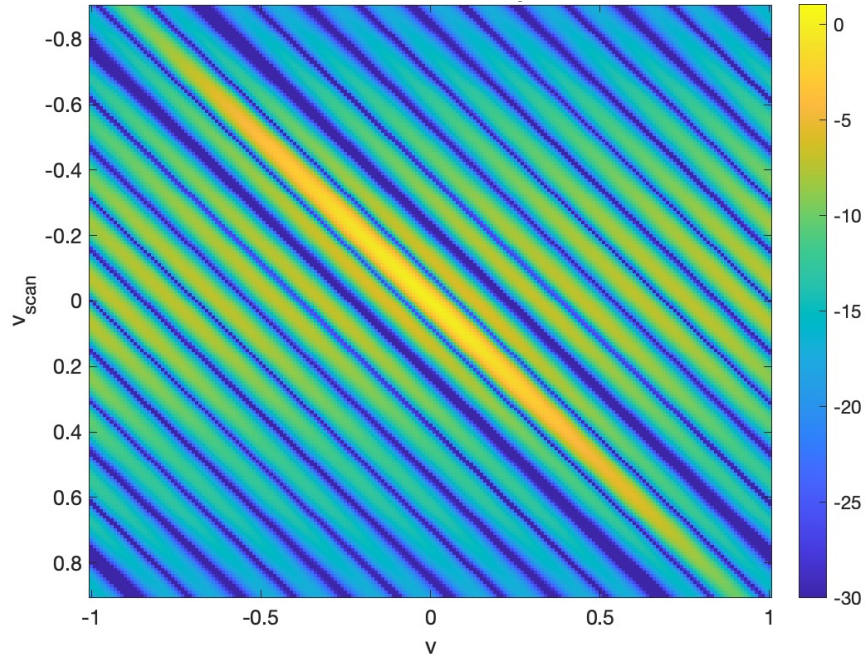


Figure 5.5: Simulated response for 8-element antenna receiver in  $u$ - $v$  coordinates for complete antenna scan.

lobes. In these situations, it is possible to add tapering to reduce the SLLs at the expense of HPBW. From this graph it can be seen that configuration no. 3 provides the best SLL over scan angle and this is the one which has been chosen for fabrication.

### 5.5.2 Non-uniform Antenna Array Fabrication

The selected antenna configuration no. 3 from Table 5.3 was fabricated with the same material and techniques presented in [1.4]. A detailed presentation on how the SIW antenna was designed can also be read in 2.11. The receiver antenna is depicted in Figure 5.8 which depicts configuration No. 3 as described in the previous section. The antenna uses the same substrate as described in [5.17], having similar return losses as the previous prototype. The antenna was made in July 2020 with Printech Ltd, in the UK and shipped in the Netherlands for measurements completed during the EUMA internship award in 2020.

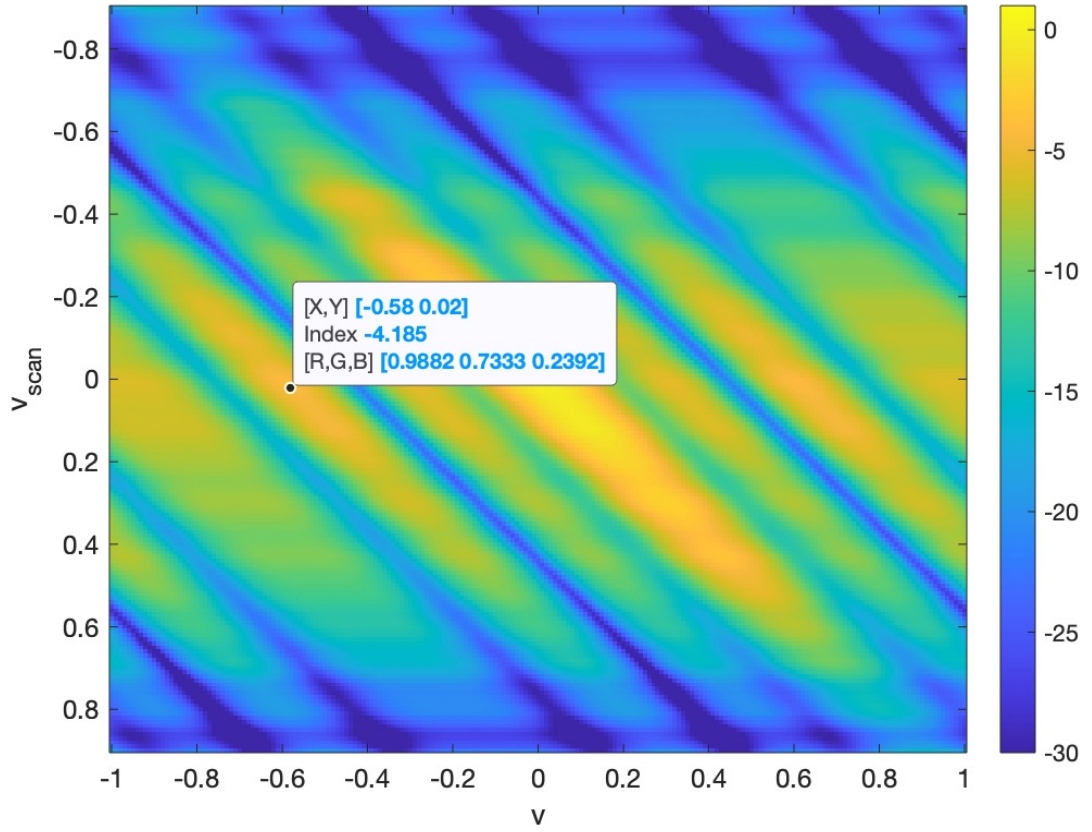


Figure 5.6: Measured UV response for antenna array beam steering for complete antenna scan, showing highest SLL.

## 5.6 Measurement Setup and Results

### 5.6.1 Antenna Beampatterns

Also shown in Fig. 5.8 is the FMCW hardware measurement setup for target detection. Here the Analog Devices raar has been connected to the antenna receivers with the help of 2.92mm co-axial cables and interfaced with Analog Devices SDP board to connect to the computer. The antenna was first measured for functionality. The measured and simulated return losses for the 8 elements for the antenna array are presented in Figure 5.9 and a good agreement between them can be seen. The antenna under test (AUT) was placed at 2.5m from the test horn antenna, and was measured at 24 GHz. The compared beampattern measurements and simulations can be seen in Figure 5.10 for the azimuth plane, while in Figure 5.11 the elevation pattern is presented. We can see there is good agreement between the measurements and simulations in both planes. The SLL is also at the expected -5 dB level. The realised gain for the antenna is 16.7 dB, only 0.7 dB down compared to the

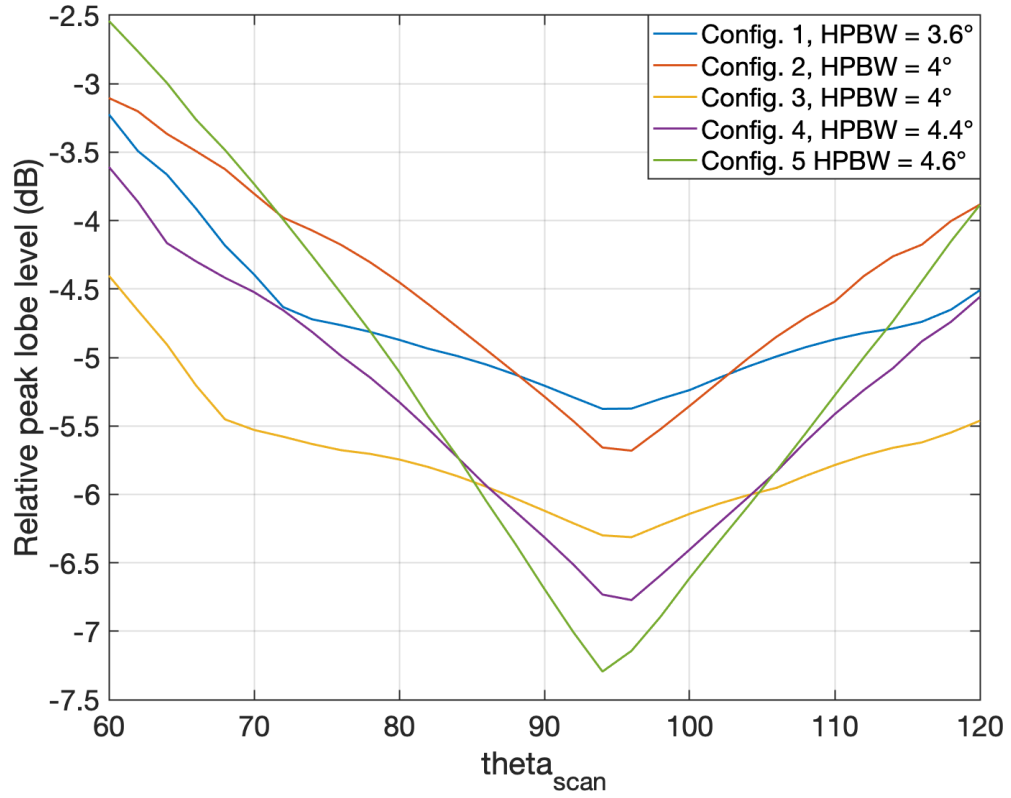
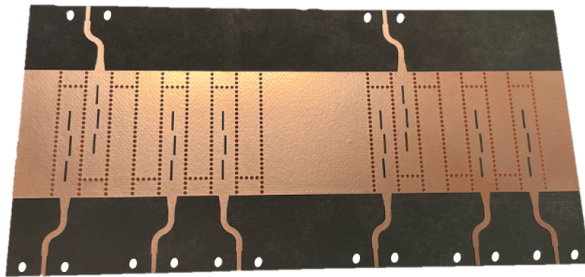
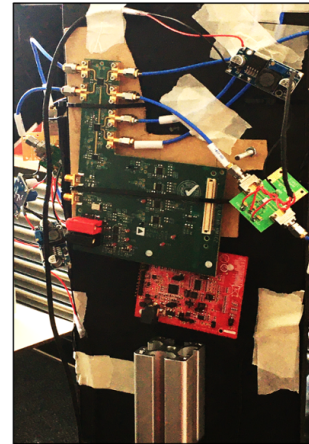


Figure 5.7: Side lobe level response comparison for 8-element array configuration with a large separation between arrays as described in Table 5.3.



Sparse 8-Element Antenna  
Array Receiver



Radar Setup for Sparse Antenna  
Radar Detection

Figure 5.8: Newly fabricated SIW transmitter and receiver antennas, and radar hardware setup for far-field measurement.

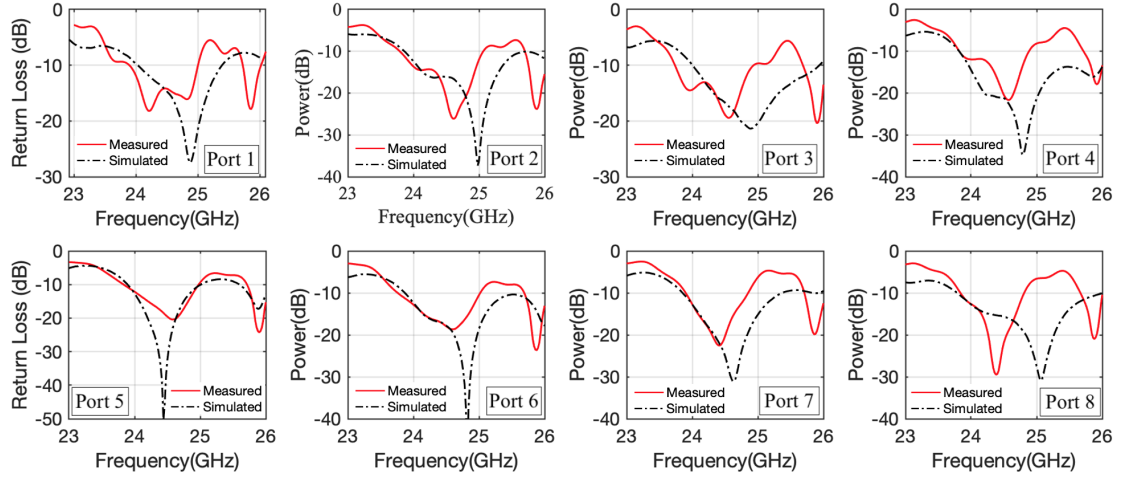


Figure 5.9: Simulated and measured return losses for the manufactured SIW sparse 8-element antenna array.

simulated 17.4 dB and the antenna efficiency is 83.5%.

### 5.6.2 Radar Measurements over frequency

A preliminary study has been done where the radar system bandwidth was tested for different values for the small corner reflector. This result can be seen in Figure 5.12. The side lobe levels for the 1.5 GHz measurements are improved compared to the 200 MHz bandwidth, therefore 1.5 GHz bandwidth was used for the measurement trials.

### 5.6.3 Radar Measurements with CS

For the target detection trial, two targets have been chosen to simulate target detection. The two targets represented here are an aluminium corner reflector with an rcs of  $30 \text{ cm}^2$ , as well as a metal plate with an edge also of 10 cm. The radar setup for the measurements has been depicted in Fig. C. These have been chosen due to the necessity of working in the far-field at the detection range. The corner reflector has been attached to a plastic pole which allowed its re-positioning for the target trials. The other target plate was placed at a fixed position in the anechoic chamber. The radar MIMO setup can be seen in Figure 5.13, where the antenna setup is illustrated, the target positions and the radar platform from TNO Radar Signal Processing group. This setup has been used similar to the setup as depicted in Fig.



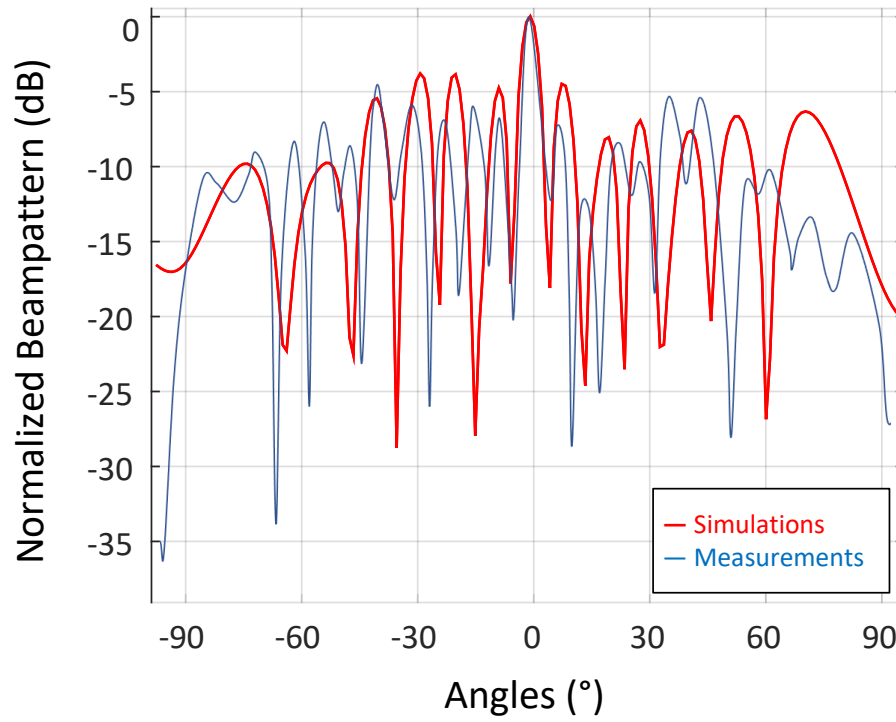


Figure 5.10: Azimuth beampattern response of 8-element SIW antenna receiver

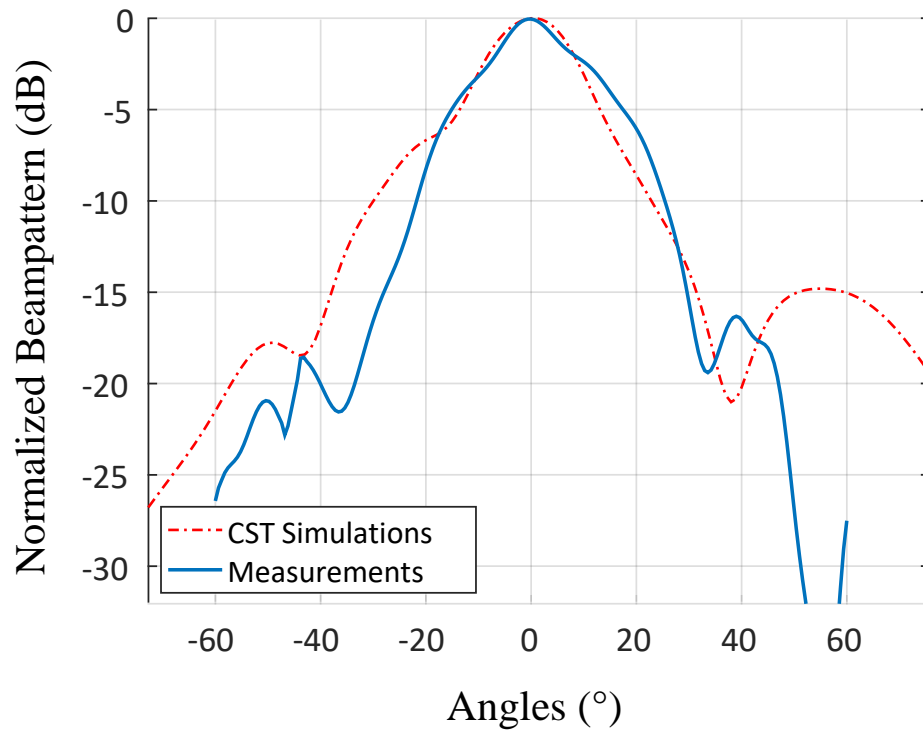


Figure 5.11: Elevation beampattern response of 8-element SIW antenna receiver

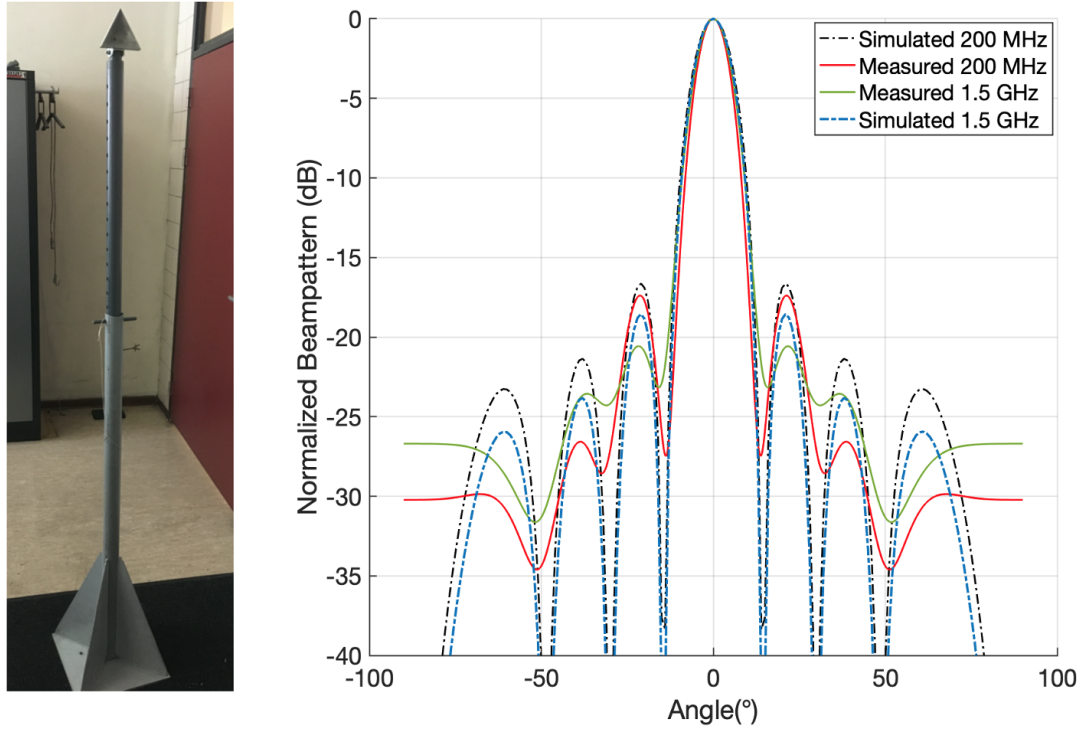


Figure 5.12: Normalised target return for frequency calibration at 200 MHz and 1.5 GHz for corner reflector with 10 cm size at 2.6 meter distance.

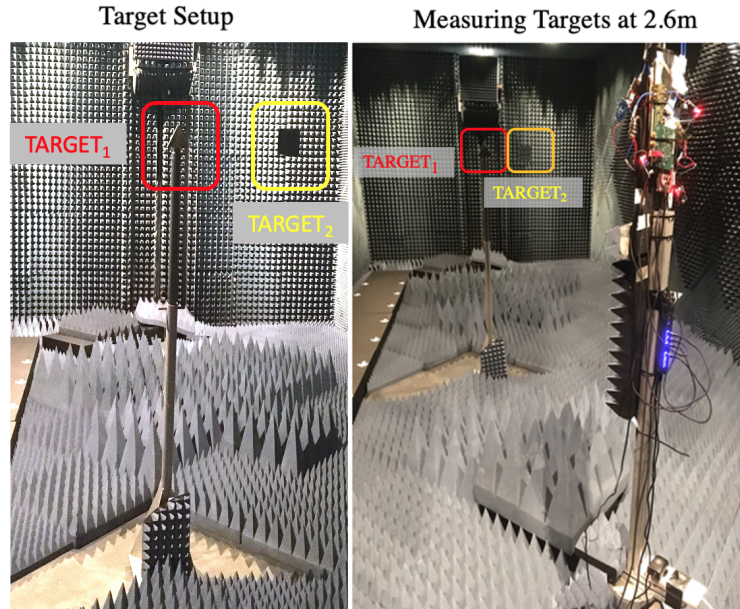


Figure 5.13: Radar hardware setup for target detection measurement comprising of two targets positioned at 2.6m, spaced at different angle separations.



C.

Measurement trials for the target detection have been carried out and results are reported here. The radar targets have been positioned at an angular separation of  $2^\circ$  between the center of each target. The detection has been compared with two algorithms, delay and sum (DAS) and CS. This results can be seen in Figure 5.14. The two targets distanced very close are not distinguishable with the DAS algorithm but they can be clearly identified with the CS algorithm, which shows the potential improvement of the CS implementation. As expected from then antenna measurements, the SLLs are high. If the CFAR threshold (see Chapter 2 on definition) is set at -5 dB then just the two targets are detected and no false targets are present. Therefore a new objective for this work is to find the best way of reducing the SLL while preserving HPBW.

#### 5.6.4 CS and Multiplication

In Chapter 4, the multiplication method is presented a smoothing function which is based on multiple readings of the target scenario and use beampattern pattern multiplication to smooth the SLL. The same technique is applied here for the CS algorithm to reduce the SLL and reduce the probability of false targets. By adding this technique, target detection response is much improved as an be seen in Figure 5.15, with an SLL of almost 40 dB. This is very helpful in situations where clutter would hinder performance, however, as it is noted in Chapter 4, the multiplication method does not increase angular resolution. The combination of both CS and multiplication yields a clearer image for automotive radar detection.

#### 5.6.5 Measurements with radar rotation

Another trial has been done with rotating the radar platform and checking the response of the radar for angles further from broadside. Six trials have been carried out with an angular target separation of  $20^\circ$  and rotation angle from  $0^\circ$  to  $-50^\circ$  (in the left plane). This shows the response of the radar for the right quadrant and the trials can be observed in Figure 5.16. These results shows a lot of noise due to the reduced power transmitted at the edges of the field of view. Hence, a system that is able to beamform at the transmitter (such as a Butler matrix network, see [3.39])

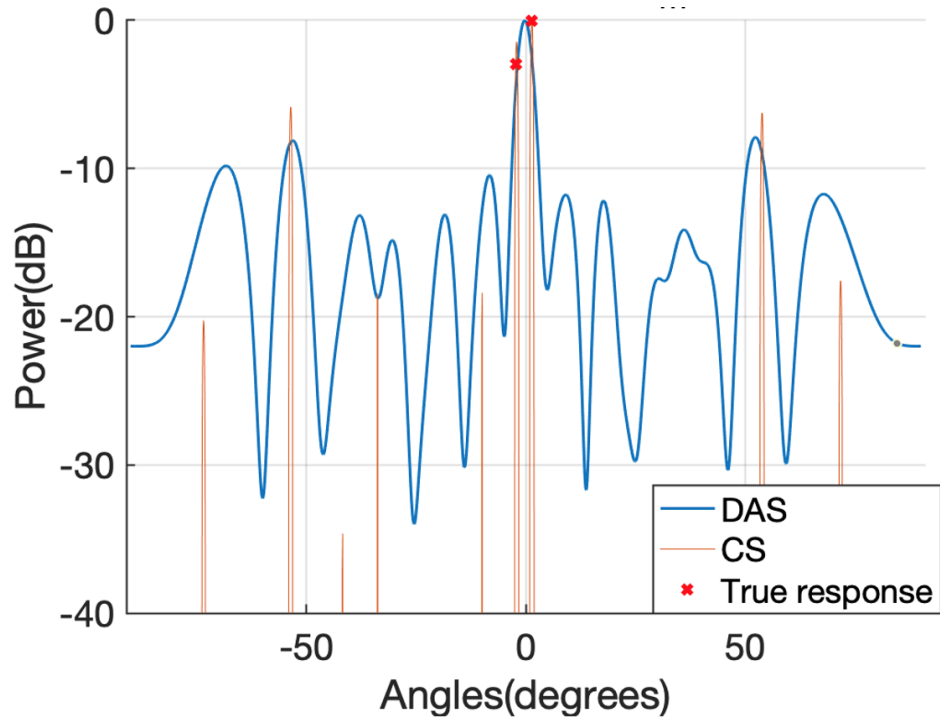


Figure 5.14: Final measurement for two targets spaced at 2 degrees at a distance of 2.6m as shown in Fig. 5.13, comparing delay-and-sum (DAS), compressive sensing (CS) with range resolution of 7.5cm (1.5 GHz bandwidth).

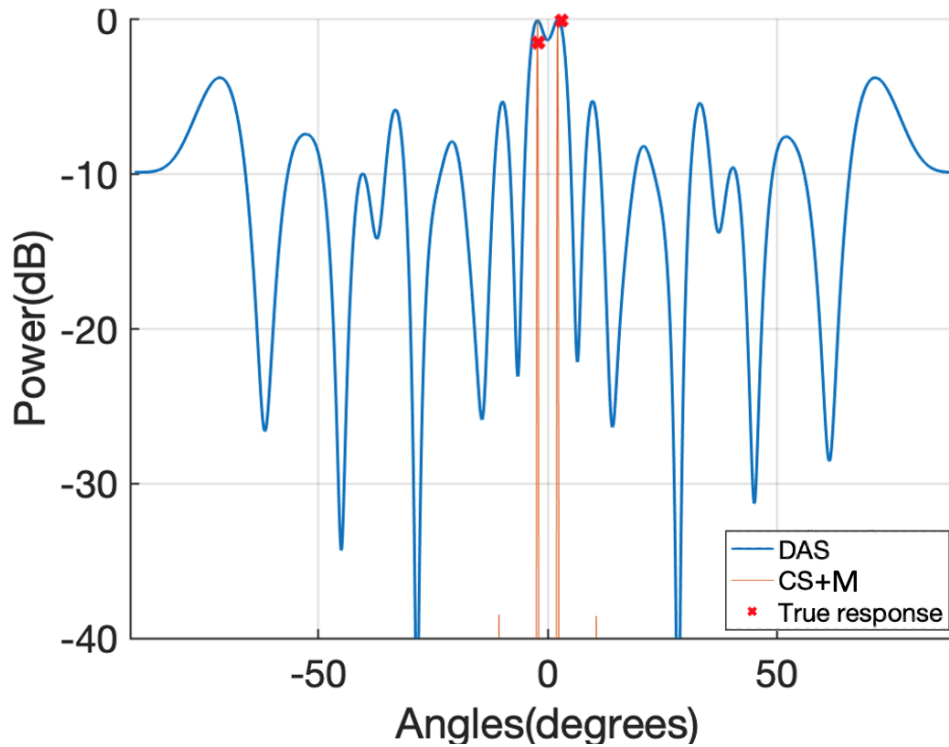


Figure 5.15: Final measurement for two targets spaced at 2 degrees apart at a distance of 2.6m as shown in Fig. 5.13, comparing delay-and-sum (DAS), compressive sensing with multiplication (CS+M) with range resolution of 7.5cm (1.5 GHz).

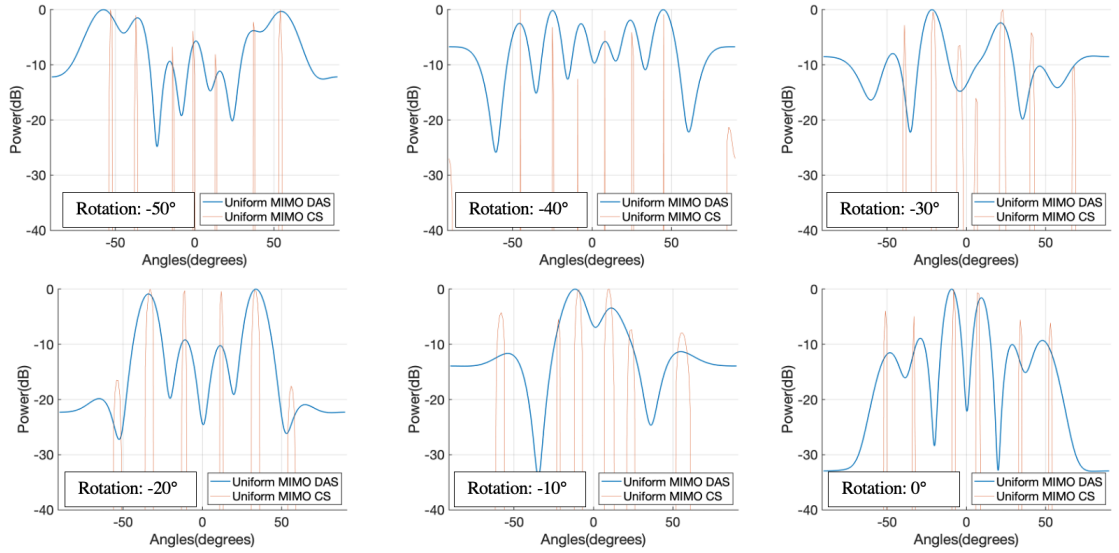


Figure 5.16: Measurement sweep for two targets spaced at 20 degrees apart at 2.6m as shown in Fig. 5.13, rotating the radar platform in 10° increments, while comparing delay and sum (DAS) and compressive sensing (CS) with 7.5cm range resolution (1.5 GHz).

can alleviate some of the problems encountered with detecting targets at the edges.

### 5.6.6 Discussion and limitations

It is clear that CS is able to resolve the targets better, but in this case, it can be seen that keeping the angular separation constant would have implied that this should be translated at different angles for the separate trials. Unfortunately, this is not the case with the detected images as the targets are separating more once the radar is rotated at a further angles. In this case, it is clear that the SLL response is affecting the measurement and also that the results are inconclusive since the expected results are not seen with the radar system rotation.

This effect can be traced due to several factors. At the time of the measurement, time based MIMO processing was taking place and some ports were changed manually in between measurements, which could have caused a slight shift of antenna positioning. The SLLs response can be affected by the noise of the system and calibrations may need several trials to accurately show a good measurement. In this scenario, an additional calibration procedure needs to be carried out. In conclusion we can find the following limitations:

- In the case where SNR is not enough, CS is not able to distinguish multiple targets, therefore it is important this is provided.
- Non-uniform antenna design reduces SLL and this can cause for the CS algorithm not to detect multiple targets.
- Multiplication can have limitations for targets that have a large difference in RCS.

## 5.7 Conclusions and future work

In this chapter, compressive sensing for automotive radar scenarios has been discussed. It has been demonstrated how non-uniform sparse arrays can aid radar detection by offering an enlarged virtual antenna aperture, while preserving an acceptable side-lobe level response, and this thesis presents results of a MIMO radar system with capability of detecting targets at an angular separation of just  $2^\circ$ . This work is also compared with other radar systems present in literature, identifying advantages and disadvantages of each. The work also discussed the methodology of obtaining a sparse antenna array design, given some constraints, such as antenna inter-element spacing and number of elements. Configurations have been compared for best possible radar angular resolution and side-lobe level, prior to the new antenna fabrication. Good agreement between simulations and measurements have been reported for antenna array characteristics which has been designed and measured throughout the project. In addition, a study was undertaken to obtain the SLL response with steering angle, determining the response of the radar while trying to identify objects at further angles within the FOV. Future work will discuss how to achieve better SLL response for the antenna design and improve SLL with scan angle as well.

## 5.8 Contributions by the candidate

In this chapter, the candidate has developed the compressive sensing algorithm (YALL1) for the angular target detection of the radar, beginning from the frequency domain signal reconstruction and obtaining the angular spectrum reconstruction as

desired. The measurements used a non-uniform spaced antenna receiver in the SIW technology, antenna which the candidate has designed in CST and it has been externally manufactured during July 2020 by Printech Technologies. The candidate has therefore performed measurements at the TNO facilities in the Netherlands with a new antenna which he designed and obtaining very good results. The non-uniform design has been obtained with the prolonged efforts of finding the best antenna array design, which has been found using an exhaustive search method. The array then was simulated and tested for side-lobe level response and half-power beamwidth for angular resolution. The beampatterns of the new array have also been simulated and measured by the candidate. Lastly, the compressive sensing measurements have been carried out by the candidate at the TNO facilities in the Netherlands.

# Chapter 6

## Conclusions

### 6.1 Motivation and goal

In this chapter, we will summarise the novelties of this thesis, draw a conclusion and discuss the opportunities of future work.

Radars system developments and their performance characteristics have been investigated in the context of the automotive industry with the aim of enhanced resolution. As it can be seen from Chapter 2, a comprehensive analysis of the automotive radar literature has been carried out to find which state-of-the art systems provide the best resolution, detection time, cost and the ease of manufacturing. Additionally, a market research (outlined in Chapter 3) was also carried out for prototyping a radar system outlined in the thesis. Multiple input multiple output (MIMO) systems together with newly developed substrate integrated waveguide (SIW) antenna arrays have been the focus of this research due to the improved characteristics and capabilities of these systems.

A focused approach on performance balanced with simplicity of design and keeping costs reasonable has been adopted throughout the work. These efforts have been widely recognised in the radar community, and so the first radar MIMO SIW system (outlined in chapter 3) which was presented in European Conference on Antennas and Propagation (EuCAP, London, 2018) was nominated for Best Antenna Applications paper, which classed it among the first 5/1050 papers submitted that year. During the same year, the multiplication spectral smoothing function outlined in Chapter 4 has received Best Student Paper Award at the International Sympo-

sium on Antenna Technology and Applied Electromagnetics (ANTEM), Waterloo, Canada, August, 2018. This recognition has been very motivating, and so in 2019, this work has also been awarded the European Microwave Association (EuMA)’s Internship Award which allowed research to be done up to 6 months at one of the best radar facilities in the industry at TNO Research and Defence, The Hague, Netherlands, where the compressive sensing and interpolation work has been developed and outlined in Chapters 4 and 5.

## 6.2 Novelty in this work

The automotive radar candidate systems which have been developed throughout the thesis have some advantages over conventional radar systems and some of these developments have been pioneered to enhance system performance, by using new techniques implemented here. Some of these points are highlighted below:

- Integration of SIW antenna arrays with a MIMO radar and performing radar measurements with an off the shelf 24 GHz radar system for short-range radar (SRR) applications.
- High percentage bandwidth antennas with SIW arrays that allow a stable impedance bandwidth of 1.5 GHz for a radar range resolution of 10 cm, and a design which is scalable to 77 GHz, allowing for as little as 3 cm separation distance between targets.
- Spectral multiplication method which can smooth out receiver radar data to allow better radar accuracy (improvement of -13 dB in side lobe level is reported in Chapter 4).
- The realisation of sparse antenna array using an heuristic search method for the antenna element positions to maximise angular resolution and reduce as much of possible SLL. The radar employs 32 elements which have a virtual array aperture of 47 elements at  $0.5\lambda$  spacing.
- Using compressive sensing together with sparse array antenna systems to facilitate sparse recovery using less hardware resources for the SIW MIMO radar system.
- Applying interpolation and extrapolation methods on the MIMO SIW radar to

further increase angular resolution by an additional 20% in antenna aperture.

- Using a sectorized radar sub-modular system to detect targets within  $\pm 90^\circ$  of the field-of-view, together with non-uniform antenna arrays.

### 6.3 Limitations of this work

Although there are many advancements with the use of the radar systems developed in this work, there are still many challenges that need to be addressed and would consist the starting point of future work. The known limitations of the work are:

- The use of 24 GHz radar systems are already phased out by the European Telecommunications Standards Institute (ETSI) and Federal Communications Commission (FCC) since the beginning of 2022, which makes the use of the current hardware not suitable for future radar systems.
- More losses are expected at 77 GHz due to the increased tolerances and difficulty of manufacturing at a smaller wavelength, and increased cost of manufacturing and prototyping.
- The smoothing multiplication method does not increase angular resolution, only improves accuracy by lowering the SLL of the detection. The aperture of the radar needs to be large enough for the targets to be detected and so the it will not discriminate for targets that are very close to each other.
- Compressive sensing does not reduce signal processing time in comparison to other sub-space based algorithms such as MUSIC and MVDR, although it processes less data, it reduces the hardware requirements for analogue-to-digital (ADC) converters.
- Sectorized sub-modular radars use multiple radar system which increase cost, however this also increases scalability of the manufacturing process which can be optimised by parallelising tasks.
- The size of the bumper is a limiting factor for the highly separated radar system. Since an average bumper has the size of one meter, it is therefore practical only to use highly separated radars within this space. The use of 77 GHz radar is beneficial in this case since the wavelength is approximately three time less than the 24 GHz wavelength.



## 6.4 Future work endeavours

The topics which have been discussed have opened the possibility of future work in the following areas for the automotive radar system research:

- The design, manufacturing and testing of an automotive radar system using SIW antennas at 77 GHz, using ultra wide band antennas, with the use of aforementioned methods outlined in this thesis.
- The development of SIW monopulse antenna arrays which have large antenna aperture and the development of a new monopulse radar signal processing algorithm which can integrate the smoothing multiplication function.
- The development of genetic algorithms such as Particle Swarm Optimisation or Simulated Annealing to detect optimal antenna array positions with non-uniform sparse array and the development of an antenna beamformer based on the same principles and the measurement of such a system in an anechoic chamber.
- The design, implementation and testing of a highly separated automotive radar system which is capable of improved detection and uses re-configurable antennas in order to shape the aperture of the radar corresponding to the detection scenario.
- The integration of pulse-width modulation (PMW) and other detection methods such as multiple frequency shift keying (MFSK) with the automotive radar system and data transmission in addition to the target detection capability.
- Using compressive sensing also in the range domain, and enhancing range resolution capability of the radar system.

Many areas of improvement still remain with the automotive radar system, and it is the duty of the design engineer to develop new methods of enhancing these types of systems. This thesis has covered some of the techniques which help achieve the goal of better resolution and improved detection for ultimate road user safety. The radar systems are also part of the in-sensor fusion capabilities of new automotive collision avoidance application present in newly manufactured vehicles. Thus, the automotive radar topics are going to be of wide interest among car manufacturers and researchers for future decades to come.

# Appendix A

## Compressive sensing beamforming implementation with YALL1

The YALL1 algorithm is divided into four sections: input, initialisation of the parameters, iteration of the projection and output of the reconstructed signal. In this case, the YALL1 algorithm is optimised to detect targets in the angular domain. The requirements for the algorithm are to have a matrix dictionary  $\mathbf{A}$ , and a set of measurements  $\mathbf{y}$ , chosen with a degree of sparsity  $k$ . Once the initialisation phase is done, the algorithm sets the parameters which will loop either until the maximum number of iterations is reached, or the stopping criteria for the algorithm are met. During each iteration, one target is identified by randomly undersampling the signal and re-creating the original image with back-projection. This method allows for Nyquist aliasing to disappear, however the side-lobe level (SLL) can pose an issue if the level is higher than smaller targets. Therefore, the design of the antenna is important for YALL1 since a good SLL response will be able to detect more targets.

### **Example of YALL1 iteration step:**

1. Detect strong signal component above the threshold.
2. Obtain sparse estimate based on threshold level.
3. Compute interference based on the detected targets and convolve sparse estimation.
4. Subtract interference signal from original to find targets that might have been masked by side lobe levels.
5. Continue iteration until stop criteria is met.

The following is the YALL1 pseudocode implementation:

---

**Algorithm 1** Your Algorithm for  $l_1$  (YALL1) pseudocode

---

```

1:
Require: measurement matrix  $\mathbf{A}$ , measurement vector  $\mathbf{y}$ ,
2: sparsity level  $k$ ,  $n \geq 0$ 
Ensure:  $k$ -sparse target vector  $\mathbf{x}$ ,  $\mathbf{x}^0 = 0$ ;
3: Initialisation:  $\text{tol}$ ,  $\rho$ ,  $B_{\max}$ ,  $\mu$ ,  $\text{maxit}$ , weights  $\mathbf{w}$ ,  $\gamma$ .
4:  $\rho = 0.01$ 
5:  $\text{maxit} = 9999$ 
6:  $w = 1$ 
7:  $\text{tol} = 5 \times 10^6$ 
8:  $B_{\max} \leftarrow \lim_{n \rightarrow \infty} y[n]$ 
9:  $\rho \leftarrow \rho / B_{\max}$ 
10:  $y \leftarrow y / B_{\max}$ 
11:  $\mathbf{x} = \mathbf{A}' * \mathbf{y}$ ;
12:  $\mathbf{x}^0 \leftarrow \mathbf{x} / \max(\mathbf{x})$ 
13:  $\mathbf{b} \leftarrow \mathbf{y}$ 
14:  $n \leftarrow \text{size}(x)$ 
15:  $z \leftarrow 0$ 
16:  $y \leftarrow 0$ 
17:  $\mathbf{A} \mathbf{t} \mathbf{y} \leftarrow 0$ 
18:  $\mu_{\text{orig}} \leftarrow \mu$ 
19:  $\rho_{\text{avg}} \leftarrow \rho / \mu$ 
20:  $\rho_{\text{avg}} \leftarrow \rho / \mu$ 
21:  $\mathbf{b}_{\text{avg}} \leftarrow \mathbf{b} / \mu$ 
22:  $\text{rel}_{\text{gap}} \leftarrow 0$ 
23:  $\text{rel}_{\rho} \leftarrow 0$ 
24:  $\text{stop} \leftarrow \text{false}$ 
25: Iteration:
26: while  $\text{iter} \neq \text{maxit}$  do
27:    $\text{iter}++$ 
28:    $\mathbf{x}_{\mu} \leftarrow \mathbf{x} / \mu$ 
29:    $\mathbf{y}_{\text{res}} \leftarrow \mathbf{A} * (\mathbf{A}' * \mathbf{y} - \mathbf{z} + \mathbf{x}_{\mu}) - \mathbf{b}_{\text{avg}}$ 

```

```

30:    $\mathbf{y}_{res} \leftarrow \mathbf{y}_{res} + \rho_{avg} * \mathbf{y}$ 
31:    $\mathbf{denom} \leftarrow \mathbf{A} \mathbf{y}' * \mathbf{A} \mathbf{y}$ ;
32:    $\mathbf{denom} \leftarrow \mathbf{denom} + \rho_{avg} * (\mathbf{y}'_{res} * \mathbf{y}_{res})$ ;
33:    $stp \leftarrow \text{real}(\mathbf{y}'_{res} * \mathbf{y}_{res}) / (\text{Re}(\mathbf{denom}) + \epsilon)$ ;
34:    $\mathbf{y} \leftarrow \mathbf{y} - stp * \mathbf{y}_{res}$ ;
35:    $\mathbf{A} \mathbf{y} \leftarrow \mathbf{A} \mathbf{y} - stp * \mathbf{A} \mathbf{y}$ ;
36:    $z \leftarrow \mathbf{A} \mathbf{y} + \mathbf{x}_\mu$ ;
37:    $\mathbf{z} = \mathbf{z} .* \mathbf{w} ./ \max(\mathbf{w}, \text{abs}(\mathbf{z}))$ ; ▷ Projection
38:    $\mathbf{res} \leftarrow \mathbf{A} \mathbf{y} - \mathbf{z}$ ;
39:    $\mathbf{x}_{projected} = \mathbf{x}$ ;
40:    $\mathbf{x} = \mathbf{x} + (\gamma * \mu) * \mathbf{res}$ ;
41:   if  $iter$  is even then
42:        $q \leftarrow 0.1$  ▷ Check stopping conditions
43:        $\mathbf{res}_{normal} \leftarrow \text{norm}(\mathbf{res})$ 
44:        $\mathbf{objp} = \sum |\mathbf{w} .* \mathbf{x}|$ ;
45:        $\mathbf{objd} = \mathbf{y}' * \mathbf{y}$ ;
46:        $rel_\rho \leftarrow \mathbf{res}_{normal} / \text{norm}(\mathbf{z})$ 
47:        $\mathbf{res}_{projection} = \mathbf{A} * \mathbf{x} - \mathbf{y}$ ;
48:        $\mathbf{resnorm}_{projection} = \text{norm}(\mathbf{res}_{projection})$ 
49:        $\mathbf{objp} = \mathbf{objp} + (0.5/\rho) * \mathbf{resnorm}_{projection}^2$ ;
50:        $\mathbf{objd} = \mathbf{objd} - (0.5 * \rho) * \text{norm}(\mathbf{y})^2$ ;
51:        $rel_{gap} = |(\mathbf{objd} - \mathbf{objp})| / |(\mathbf{objp})|$ ;
52:        $\text{stop} \leftarrow false$ ;
53:        $\mathbf{x}_{chg} = \text{norm}(\mathbf{x} - \mathbf{x}_p) / \text{norm}(\mathbf{x})$ ;
54:       if  $\mathbf{x}_{chg} < tol * (1 - q)$  then ▷ Stop if not within tolerance
55:            $\text{stop} \leftarrow true$ 
56:       else
57:           if  $\mathbf{x}_{chg} < tol * (1 + q)$  and  $rel_{gap} < tol$  and  $rel_\rho < tol$  then
58:                $\text{stop} \leftarrow true$ 
59:           end if
60:       end if
61:   if  $\text{stop}$  then
    
```

```

62:         break;
63:     end if
64:     if iter is even then                                     ▷ Update the mean value
65:         mfrac = 0.1;
66:         big = 50;
67:         nup = 8;
68:          $\mu_{min} = mfrac^{nup} * \mu_{orig}$ ;
69:          $update \leftarrow (rel_{gap} > big * rel_{\rho})$  and  $\mu > 1.1 * \mu_{min}$  and  $iter > 10$ 
70:     end if
71:     if update then
72:          $\mu = max(mfrac * \mu, \mu_{min})$ ;
73:          $\rho_{avg} = rho / \mu$ ;
74:          $\mathbf{b}_{abg} = \mathbf{b} / \mu$ ;
75:     end if
76: end if
77: end while
78:  $\mathbf{x} \leftarrow \mathbf{x} * Bmax$ 

```

---

## Appendix B

# Additional Simulations with the Multiplication Method

This section aims to provide additional data for the use of the multiplication method, as there are some cases where angular target detections would not benefit from the use of multiplication. There are three cases presented:

1. When there are 10 dB difference between the RCS of the targets.
2. When there are 20 dB difference between the RCS of the targets.
3. When there are 20 dB difference between the RCS of the targets.

For each of the cases, we have varied the multiplication factor and observe what is the effect on the target responses for a classic beamforming processing. In the first case (Fig. B.1), we can see that the multiplication method manages to reduce the SLL, but the difference between the two targets is now 40 dB in Fig. B.2 when the multiplication factor increases to 2. This difference increases more than 80 dB when  $M = 3$  (in Fig. B.3). However, when the difference between the two targets is 20 dB (as seen in Fig. B.4), it is clear from the start that the pedestrian is not detected because of the side lobes and also the multiplication algorithm does not help with its identification (Fig. B.5). One last interesting aspect is to probe what happens when the two targets are similar in RCS as can be seen in Fig. B.6. Once the smoothing process happens, the side-lobes almost disappear as seen in Fig. B.7 and when the multiplication factor is increased to 3, only the targets are shown as seen in Fig. B.8.

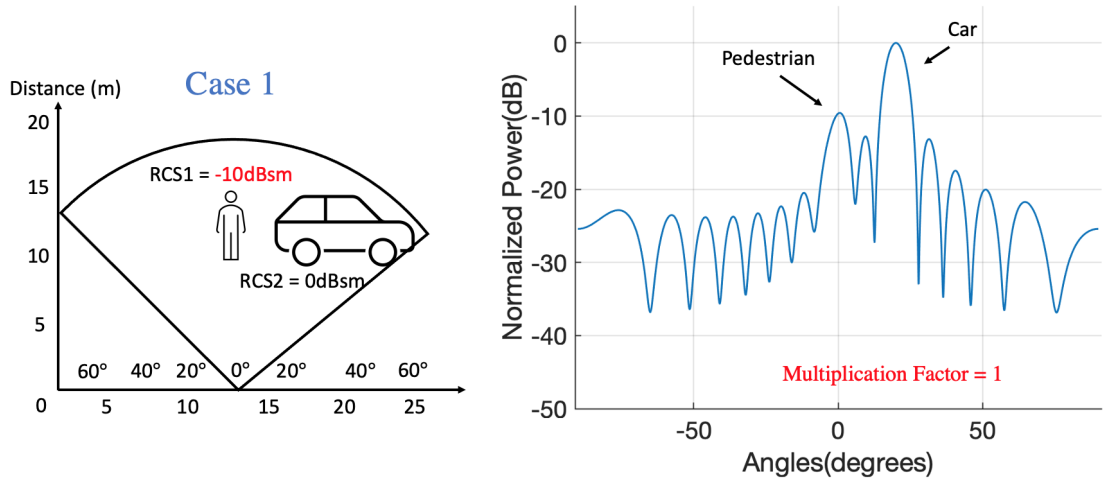


Figure B.1: Diagram showing the multiplication scenario where the radar cross section difference between the pedestrian and the car is 10 db and the multiplication factor is set to  $M = 1$ .

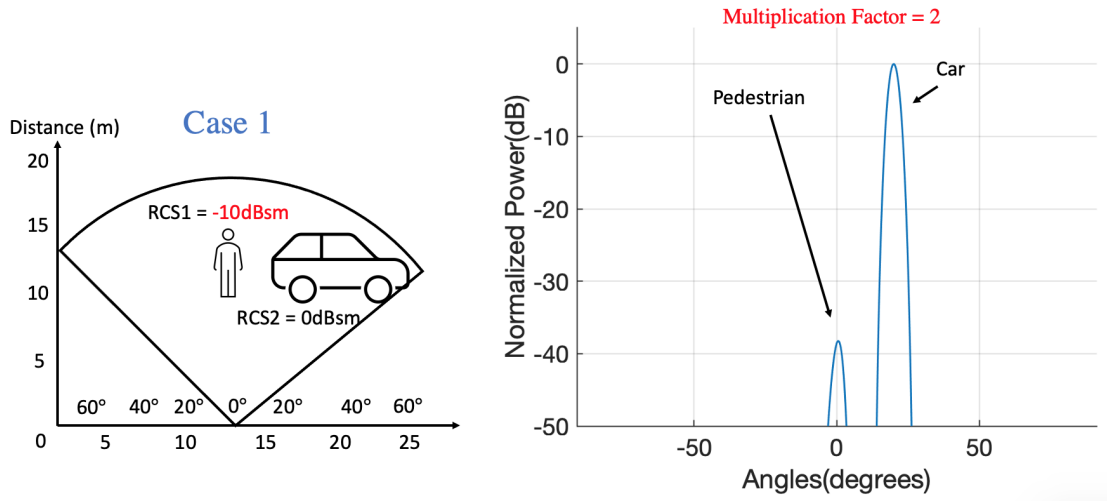


Figure B.2: Diagram showing the multiplication scenario where the radar cross section difference between the pedestrian and the car is 10 db and the multiplication factor is set to  $M = 2$ .

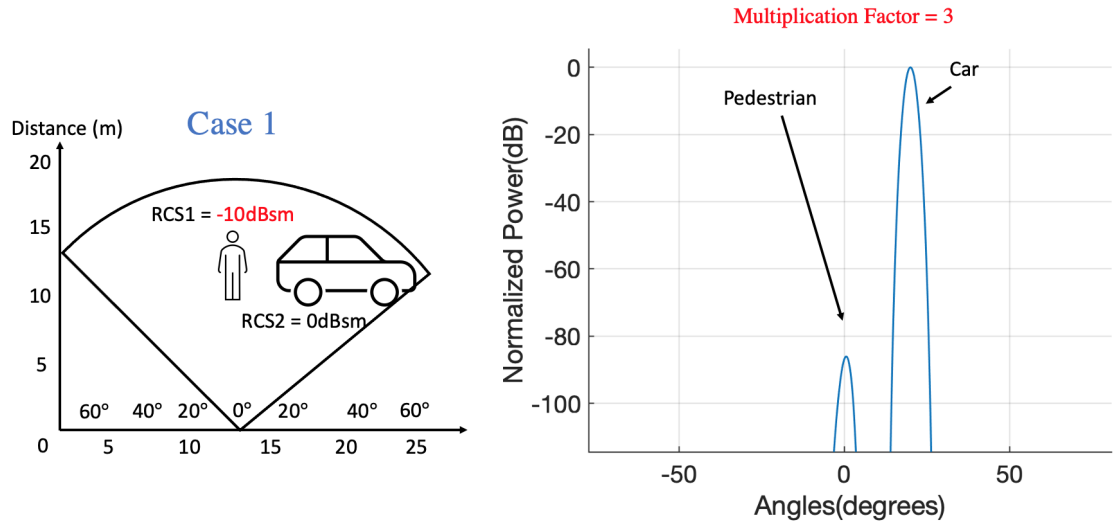


Figure B.3: Diagram showing the multiplication scenario where the radar cross section difference between the pedestrian and the car is 10 db and the multiplication factor is set to  $M = 3$ .

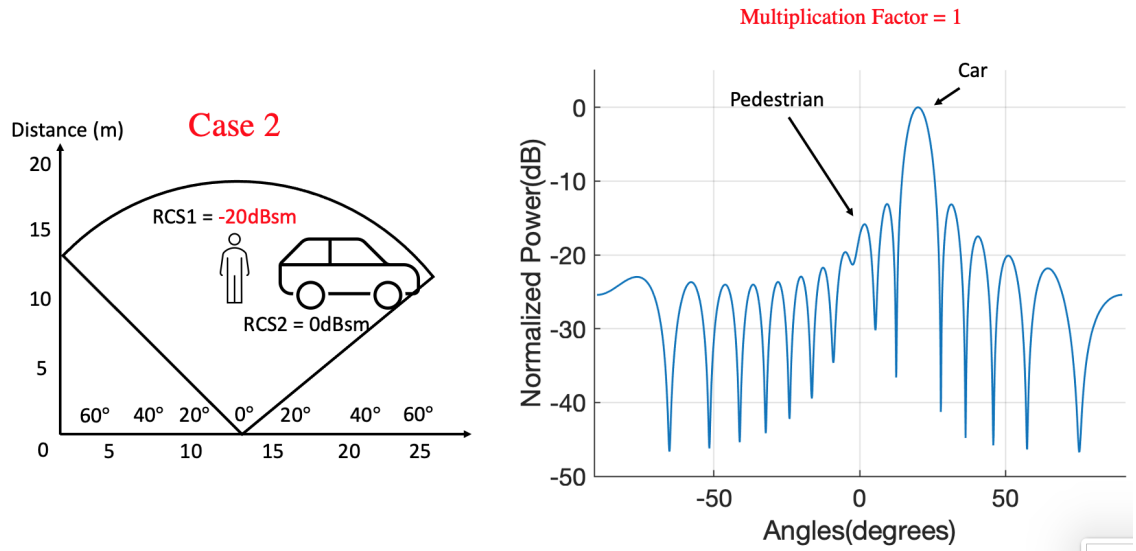


Figure B.4: Diagram showing the multiplication scenario where the radar cross section difference between the pedestrian and the car is 20 db and the multiplication factor is set to  $M = 1$ .



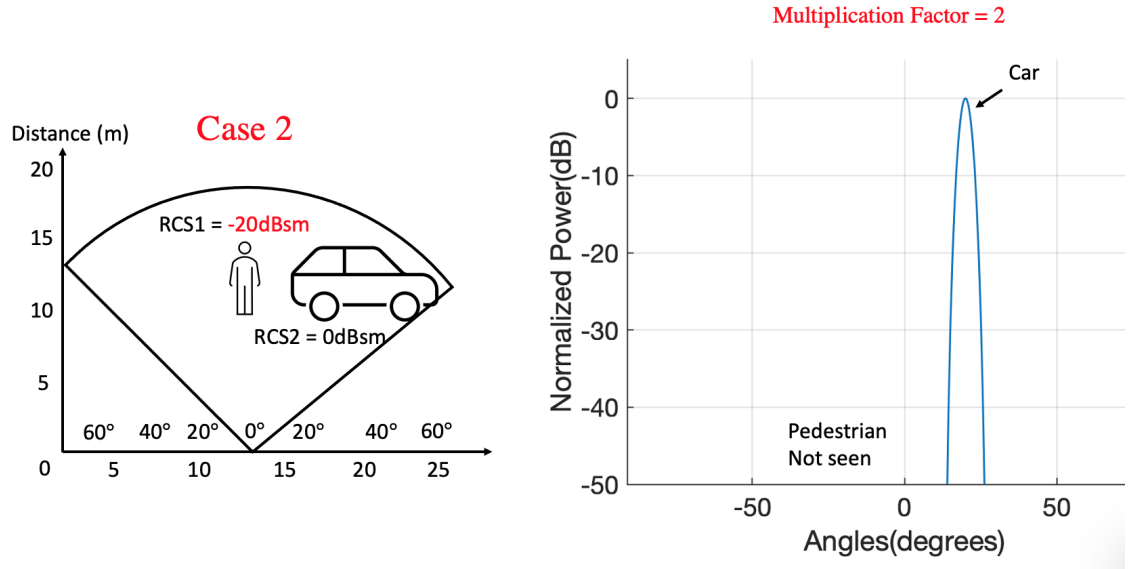


Figure B.5: Diagram showing the multiplication scenario where the radar cross section difference between the pedestrian and the car is 20 db and the multiplication factor is set to  $M = 2$ .

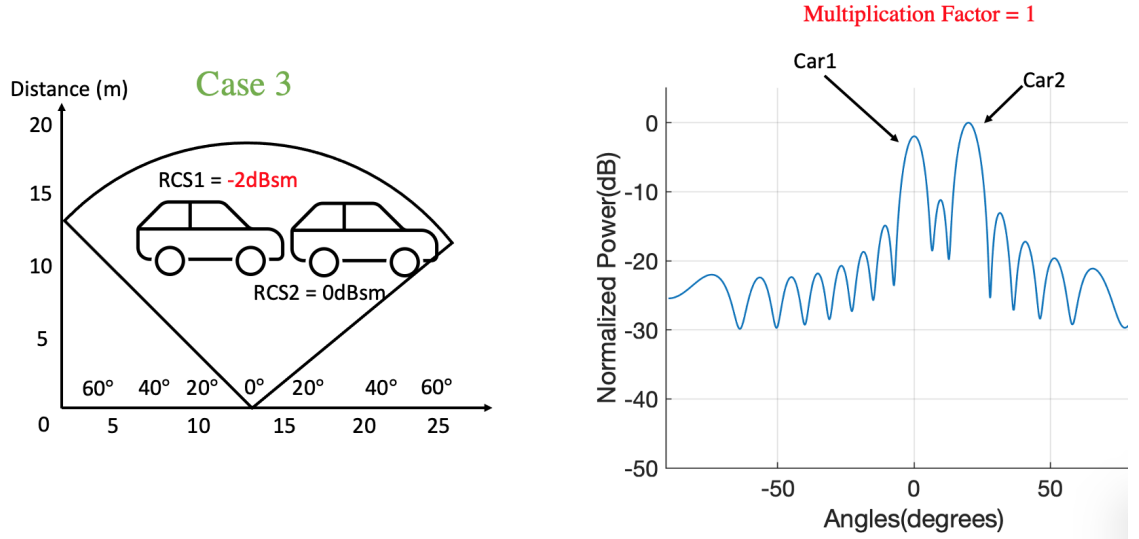


Figure B.6: Diagram showing the multiplication scenario where the radar cross section difference between two cars is 2 dB and the multiplication factor is set to  $M = 1$ .

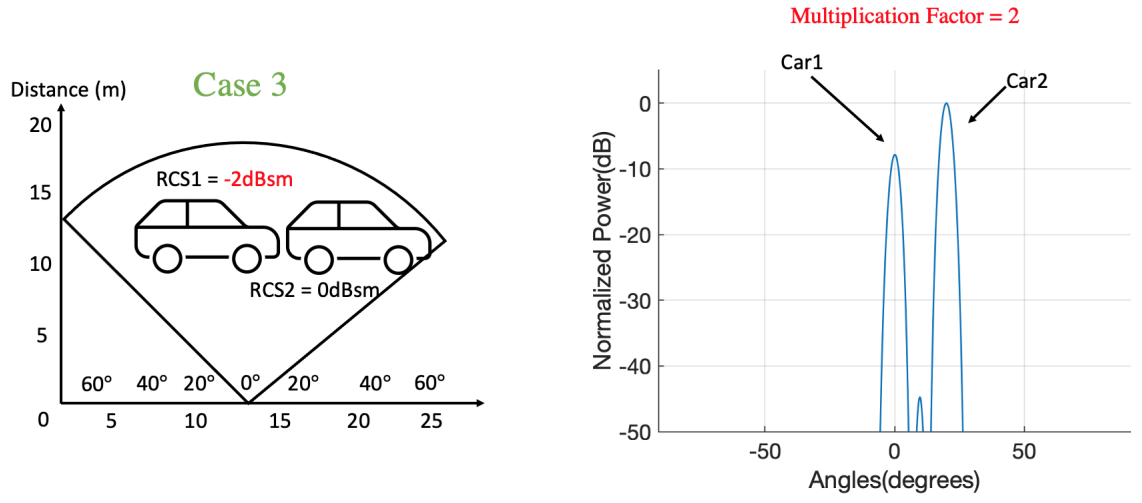


Figure B.7: Diagram showing the multiplication scenario where the radar cross section difference between two cars is 2 dB and the multiplication factor is set to  $M = 2$ .

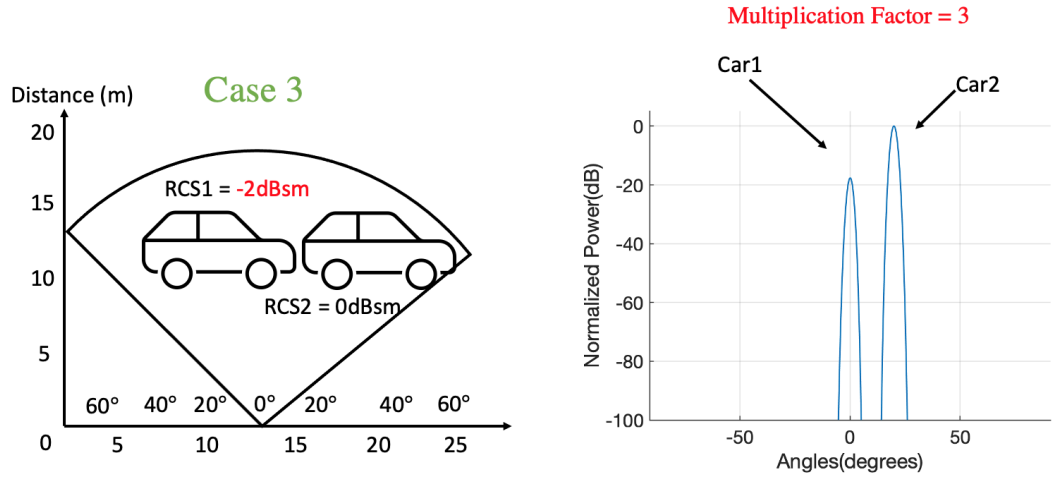


Figure B.8: Diagram showing the multiplication scenario where the radar cross section difference between two cars is 2 dB and the multiplication factor is set to  $M = 3$ .

## Appendix C

# Measurement Setup for Anechoic Chamber Measurements

This short appendix is designed as a reference for all measurements which have been carried out in the anechoic chamber, where two targets have been used.

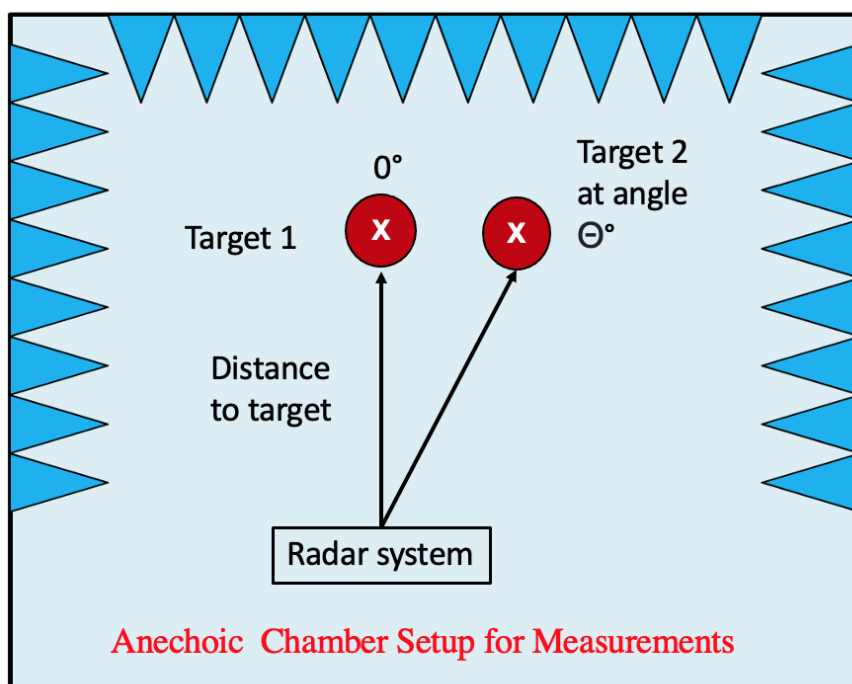


Figure C.1: Diagram showing the chamber setup for two targets for each of the measurements presented in previous chapter

# References: Chapter 1

- [1.1] Christian Waldschmidt, Juergen Hasch, and Wolfgang Menzel. “Automotive Radar—From First Efforts to Future Systems”. In: *IEEE Journal of Microwaves* 1.1 (2021), pp. 135–148.
- [1.2] Cedric Malaquin and Antoine Bonnabel. “Automated Driving: Market Perspective for Radar”. In: *European Microwave Week 2019: Automotive Forum*. Yole Development, 2019.
- [1.3] M Kunert et al. “The Role of Automotive Radars in future automated Driving Functions”. In: *European Microwave Week 2019: Automotive Forum*. Robert Bosch GmbH, 2019.
- [1.4] Cristian Alistarh *et al.* “Millimetre-Wave FMCW MIMO Radar System Development Using Broadband SIW Antennas”. In: *2018 12th European Conference on Antennas and Propagation (EUCAP)*. Jan. 1, 2018. published.
- [1.5] Cristian Alistarh *et al.* “Sub-modular FMCW MIMO Radar Design by Non-uniform Sparse Arrays”. In: *IEEE Journal of Microwaves (submitted)* (2021).
- [1.6] Cristian Alistarh et al. “Millimeter-wave Automotive Radar using Extrapolation for Improved Angular Resolution”. In: *2020 17th European Radar Conference (EuRAD)*. 2021, pp. 394–397.
- [1.7] Cristian A Alistarh et al. “Spectral Smoothing by Multiple Radar Pattern Multiplication for Improved Accuracy”. In: *2018 18th International Symposium on Antenna Technology and Applied Electromagnetics (ANTEM)*. IEEE. 2018, pp. 1–2.
- [1.8] Cristian Alistarh et al. “Compressed Sensing for MIMO Radar using SIW Antennas for High Resolution Detection”. In: *2021 18th European Radar Conference (EuRAD)*. IEEE. 2022.

## References: Chapter 2

- [2.1] Jessica Hammett. “‘The Invisible Chain by Which All Are Bound to Each Other’: Civil Defence Magazines and the Development of Community During the Second World War”. In: *Journal of War & Culture Studies* 11.2 (2018), pp. 117–135.
- [2.2] Manikas Athanassios. *EE3-27: Principles of Classical and Modern Radar Continuous Wave (CW) Radar*. Department of Electrical & Electronic Engineering Imperial College London, 2020.
- [2.3] Merrill I Skolnik. *Introduction to radar systems*. McGraw-Hill, 2007, pp. 68–98.
- [2.4] M. Cheney and B. Borden. *Fundamentals of Radar Imaging, Chapter 4*. Society for Industrial and Applied Mathematics, 2009. DOI: 10.1137/1.9780898719291. eprint: <https://epubs.siam.org/doi/pdf/10.1137/1.9780898719291>. URL: <https://epubs.siam.org/doi/abs/10.1137/1.9780898719291>.
- [2.5] Jürgen Hasch et al. “Millimeter-wave technology for automotive radar sensors in the 77 GHz frequency band”. In: *IEEE Transactions on Microwave Theory and Techniques* 60.3 (2012), pp. 845–860.
- [2.6] Mark A Richards et al. *Principles of modern radar, Chapter 21*. Citeseer, 2010.
- [2.7] Federal Communications Commission (FCC). *Radar Services in the 76-81 GHz Band*. Federal Communications Commission (FCC), 2017.
- [2.8] Karthik Ramasubramanian and Kishore Ramaiah. “Moving from Legacy 24 GHz to State-of-the-Art 77-GHz Radar”. In: *ATZelektronik worldwide* 13.3 (2018), pp. 46–49.

- [2.9] Constantine A Balanis. *Antenna Theory: Analysis and Design, Chapter 6*. John Wiley & Sons, 2005.
- [2.10] Graham Brooker. *High Angular-Resolution Techniques*. Radar, Sonar and; Navigation. Institution of Engineering and Technology, 2009, pp. 481–538. DOI: 10.1049/SBRA014E\_ch12. URL: [http://digital-library.theiet.org/content/books/10.1049/sbra014e\\_ch12](http://digital-library.theiet.org/content/books/10.1049/sbra014e_ch12).
- [2.11] Frank C Robey et al. “MIMO radar theory and experimental results”. In: *Conference Record of the Thirty-Eighth Asilomar Conference on Signals, Systems and Computers, 2004*. Vol. 1. IEEE. 2004, pp. 300–304.
- [2.12] Jacques Dorey and Gerard Garnier. “The RIAS pulsed synthetic-antenna radar”. In: *L’Onde Electrique* 69 (1989), pp. 36–44.
- [2.13] Jian Li and Petre Stoica. *MIMO radar signal processing*. John Wiley & Sons, 2009.
- [2.14] Sujeet Milind Patole et al. “Automotive radars: A review of signal processing techniques”. In: *IEEE Signal Processing Magazine* 34.2 (2017), pp. 22–35.
- [2.15] Jian Li and Petre Stoica. “MIMO radar with colocated antennas”. In: *IEEE Signal Processing Magazine* 24.5 (2007), pp. 106–114.
- [2.16] Igal Bilik et al. “Automotive MIMO radar for urban environments”. In: *2016 IEEE Radar Conference (RadarConf)*. IEEE. 2016, pp. 1–6.
- [2.17] Florian Engels, Markus Wintermantel, and Philipp Heidenreich. “Automotive MIMO radar angle estimation in the presence of multipath”. In: *2017 European Radar Conference (EURAD)*. IEEE. 2017, pp. 82–85.
- [2.18] Clemens Pfeffer et al. “FMCW MIMO radar system for frequency-division multiple TX-beamforming”. In: *IEEE transactions on microwave theory and techniques* 61.12 (2013), pp. 4262–4274.
- [2.19] Eran Fishler et al. “MIMO radar: An idea whose time has come”. In: *Proceedings of the 2004 IEEE Radar Conference (IEEE Cat. No. 04CH37509)*. IEEE. 2004, pp. 71–78.
- [2.20] J Li and P. Stoica. *MIMO radar signal processing*. John Wiley & Sons, 2008.

- [2.21] D. Mateos-Núñez et al. “Sparse array design for Automotive MIMO Radar”. In: *2019 16th European Radar Conference (EuRAD)*. 2019, pp. 249–252.
- [2.22] Alexander M Haimovich, Rick S Blum, and Leonard J Cimini. “MIMO radar with widely separated antennas”. In: *IEEE Signal Processing Magazine* 25.1 (2008), pp. 116–129.
- [2.23] Bon-Hyun Ku et al. “A 77-81 GHz 16-Element Phased-Array Receiver With  $\pm 50^\circ$  Beam Scanning for Advanced Automotive Radars”. In: *IEEE Trans. Microw. Theory Techn.* 62.11 (2014), pp. 2823–2832.
- [2.24] Eray Topak et al. “A novel millimeter-wave dual-fed phased array for beam steering”. In: *IEEE Transactions on Microwave Theory and Techniques* 61.8 (2013), pp. 3140–3147.
- [2.25] Osama Khan et al. “Hybrid Thin Film Antenna for Automotive Radar at 79 GHz”. In: *IEEE Transactions on Antennas and Propagation* 65.10 (2017), pp. 5076–5085.
- [2.26] Joonhong Park et al. “76–81-GHz CMOS transmitter with a phase-locked-loop-based multichirp modulator for automotive radar”. In: *IEEE Transactions on Microwave Theory and Techniques* 63.4 (2015), pp. 1399–1408.
- [2.27] Cristian Alistarh et al. “Millimetre-Wave FMCW MIMO Radar System Development Using Broadband SIW Antennas”. In: *2018 12th European Conference on Antennas and Propagation (EUCAP)* (Apr. 2018).
- [2.28] Yingrui Yu et al. “Optimization and Implementation of SIW Slot Array for Both Medium and Long Range 77GHz Automotive Radar Application”. In: *IEEE Transactions on Antennas and Propagation* (2018).
- [2.29] Clemens Pfeffer et al. “FMCW MIMO radar system for frequency-division multiple TX-beamforming”. In: *IEEE Transactions on Microwave Theory and Techniques* 61.12 (2013), pp. 4262–4274.
- [2.30] Junfeng Xu, Zhi Ning Chen, and Xianming Qing. “CPW center-fed single-layer SIW slot antenna array for automotive radars”. In: *IEEE Transactions on Antennas and Propagation* 62.9 (2014), pp. 4528–4536.

- [2.31] Claudia Vasanelli, Tobias Ruess, and Christian Waldschmidt. “A 77-GHz cavity antenna array in PCB technology”. In: *Microwave Symposium (MMS), 2015 IEEE 15th Mediterranean*. IEEE. 2015, pp. 1–4.
- [2.32] Yuan-Hung Hsiao et al. “A 77-GHz 2T6R transceiver with injection-lock frequency sextupler using 65-nm CMOS for automotive radar system application”. In: *IEEE Trans. Microw. Theory Techn* 64.10 (2016), pp. 3031–3048.
- [2.33] Claudia Vasanelli et al. “Assessment of a Millimeter-Wave Antenna System for MIMO Radar Applications”. In: *IEEE Antennas and Wireless Propagation Letters* 16 (2017), pp. 1261–1264.
- [2.34] Jürgen Hasch et al. “Millimeter-wave technology for automotive radar sensors in the 77 GHz frequency band”. In: *IEEE Trans. Microw. Theory Techn.* 60.3 (2012), pp. 845–860.
- [2.35] D Bleh et al. “A 100 GHz FMCW MIMO radar system for 3D image reconstruction”. In: *Radar Conference (EuRAD), 2016 European*. IEEE. 2016, pp. 37–40.
- [2.36] Jonathan Bechter, Muhammad Rameez, and Christian Waldschmidt. “Analytical and experimental investigations on mitigation of interference in a DBF MIMO radar”. In: *IEEE Transactions on Microwave Theory and Techniques* 65.5 (2017), pp. 1727–1734.
- [2.37] Claudia Vasanelli, Rahul Batra, and Christian Waldschmidt. “Optimization of a MIMO radar antenna system for automotive applications”. In: *Antennas and Propagation (EUCAP), 2017 11th European Conference on*. IEEE. 2017, pp. 1113–1117.
- [2.38] Mohammad Mosalanejad et al. “Stacked patch antenna sub-array with low mutual coupling for 79 GHz MIMO radar applications”. In: *Antennas and Propagation (EUCAP), 2017 11th European Conference on*. IEEE. 2017, pp. 190–194.
- [2.39] Jun Xu et al. “An Array Antenna for Both Long-and Medium-Range 77 GHz Automotive Radar Applications”. In: *IEEE Transactions on Antennas and Propagation* 65.12 (2017), pp. 7207–7216.



- [2.40] Daniel Schindler et al. “MIMO-OFDM Radar Using a Linear Frequency Modulated Carrier to Reduce Sampling Requirements”. In: *IEEE Transactions on Microwave Theory and Techniques* (2018).
- [2.41] Muhammad Rameez, Mattias Dahl, and Mats I Pettersson. “Adaptive digital beamforming for interference suppression in automotive FMCW radars”. In: *Radar Conference (RadarConf18), 2018 IEEE*. IEEE. 2018, pp. 0252–0256.
- [2.42] Tristan Visentin, Jürgen Hasch, and Thomas Zwick. “Polarimetric RCS Measurements of Selected Two-Wheeled Vehicles for Automotive Radar,” in: *20th European Microwave Week (EuMW)* (2017).
- [2.43] Enric Miralles et al. “Slotted ESIW Antenna with high efficiency for a MIMO Radar Sensor”. In: *Radio Science* 53.5 (2018), pp. 605–610.
- [2.44] Fabian Roos et al. “Waveform multiplexing using chirp rate diversity for chirp-sequence based MIMO radar systems”. In: *2018 IEEE Radio and Wireless Symposium (RWS)*. Universität Ulm. 2018, pp. 60–63.
- [2.45] Matthias Steinhauer et al. “Millimeter-wave-radar sensor based on a transceiver array for automotive applications”. In: *IEEE Trans. Microw. Theory Techn.* 56.2 (2008), pp. 261–269.
- [2.46] Reinhard Panhuber et al. “System concept for the imaging MIMO radar of the radar warning and information system RAWIS”. In: *EUSAR 2016: 11th European Conference on Synthetic Aperture Radar, Proceedings of*. VDE. 2016, pp. 1–4.
- [2.47] Z. Li and K. Wu. “24-GHz Frequency-Modulation Continuous-Wave Radar Front-End System-on-Substrate”. In: *IEEE Transactions on Microwave Theory and Techniques* 56.2 (2008), pp. 278–285. ISSN: 0018-9480. DOI: 10.1109/TMTT.2007.914363.
- [2.48] Joachim Massen et al. “A 79 GHz SiGe short-range radar sensor for automotive applications”. In: *International Journal of Microwave and Wireless Technologies* 5.1 (2013), pp. 5–14. ISSN: 17590787. DOI: 10.1017/S1759078712000669.

- [2.49] “Design of an FMCW radar baseband signal processing system for automotive application”. In: *SpringerPlus* 5.1 (2016), pp. 1–16. DOI: 10.1186/s40064-015-1583-5.
- [2.50] M. Andres et al. “3D detection of automobile scattering centers using UWB radar sensors at 24/77 GHz”. In: *IEEE Aerospace and Electronic Systems Magazine* 28.3 (2013), pp. 20–25. DOI: 10.1109/MAES.2013.6495649.
- [2.51] Hasan Iqbal et al. “SAR imaging in an automotive scenario”. In: *Mediterranean Microwave Symposium* 2015-January (2015). ISSN: 21579830. DOI: 10.1109/MMS.2015.7375430.
- [2.52] Igal Bilik et al. “Automotive MIMO radar for urban environments”. In: *2016 IEEE Radar Conference, RadarConf 2016* (2016). DOI: 10.1109/RADAR.2016.7485215.
- [2.53] Winfried Mayer et al. “A compact 24 GHz sensor for beam-forming and imaging”. In: *9th International Conference on Control, Automation, Robotics and Vision, 2006, ICARCV '06* 1 (2006), pp. 1–6. DOI: 10.1109/ICARCV.2006.345160.
- [2.54] Steffen Lutz, Thomas Walter, and Robert Weigel. “Lens-based 77 GHz MIMO radar for angular estimation in multitarget environments”. In: *International Journal of Microwave and Wireless Technologies* 6.3-4 (2014), pp. 397–404. ISSN: 17590795. DOI: 10.1017/S1759078714000506.
- [2.55] Zhang Hui, Li Lin, and Wu Ke. “24GHz software-defined radar system for automotive applications”. In: *European Microwave Week 2007 Conference Proceedings, EuMW 2007 - 10th European Conference on Wireless Technology, ECWT 2007* October (2007), pp. 138–141. DOI: 10.1109/ECWT.2007.4403965.
- [2.56] Reinhard Feger et al. “A 77-GHz FMCW MIMO radar based on an SiGe single-chip transceiver”. In: *IEEE Trans. Microw. Theory Techn.* 57.5 (2009), pp. 1020–1035.
- [2.57] Liang Han and Ke Wu. “24-GHz integrated radio and radar system capable of time-agile wireless communication and sensing”. In: *IEEE Transactions*

- on Microwave Theory and Techniques* 60.3 PART 1 (2012), pp. 619–631. ISSN: 00189480. DOI: 10.1109/TMTT.2011.2179552.
- [2.58] Reinhard Feger, Clemens Pfeffer, and Andreas Stelzer. “A frequency-division MIMO FMCW radar system based on Delta–Sigma modulated transmitters”. In: *IEEE Trans. Microw. Theory Techn.* 62.12 (2014), pp. 3572–3581.
  - [2.59] Reinhard Feger, Andreas Haderer, and Andreas Stelzer. “Experimental verification of a 77-GHz synthetic aperture radar system for automotive applications”. In: *Microwaves for Intelligent Mobility (ICMIM), 2017 IEEE MTT-S International Conference on.* IEEE. 2017, pp. 111–114.
  - [2.60] Beatriz Mencia-Oliva et al. “Low-cost CW-LFM radar sensor at 100 GHz”. In: *IEEE transactions on microwave theory and techniques* 61.2 (2013), pp. 986–998.
  - [2.61] Frank Bauer et al. “A 79-GHz radar sensor in LTCC technology using grid array antennas”. In: *IEEE Transactions on Microwave Theory and Techniques* 61.6 (2013), pp. 2514–2521.
  - [2.62] Sang Young Kim et al. “A 76–84 GHz 16-element phased array receiver with a chip-level built-in-self-test system”. In: *Radio Frequency Integrated Circuits Symposium (RFIC), 2012 IEEE.* IEEE. 2012, pp. 127–130.
  - [2.63] Preeti Kumari, Amine Mezghani, and Robert W Heath. “JCR70: A low-complexity millimeter-wave proof-of-concept platform for a fully-digital SIMO joint communication-radar”. In: *IEEE Open Journal of Vehicular Technology* 2 (2021), pp. 218–234.
  - [2.64] Theodore S Rappaport et al. “Wireless communications: principles and practice”. In: vol. 2. Prentice Hall PTR New Jersey, 1996, p. 86.
  - [2.65] Egidio Ragonese et al. “CMOS Automotive Radar Sensors: mm-wave Circuit Design Challenges”. In: *IEEE Transactions on Circuits and Systems II: Express Briefs* (2022).
  - [2.66] ETSI Technical Committee Electromagnetic compatibility and Radio spectrum Matters (ERM). *Electromagnetic compatibility and Radio spectrum Matters (ERM); SRD radar equipment using Wideband Low Activity Mode*

- (WLAM) and operating in the frequency range from 24,05 GHz to 24,50 GHz; TR 102 892 V1.1.2 (2011-07). Tech. rep. European Telecommunications Standards Institute (ETSI), 2011.
- [2.67] Pascual D. Hilario Re. *Antenna Array Design for Retrodirective Wireless Power Transmission and Radar*. PhD Thesis, Heriot-Watt University, 2019, 2019.
- [2.68] Feng Xu and Ke Wu. “Guided-wave and leakage characteristics of substrate integrated waveguide”. In: *IEEE Transactions on microwave theory and techniques* 53.1 (2005), pp. 66–73.

## References: Chapter 3

- [3.1] Juergen Maisel. “A radar based satellite architecture for autonomous driving applications”. In: *Automotive radar sensors for semi-automatic and autonomous driving and parking systems*. AUTOLIV, 2017, p. 19.
- [3.2] Yuandan Dong and Tatsuo Itoh. “Planar ultra-wideband antennas in Ku- and K-band for pattern or polarization diversity applications”. In: *IEEE Transactions on Antennas and Propagation* 60.6 (2012), pp. 2886–2895.
- [3.3] Lisa S Locke, Jens Bornemann, and Stéphane Claude. “Substrate integrated waveguide-fed tapered slot antenna with smooth performance characteristics over an ultra-wide bandwidth”. In: *ACES*. Vol. 28. 2013.
- [3.4] Simon Kueppers, Harun Cetinkaya, and Nils Pohl. “A compact 120 GHz SiGe: C based  $2 \times 8$  FMCW MIMO radar sensor for robot navigation in low visibility environments”. In: *2017 European Radar Conference (EURAD)*. IEEE. 2017, pp. 122–125.
- [3.5] Herman Jalli Ng, Wael Ahmad, and Dietmar Kissinger. “Scalable MIMO radar utilizing delta-sigma modulation-based frequency-division multiplexing technique”. In: *2017 European Radar Conference (EURAD)*. IEEE. 2017, pp. 118–121.
- [3.6] Joachim Massen et al. “A 79 GHz SiGe short-range radar sensor for automotive applications”. In: *Int. J. Microw. Wirel. Technol.* 5.1 (2013), pp. 5–14.
- [3.7] Liam Daniel *et al.* “Application of Doppler beam sharpening for azimuth refinement in prospective low-THz automotive radars”. In: *IET Radar, Sonar Navig.* 12.10 (2018), pp. 1121–1130.

- [3.8] Shahzad Gishkori et al. “Imaging for a Forward Scanning Automotive Synthetic Aperture Radar”. In: *IEEE Trans. Aerosp. Electron. Syst.* (2018).
- [3.9] D Jasteh et al. “Experimental Low-Terahertz Radar Image Analysis for Automotive Terrain Sensing”. In: *IEEE Geosci. Remote. Sens. Lett.* 13.4 (2016), pp. 490–494.
- [3.10] You-Sun Won, Chung-Hwan Kim, and Sang-Gug Lee. “Range resolution improvement of a 24 GHz ISM band pulse radar—A feasibility study”. In: *IEEE Sensors Journal* 15.12 (2015), pp. 7142–7149.
- [3.11] Winfried Mayer et al. “A compact 24 GHz sensor for beam-forming and imaging”. In: *2006 9th International Conference on Control, Automation, Robotics and Vision*. IEEE. 2006, pp. 1–6.
- [3.12] Cheng-Yu Ho et al. “A Low-Cost Antenna-in-Package Solution for 77GHz Automotive Radar Applications”. In: *2019 International Conference on Electronics Packaging (ICEP)*. IEEE. 2019, pp. 110–114.
- [3.13] Dominik Kellner et al. “Instantaneous ego-motion estimation using doppler radar”. In: *16th International IEEE Conference on Intelligent Transportation Systems (ITSC 2013)*. IEEE. 2013, pp. 869–874.
- [3.14] Mike Cherniakov et al. “Bistatic, Multistatic Radar and MIMO Radar - WF10 Workshop”. In: *2016 13th European Radar Conference (EuRAD)*. IEEE. 2016.
- [3.15] Pier Francesco Sammartino, Christopher J Baker, and Hugh D Griffiths. “Frequency diverse MIMO techniques for radar”. In: *IEEE Transactions on Aerospace and Electronic Systems* 49.1 (2013), pp. 201–222.
- [3.16] Florian Folster, Hermann Rohling, and Urs Lubbert. “An automotive radar network based on 77 GHz FMCW sensors”. In: *IEEE International Radar Conference, 2005*. IEEE. 2005, pp. 871–876.
- [3.17] Michael Klotz and Hermann Rohling. “A 24 GHz short range radar network for automotive applications”. In: *2001 CIE International Conference on Radar Proceedings (Cat No. 01TH8559)*. IEEE. 2001, pp. 115–119.

- [3.18] Maximilian Steiner, Karim S Osman, and Christian Waldschmidt. “Cooperative target detection in a network of single-channel radar sensors”. In: *2019 12th German Microwave Conference (GeMiC)*. IEEE. 2019, pp. 91–94.
- [3.19] Qian He, Rick S Blum, and Zishu He. “Noncoherent versus coherent MIMO radar for joint target position and velocity estimation”. In: *Proceedings of 2011 IEEE CIE International Conference on Radar*. Vol. 1. IEEE. 2011, pp. 108–111.
- [3.20] Hai Deng. “Orthogonal netted radar systems”. In: *IEEE aerospace and electronic systems magazine* 27.5 (2012), pp. 28–35.
- [3.21] Jau-Jr Lin. “Integration of multiple automotive radar modules based on fiber-wireless network”. In: *2015 24th Wireless and Optical Communication Conference (WOCC)*. IEEE. 2015, pp. 36–39.
- [3.22] R Feger et al. “A 77-GHz FMCW MIMO radar based on loosely coupled stations”. In: *2012 The 7th German Microwave Conference*. IEEE. 2012, pp. 1–4.
- [3.23] Andreas Frischen, Jürgen Hasch, and Christian Waldschmidt. “A cooperative MIMO radar network using highly integrated FMCW radar sensors”. In: *IEEE Transactions on Microwave Theory and Techniques* 65.4 (2017), pp. 1355–1366.
- [3.24] Andreas Frischen, Gor Hakobyan, and Christian Waldschmidt. “Coherent measurements with MIMO radar networks of incoherent FMCW sensor nodes”. In: *IEEE Microwave and Wireless Components Letters* 30.7 (2020), pp. 721–724.
- [3.25] Benedikt Meinecke et al. “Coherent multistatic MIMO radar networks based on repeater tags”. In: *IEEE Transactions on Microwave Theory and Techniques* 67.9 (2019), pp. 3908–3916.
- [3.26] Eric Klinefelter and Jeffrey A Nanzer. “Interferometric microwave radar with a feedforward neural network for vehicle speed-over-ground estimation”. In: *IEEE Microwave and Wireless Components Letters* 30.3 (2020), pp. 304–307.

- [3.27] D. Mateos-Núñez et al. “Sparse array design for Automotive MIMO Radar”. In: *2019 16th European Radar Conference (EuRAD)*. 2019, pp. 249–252.
- [3.28] C. M. Schmid et al. “Design of a linear non-uniform antenna array for a 77-GHz MIMO FMCW radar”. In: *2009 IEEE MTT-S International Microwave Workshop on Wireless Sensing, Local Positioning, and RFID*. 2009, pp. 1–4. DOI: 10.1109/IMWS2.2009.5307896.
- [3.29] Robin Rajamäki and Visa Koivunen. “Comparison of sparse sensor array configurations with constrained aperture for passive sensing”. In: *2017 IEEE Radar Conference (RadarConf)*. IEEE. 2017, pp. 0797–0802.
- [3.30] YI Chong and DOU Wenbin. “Microstrip series fed antenna array for millimeter wave automotive radar applications”. In: *IEEE MTT-S IMWS*. IEEE. 2012, pp. 1–3.
- [3.31] Ke Wu, Maurizio Bozzi, and Nelson JG Fonseca. “Substrate Integrated Transmission Lines: Review and Applications”. In: *IEEE Journal of Microwaves* 1.1 (2021), pp. 345–363.
- [3.32] Wolfgang Menzel. “Antennas in automobile radar”. In: *Handbook of Antenna Technologies*. Springer, 2014, pp. 1–22.
- [3.33] Nelson Jorge G Fonseca, Ahmed Ali, and Hervé Aubert. “Cancellation of beam squint with frequency in serial beamforming network-fed linear array antennas”. In: *IEEE Antennas Propag Mag* 54.1 (2012), pp. 32–39.
- [3.34] Ramesh Garg, Inder Bahl, and Maurizio Bozzi. *Microstrip lines and slotlines*. Artech house, 2013.
- [3.35] SD Targonski and DM Pozar. “Minimization of beam squint in microstrip reflectarrays using an offset feed”. In: *IEEE Antennas and Propagation Society International Symposium. 1996 Digest*. Vol. 2. IEEE. 1996, pp. 1326–1329.
- [3.36] Maurizio Bozzi, Anthimos Georgiadis, and Kaijie Wu. “Review of substrate-integrated waveguide circuits and antennas”. In: *IET Microw. Antennas Propag.* 5.8 (2010), pp. 909–920.



- [3.37] Feng Xu and Ke Wu. “Guided-wave and leakage characteristics of substrate integrated waveguide”. In: *IEEE Transactions on Microwave Theory and Techniques* 53.1 (2005), pp. 66–73. DOI: 10.1109/tmtt.2004.839303.
- [3.38] Thomas A Milligan. *Modern antenna design*. John Wiley & Sons, 2005.
- [3.39] Pascual D Hilario Re et al. “FMCW Radar With Enhanced Resolution and Processing Time by Beam Switching”. In: *IEEE Open Journal of Antennas and Propagation* 2 (2021), pp. 882–896.
- [3.40] Wei Deng, Reza Mahmoudi, and Arthur HM Van Roermund. *Time multiplexed beam-forming with space-frequency transformation*. Springer, 2012.
- [3.41] A. M. Haimovich, R. S. Blum, and L. J. Cimini. “MIMO Radar with Widely Separated Antennas”. In: *IEEE Signal Processing Magazine* 25.1 (2008), pp. 116–129.
- [3.42] Gorka Rubio-Cidre et al. “DDS-based signal-generation architecture comparison for an imaging radar at 300 GHz”. In: *IEEE Transactions on Instrumentation and Measurement* 64.11 (2015), pp. 3085–3098.
- [3.43] Bar-Giora Goldberg. *Digital frequency synthesis demystified*. Elsevier, 2000.
- [3.44] *Direct Modulation/Fast Waveform Generating, 13 GHz, Fractional-N Frequency Synthesizer*. ADF4159. Rev. E. Analog Devices. 2017.
- [3.45] Constantine A Balanis. *Antenna theory: analysis and design*. John wiley & sons, 2016.
- [3.46] Jyrki K Kauppinen et al. “Smoothing of spectral data in the Fourier domain”. In: *Applied optics* 21.10 (1982), pp. 1866–1872.
- [3.47] Emna Bel Kamel, Alain Peden, and Patrice Pajusco. “RCS modeling and measurements for automotive radar applications in the W band”. In: *2017 11th European Conference on Antennas and Propagation (EUCAP)*. IEEE. 2017, pp. 2445–2449.

## References: Chapter 4

- [4.1] Frederick N Fritsch and Ralph E Carlson. “Monotone piecewise cubic interpolation”. In: *SIAM Journal on Num. Analysis* 17.2 (1980), pp. 238–246.
- [4.2] Charles L Lawson. “Software for C1 surface interpolation”. In: *Mathematical software*. Elsevier, 1977, pp. 161–194.

## References: Chapter 5

- [5.1] C. Waldschmidt, J. Hasch, and W. Menzel. “Automotive Radar — From First Efforts to Future Systems”. In: *IEEE Journal of Microwaves* 1.1 (2021), pp. 135–148. DOI: 10.1109/JMW.2020.3033616.
- [5.2] Marco Rossi, Alexander M Haimovich, and Yonina C Eldar. “Spatial compressive sensing for MIMO radar”. In: *IEEE Transactions on Signal Processing* 62.2 (2013), pp. 419–430.
- [5.3] Michael Francis Minner. *Compressive Sensing Applied to MIMO Radar and Sparse Disjoint Scenes*. Drexel University, 2016.
- [5.4] Francesco Belfiori et al. “Digital beam forming and compressive sensing based DOA estimation in MIMO arrays”. In: *2011 8th European Radar Conference*. IEEE. 2011, pp. 285–288.
- [5.5] Aitor Correas-Serrano and Maria A Gonzalez-Huici. “Experimental evaluation of compressive sensing for DoA estimation in automotive radar”. In: *2018 19th International Radar Symposium (IRS)*. IEEE. 2018, pp. 1–10.
- [5.6] Dominic Phippen et al. “Compressive Sensing for Automotive 300GHz 3D Imaging Radar”. In: *2020 IEEE Radar Conference (RadarConf20)*. IEEE. 2020, pp. 1–6.
- [5.7] André Dürr et al. “Radar Imaging Using Electrically Large Arrays With High Range Resolution at 160 GHz”. In: *2020 17th European Radar Conference (EuRAD)*. 2021, pp. 326–329. DOI: 10.1109/EuRAD48048.2021.00090.
- [5.8] Cristian A Alistarh et al. “Compressed Sensing Radar Using a Non-Uniformly Spaced SIW Receiver Array”. In: *IEEE Transactions on Antennas and Propagation* (2022).

- [5.9] Yin Zhang. “Theory of compressive sensing via  $l_1$ -minimization: A non-rip analysis and extensions”. In: *Journal of the Operations Research Society of China* 1.1 (2013), pp. 79–105.
- [5.10] Richard Baraniuk et al. “An introduction to compressive sensing”. In: *Connections e-textbook* (2011), pp. 24–76.
- [5.11] Laura Anitori and Joachim Ender. “Waveform Design for Sparse Signal Processing in Radar”. In: *2021 IEEE Radar Conference (RadarConf21)*. IEEE. 2021, pp. 1–6.
- [5.12] Fabian Roos et al. “Compressed Sensing based Single Snapshot DoA Estimation for Sparse MIMO Radar Arrays”. In: *2019 12th German Microwave Conference (GeMiC)*. 2019, pp. 75–78. DOI: 10.23919/GEMIC.2019.8698136.
- [5.13] Allen Y Yang et al. “Fast  $l_1$ -minimization algorithms and an application in robust face recognition: A review”. In: *2010 IEEE international conference on image processing*. IEEE. 2010, pp. 1849–1852.
- [5.14] Yan Zhang et al. “Phase Transition Analysis for Compressive Sensing Based DoA Estimation in Automotive Radar”. In: *2020 21st International Radar Symposium (IRS)*. IEEE. 2020, pp. 396–401.
- [5.15] Dirk A Lorenz, Marc E Pfetsch, and Andreas M Tillmann. “Solving basis pursuit: Heuristic optimality check and solver comparison”. In: *ACM Transactions on Mathematical Software (TOMS)* 41.2 (2015), pp. 1–29.
- [5.16] Ashkan Esmaeili and Farokh Marvasti. “Comparison of several sparse recovery methods for low rank matrices with random samples”. In: *2016 8th International Symposium on Telecommunications (IST)*. IEEE. 2016, pp. 191–195.
- [5.17] Cristian Alistarh et al. “Millimetre-Wave FMCW MIMO Radar System Development Using Broadband SIW Antennas”. In: *12th European Conference on Antennas and Propagation (EuCAP)*. Jan. 1, 2018. published.